Reconfigurable photonic integrated circuits for space applications

Politecnico di Bari

Department of Mechanics, Mathematics and Management
ENGINEERING AND AEROSPACE SCIENCES
Ph.D. Program
SSD: IINF-01/A – ELECTRONICS

Final Dissertation

Reconfigurable Photonic Integrated Circuits for Space applications

---

by

ANNARITA di TOMA

Supervisors:

Prof. Caterina CIMINELLI, PhD

Dr. Giuseppe BRUNETTI, PhD

Coordinator of Ph.D. Program:
Prof. Caterina CIMINELLI, PhD

Course n°38, 01/11/2022 – 31/10/2025

Department of Mechanics, Mathematics and Management
ENGINEERING AND AEROSPACE SCIENCES
Ph.D. Program
SSD: IINF-01/A – ELECTRONICS

Final Dissertation

Reconfigurable Photonic Integrated Circuits for Space applications

by

ANNARITA di TOMA

Referees:

Dr. Padraic Morrissey, PhD

Prof. Marian Marciniak, PhD

Supervisors:

Prof. Caterina CIMINELLI, PhD

Dr. Giuseppe BRUNETTI, PhD

Coordinator of Ph.D. Program:

Prof. Caterina CIMINELLI, PhD

Course n°38, 01/11/2022 – 31/10/2025

“E quindi uscimmo a riveder le stelle”

Inferno XXXIV, 139

Abstract

Integrated photonics is rapidly emerging as a transformative technology for space engineering, expected to disrupt satellite systems in much the same way fiber optics reshaped terrestrial networks. Photonic integrated circuits (PICs), conceived as scalable systems-on-chip, provide decisive advantages in terms of size, weight, power efficiency, bandwidth, and reconfigurability, all of which are critical within the NewSpace paradigm of reduced cost, rapid development cycles, and proliferating small-satellite constellations. With a market projected to grow from hundreds of millions to several billions of dollars within a decade, PICs combine compactness with embedded computing capabilities and high functional integration, positioning them as indispensable building blocks for future payloads.

This thesis investigates the use of integrated photonic devices and photonic integrated circuits to enable advanced functionalities in satellite payloads, with particular focus on reconfigurable filtering, beamforming, and on-board data processing for Synthetic Aperture Radar (SAR) systems. The work first analyzes the requirements and architectures of reconfigurable photonic filters, introducing novel schemes based on cascaded ring resonators and coupled-resonator optical waveguides (CROWs) to achieve wide tunability and low insertion loss. Subsequently, photonic beamforming networks for next-generation phased array antennas are addressed, with emphasis on architectures exploiting delay lines, asymmetric power splitters, or metasurfaces for wideband beam steering and optical intersatellite links. Finally, a fully reconfigurable integrated photonic FFT processor for on-board SAR data processing is proposed. This architecture overcomes the main limitations of conventional electronic processors and previously reported optical approaches, enabling real-time data compression directly in orbit.

The integration of these building blocks culminates in the design of a complete photonic SAR payload system, comprising a linearly chirped waveform generator, a beamforming network, and an FFT processor.

The proposed solutions are benchmarked against state-of-the-art technologies and validated against the requirements of representative Earth observation missions, such as COSMO-SkyMed and Sentinel-1, or Agencies and Space companies constraints. Results demonstrate that photonic integration not only ensures compliance with stringent spaceborne specifications but also enables miniaturization, reduced power consumption, and enhanced functionality, thereby addressing the emerging needs of distributed SAR constellations and small-satellite platforms.

The contributions of this thesis provide a comprehensive analysis of the role of photonic technologies in future satellite payloads, paving the way toward fully photonic SAR instruments. These advances highlight the potential of photonics to transform next-generation space missions, where reconfigurability, scalability, and real-time processing will be essential to meet the challenges of Earth observation, global monitoring, and secure space communications.

Acknowledgments

I would like to express my sincere gratitude to Professor Caterina Ciminelli for her guidance and continuous support throughout my doctoral path. Her ability to recognize and feed potential, together with her constant commitment to providing opportunities for professional growth, have been essential to the development of my academic and research skills. I am deeply grateful for her trust, mentorship, and for the example of professionalism she has consistently demonstrated, both from a technical and managerial perspective.

I would also like to extend my thanks to Dr. Giuseppe Brunetti for the insightful discussions, constructive feedback, and constant encouragement that have greatly contributed to my progress. His support has been instrumental in helping me make the most of every opportunity that arose during this journey.

I am sincerely thankful to both for their guidance and collaboration, without which the outcomes of this work would not have been possible.

Finally, I wish to thank my colleagues at the Optoelectronics Laboratory for their collaboration and friendship. Sharing both challenging and pleasant moments with them has made my time in the laboratory an enriching and enjoyable experience.

Contents

List of figures

List of tables

Chapter 1

Introduction

1.1 The Role of Photonics in the New Space Era

Integrated photonics has the capability of revolutionizing the New Space industry, enabling significant advancements in systems performance, miniaturization, and functionality. Photonic technologies can reduce the size, weight, and power consumption of on-board instruments while boosting capabilities in navigation, imaging, sensing, and high-speed optical communication perfectly matching with the NewSpace Economy goals. Photonics integrated circuits, particularly Silicon on Insulator (SOI) and Lithium Niobate on Insulator (LNOI), provide versatile platforms for these applications leading to this transformation by allowing multiple optical components to be integrated onto a single chip. Optical telecommunications, LiDAR, 3D integration, quantum computing, optical gyroscopes, and even medical photonics hold significant potential, though facing technical and regulatory challenges [1, 2].

According to the ESA *Report on the Space Economy 2025*, in 2024 the global Space Economy registered public and private investment increases of 9% and 20%, respectively, together with the rising of Space Upstream and Downsteam Market values of 22% and 9%, corresponding to €63 and €408 billion. Private investment in space demonstrated stabilization in terms of volume of investment in 2024, reaching €7 billion. This represents a 20% increase from 2023. The public and private investment trends over the last five years are represented in Figure 1.1.1. Worldwide space companies received investments through 266 deals in 2024, a modest 2% increase from 2023. In Europe, private space investment reached a new record high in 2024, with European space ventures rising more than €1.5 billion (growing 56% from 2023) through 99 deals (compared with 82 deals in 2023) [3].

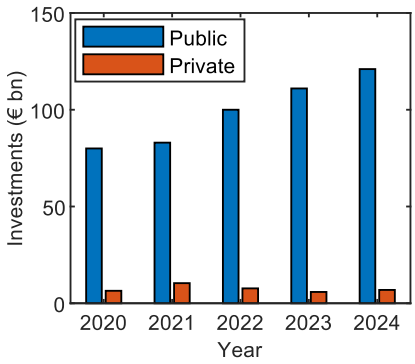

Figure 1.1.1 Public and Private Investments trends in the space sector over the last five years

As a result, space companies are increasingly investing in photonics to enhance system performance and reduce operational costs. For instance, SpaceX utilizes PICs in its satellite constellations to enable high-speed, long-distance data communication [4]. Airbus has launched the *Space Photonics Unified Roadmap* (SPUR), a strategic initiative to identify and address common photonic requirements across future space systems and reinforcing the links with industries and space agencies [5]. Other commercial players, such as the German company Rivada Space Networks, that plans to deploy a constellation of 600 LEO satellites using optical intersatellite links to ensure secure private connections [6], or the French company Exail, that in partnership with Airbus Defense & Space (ADS) has developed the Astrix fiber-optic gyroscope technology [7], are exploring photonics for next-generation satellite communications and advanced sensing networks. These efforts reflect a broader industry trend of leveraging photonics to improve scalability, data handling, and signal fidelity in complex space missions.

As for Public Institution and Agencies, the European Union's Horizon 2020 (H2020) and CORDIS programs have supported a range of space photonics-related research projects, including Photonics21 [8], INPHOMIR [9], SIPhoDiAS [10], and SPACEBEAM [11], which aim to develop next-generation space-grade photonic platforms and systems. In the United States, NASA continues to drive innovation in integrated photonics, allocating substantial funding toward research and technology development. The Photonics Group at the Goddard Space Flight Center (GSFC) have produced and tested fibers for several space missions as including Lunar Reconnaissance Orbiter (LRO), Curiosity & Perseverance, Ice, Cloud, and land Elevation Satellite 2 (ICESAT-2), and Plankton, Aerosol, Cloud, ocean Ecosystem (PACE), and is working on the Real Time Optical Receiver Project to develop an high photon efficiency transmitter and receiver [12, 13].

Nowadays, indeed, several specialized photonics technologies are seeing adoption. Optoelectronic components are now integral to telecommunications satellites, while optopyrotechnics, which employ laser ignition, are improving the safety and efficiency of launch systems. Photonics-based LIDAR systems, such as those deployed in the ADM Aeolus and EarthCare missions, play a vital role in atmospheric monitoring and scientific data collection. Meanwhile, microwave photonics is enhancing RF payloads through optical signal

manipulation, enabling higher performance and flexibility in space communications.
Across all these domains, critical components such as lasers, optical transceivers, and PICs are reshaping how space systems are designed, operated, and scaled to accommodate the need of higher frequency, wider bandwidth, and lower latency for telemetry, tracking, command (TT&C), data return, and Earth Observation.

1.2 Research motivations

The spread of CubeSats, small modular satellites typically measuring 10×10×10 cm^3 per unit, has revolutionized space access by significantly reducing both satellite production costs and launch expenses. This miniaturization has opened the doors of space not only to governmental agencies and supranational organizations but also to private entities and academic institutions. CubeSats offer a cost-effective, rapid, and versatile platform for innovation and exploration. Public and private actors now leverage these satellites for a wide range of missions, including technology demonstrations, scientific research, and educational initiatives. For example, the GomX-3 mission demonstrated software-defined radio technology for aircraft detection [14], while the OPS-SAT CubeSat functions as a flying laboratory to test innovative software and protocols [15]. These missions often employ commercial off-the-shelf components, enabling much shorter development cycles, typically within one to two years, compared to traditional satellite programs. CubeSats also enable a multitude of scientific efforts that were previously hindered by cost and size constraints. CubeSat missions have tracked solar irradiance, monitored space radiation, and investigated the plasma environment in orbit. By facilitating distributed measurements and simultaneous multi-point observations of space environments, CubeSats greatly enhance the scope and resolution of scientific investigations.
As a result of these advancements, space architecture has evolved from relying on monolithic satellites in Geostationary Earth Orbit (GEO) to deploying constellations of CubeSats with distributed functionalities in Low Earth Orbit (LEO). This shift not only reduces data transmission latency, which is crucial for telecommunications systems, but also improves image resolution for Earth observation satellites.
However, downsizing satellite systems comes with performance parameters decreasing, such as image resolution, ground coverage, orbit duty cycle, revisiting time, and mission lifetime, linked to electronic miniaturization limits. Miniaturization needing leads to the development of competitive technologies with intrinsic compactness such as photonics. The main advantages of photonics over competing technologies, such as electromagnetic interference immunity, low power consumption, high immunity to vibration/shock, radiation and small footprint, are critical for on-board systems, pushing research effort on photonic sub-systems for on-board satellites [16].

Photonic Integrated Circuits (PICs) have proved to lead to > 50% mass and power reduction, 100x footprint decrement, higher bandwidth and data rate, no-cost redundancy, aperture-independency, transparency to modulation format, versatility, and scalability [17]. The application of PICs to Telecommunications payloads has already proved Signal to Noise Ratio (SNR) enhancement, GHz-precision RF signal processing capability, propagation losses and power consumption reduction, enabling faster and higher bandwidth data transfer (with pipes higher than 100Gb/s over distances longer than 10km exploiting dense wavelength division multiplexing (DWDM)) [18]. Several missions have been developed to test and measure the optical downlink and uplink performance proving downlink speeds of up to 200 Gbps (see Figure 1.2.1) and an uplink data rate of 200 Kbps, and future mission launches include demonstrations of optical crosslinks on CubeSats, such as the CLICK mission [19, 20].

Despite the impressive results achieved, a problem is not solved yet. Currently, photonic systems are implemented as Application-Specific Photonic Integrated Circuits (ASPICs) still, designed to fulfill the target mission constraints, increasing the time to market and inflating system development costs. In the development of electronic products, the traditional design–fabrication–test–optimization cycle has been significantly shortened while broadening system functionalities using programmable platforms, such as microcontrollers, digital signal processors (DSPs), or field-programmable gate arrays (FPGAs), which can be reconfigured to implement a wide range of functions. These platforms are typically supported by development kits that facilitate rapid prototyping, enabling new functionalities to be programmed and tested within weeks rather than months. A similar paradigm can be applied to reconfigurable photonic integrated circuits, whose inherent reconfigurability offers increased functional flexibility and can substantially reduce product development time compared to ASPIC-based solutions. Figure 1.2.2 illustrates the development timeline of electronic systems and the corresponding natural progression of photonic integration technologies.

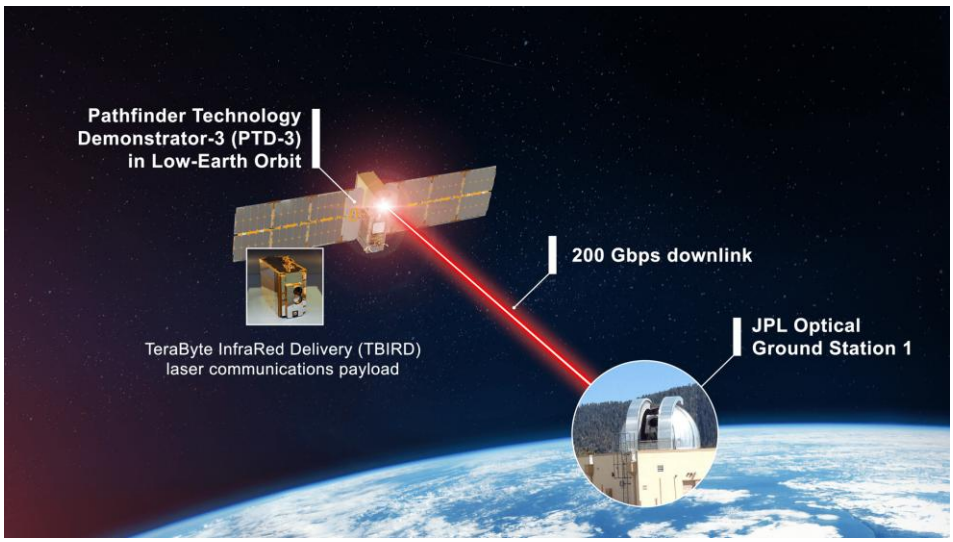

Figure 1.2.1 NASA's TBIRD on-orbit demonstration of laser Communication using infrared light [20]

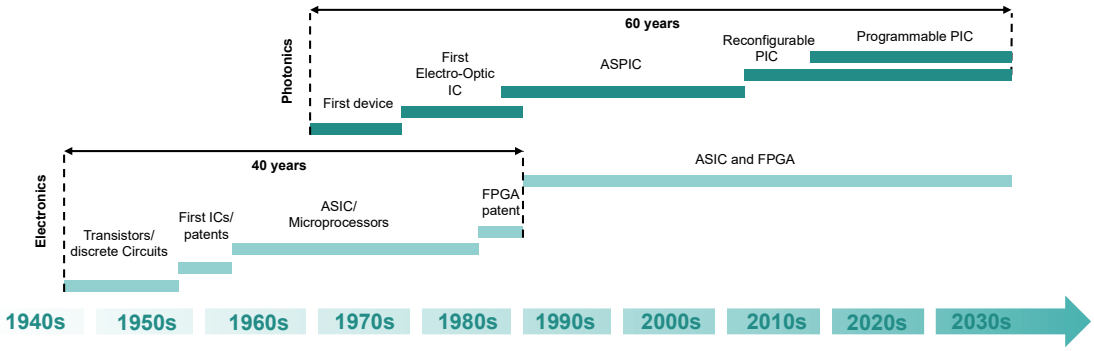

Figure 1.2.2 Electronics and Photonics timeline. (IC: integrated Circuit, ASIC: Application Specific Integrated Circuit, FPGA: Field Programmable Gate Array, ASPIC: Application Specific Photonic Integrated Circuit)

This approach is particularly advantageous for applications involving optical signal processing within standard telecom and datacom wavelength bands (1250–1600 nm). Beyond flexible fiber-optic communication systems (e.g., fiber-to-the-X), potential use cases include sensor readout architectures (e.g., attitude control systems) and optical beamforming for free-space optical communication or LiDAR systems. A key domain where reconfigurable photonic circuits are poised to have significant impact is microwave photonics, where high-frequency radio signals are processed in the optical domain. This capability supports a wide array of applications, ranging from advanced synthetic radar systems (SARs) to satellite and 5G wireless communications. Indeed, space communications keep on moving from S-band to X-band, and from X-band to Ka-band, accommodating the growing demand for high-volume data transmission in scientific missions. Forecasts suggest that space applications will soon exceed the capacity limits of the RF Ka-band (GHz), prompting a shift toward the higher-capacity, unregulated optical communication spectrum (THz).

This evolution necessitates satellite payloads that are inherently reconfigurable, capable of adapting and optimizing their performance even after launch. Such adaptability is crucial to meet changing user needs related to bandwidth, coverage, latency and frequency allocation, also enlarging the satellite operative lifetime. The dynamism of modern space missions necessitates a transformative approach, enabling satellites to reconfigure and fine-tune their functionalities on orbit. Satellite constellations for global internet provision, Earth Observation, and remote sensing, require payloads with the agility to dynamically adjust bandwidth, optimize coverage zones, and reallocate frequency resources in real time. Therefore, the development of adaptable and responsive satellite payloads becomes imperative to meet the ever-changing demands of a rapidly evolving space landscape.

1.3 Research objectives

The primary objective of this PhD thesis is to investigate and demonstrate how the adoption of reconfigurable photonic circuits can provide substantial advantages for the design and operation of next-generation satellite systems. The increasing demand for compact, lightweight, and energy-efficient satellite

platforms, particularly in the context of CubeSats and other small satellites operating in Low Earth Orbit, has intensified the search for alternative technologies capable of delivering high performance within stringent physical constraints. In this framework, integrated photonics emerges as a promising candidate, with reconfigurable photonic circuits offering a unique combination of miniaturization, functional flexibility, and performance enhancement.

Unlike traditional electronic systems, reconfigurable photonic integrated circuits allow for the significant reduction of system size and weight, which is critical for CubeSat compatibility. At the same time, these circuits enable adaptive functionality, allowing the same hardware to perform different roles or operate across different frequency bands through software-defined reconfiguration. This flexibility is particularly valuable in space applications, where physical access to the hardware is impossible once deployed. Through remote control signals from ground stations, it becomes possible to reprogram the photonic circuitry in orbit, adapting the satellite to changing mission requirements or to shifts in operational frequency bands, thus extending the functional lifetime of the satellite without the need for hardware replacement.

Moreover, reconfigurable photonic systems introduce several performance advantages. In the field of telecommunications, they offer lower latency compared to electronic counterparts due to the intrinsic speed of light-based signal propagation and processing. In remote sensing applications, such as Synthetic Aperture Radar (SAR), photonic implementations can achieve higher spatial and spectral resolution, thanks to their wider bandwidth and ability to process high-frequency signals with minimal distortion directly on-board.

In addition to reconfigurability, photonic circuits retain the inherent benefits of conventional photonic technologies. These include near real-time signal processing, immunity to electromagnetic interference (EMI)—a critical factor in the congested and noise-prone electromagnetic environment of space—transparency to modulation formats, and improved sensitivity in sensor readout systems, which enhances detection accuracy and efficiency in optical sensing payloads.

Taken together, these attributes position reconfigurable photonics as a disruptive enabler for a new class of agile, high-performance, and resource-efficient satellite systems. This doctoral research is positioned within this technological evolution, aiming to investigate and develop reconfigurable photonic devices and systems tailored to the needs of next-generation payloads and sensing platforms.

The central objective of this thesis is to explore and demonstrate novel photonic architectures that can be dynamically reconfigured in real time, offering adaptability and performance levels beyond the reach of traditional technologies. A significant part of the research has been dedicated to the design of microwave photonic filters with tunable bandwidth and central frequency, which are fundamental components for agile and intelligent communication payloads. These filters allow for real-time spectral reallocation, ensuring more efficient use of the radio frequency spectrum in increasingly crowded and dynamic environments.

Beyond spectral filtering, another core focus of the work has been the development of advanced photonic beamforming systems. These systems are designed to generate steerable beams with controllable beamwidths, enabling a high degree of directional flexibility. Such functionality is crucial in a variety of modern and emerging scenarios, including Earth observation, 5G communications, and inter-satellite links, where the ability to reconfigure the spatial properties of the signal in real time can drastically improve performance, reduce interference, and enhance overall system agility. The use of photonics in this domain offers a compelling path toward miniaturized and power-efficient beamforming solutions with ultra-fast response times.
Furthermore, the thesis addresses one of the major challenges in the field of spaceborne synthetic aperture radar (SAR), the enormous volume of data that must be transmitted from orbit to ground stations. To mitigate this bottleneck, a reconfigurable photonic processor has been proposed and investigated, capable of performing on-board, real-time compression of SAR echoes. By processing the data directly in the optical domain and reducing the data burden before downlink, this approach enables more autonomous satellite operations and a significant reduction in required communication resources.
Overall, the thesis contributes to the advancement of reconfigurable photonic technologies as key enablers of the next generation of communication and remote sensing systems. By leveraging the unique advantages of photonic integration, such as broadband operation, low latency, and reduced form factor, the research opens the way to more intelligent, efficient, and responsive systems that are better suited to the demands of future aerospace and terrestrial applications.

1.4 Thesis outline

Chapter 2, titled *"Shaping Signals in Space with Reconfigurable Photonic Filters"*, establishes the groundwork for leveraging advanced photonic filtering techniques in satellite payloads. It begins by outlining the stringent spatial and functional requirements of telecom payloads in spaceborne systems, emphasizing the growing demand for compact, energy-efficient, and dynamically reconfigurable solutions. The chapter then reviews the state-of-the-art (SOA) in reconfigurable photonic filters, identifying key technologies and their limitations. It proceeds to explore cutting-edge strategies to expand filter reconfigurability through novel integrated photonic architectures. These include independently cascaded tunable ring resonators for flexible spectral shaping, cascaded coupled resonator optical waveguide (CROW) structures for increased filtering precision, and the use of phase-change materials (PCM) to enable non-volatile and thermally tunable responses.

Chapter 3, *"Photonic Beamforming for Next-Generation Satellites"*, transitions the discussion toward spatial signal control, beginning with the role of beamforming in both telecommunications (TLC) and Earth Observation (EO) missions. Traditional electronic and RF-based beamforming methods are reviewed before introducing

reconfigurable optical beam steering networks optimized for TLC satellites. The chapter further presents an optical beam steering solution capable of achieving sub-meter resolution for Synthetic Aperture Radar (SAR) applications and culminates with the development of reconfigurable beamforming metasurface designed to enhance optical intersatellite links.

Chapter 4, *"On-board Data Processing through Photonics"*, addresses the increasing demands of satellite data management. It outlines the transition from electronic to photonic processors, focusing on the advantages of integrated photonic architectures for redundancy and power efficiency. The core of this chapter is the design of an integrated photonic Fast Fourier Transform (FFT) processor tailored for SAR onboard data processing.

Chapter 5, *"A full photonic SAR system"*, provides a comprehensive assessment of the advantages of photonic solutions over conventional electronics for SAR payload building blocks, such as the chirped microwave generator, the beamforming network, and the on-board processor. It introduces innovative approaches to overcome emerging limitations, paving the way for next-generation photonic SAR systems.

Finally, Chapter 6 offers a comprehensive conclusion, summarizing key contributions and outlining promising research directions for advancing photonic technologies in space applications.

1.5 List of publications

Journal articles

[1] A. di Toma, G. Brunetti, M. S. Chiriacò, F. Ferrara, C. Ciminelli, "A Novel Hybrid Platform for Live/Dead Bacteria Accurate Sorting by On-Chip DEP Device," *International Journal of Molecular Sciences*, vol. 24, no. 8, p. 7077, 2023, doi: https://doi.org/10.3390/ijms24087077.

[2] A. di Toma, G. Brunetti, N. Saha, C. Ciminelli, "Fully reconfigurable photonic filter for flexible payloads," *Applied Sciences*, vol. 14, no. 2, p. 488, 2024, doi: https://doi.org/10.3390/app14020488.

[3] A. di Toma, G: Brunetti, P. Colapietro, C. Ciminelli, "High-resolved near-field sensing by means of dielectric grating with a box-like resonance shape," *IEEE Sensors Journal*, vol. 24, no. 5, pp. 6045-6053, 2024, doi: 10.1109/JSEN.2024.3349948.

[4] P. Colapietro, G. Brunetti, A. di Toma, F. Ferrara, M. S. Chiriacò, C. Ciminelli, "High Stability and Low Power Nanometric Bio-Objects Trapping through Dielectric–Plasmonic Hybrid Nanobowtie," *Biosensors*, vol. 14, no. 8, p. 390, 2024, doi: https://doi.org/10.3390/bios14080390.

[5] N. Saha, G. Brunetti, A. di Toma, M. N. Armenise, C. Ciminelli, "Silicon Photonic filters: A pathway from basics to applications," *Advanced Photonics Research*, vol. 5, no. 10, p. 2300343, 2024, doi: https://doi.org/10.1002/adpr.202300343.

[6] A. di Toma, G. Brunetti, M. N. Armenise, C. Ciminelli, "LiNbO_3-Based Photonic FFT Processor: An Enabling Technology for SAR On-Board Processing," *Journal of Lightwave Technology*, vol. 43, no. 2, pp. 912-921, 2025, doi: 10.1109/JLT.2024.3453670.

[7] G. Brunetti, A. di Toma, G. Campiti, C. Ciminelli, "Optical beam steering network design for sub-meter satellite SAR" *Optics and Lasers in Engineering*, vol. 198, pp. 109520, 2026, doi: https://doi.org/10.1016/j.optlaseng.2025.109520.

[8] A. di Toma, G. Brunetti, C. Ciminelli, "Reconfigurable Beamforming Metasurface for Optical Inter-satellite Links" submitted to *IOP Journal of Optics*.

Book chapters

[9] A. di Toma, G. Brunetti, N. Sasanelli, M. N. Armenise, C. Ciminelli, "Sorting of Live/dead Escherichia Coli by Means of Dielectrophoresis for Rapid Antimicrobial Susceptibility Testing", in *Berta, R., De Gloria, A. (eds) Applications in Electronics Pervading Industry, Environment and Society. ApplePies 2022.* Lecture Notes in Electrical Engineering, vol 1036. Springer, Cham., 2023, https://doi.org/10.1007/978-3-031-30333-3_25

[10] G. Brunetti, N. Sasanelli, N. Saha, G. Campiti, F. Hassan, A. di Toma, M. N. Armenise, C. Ciminelli, "Integrated photonics for NewSpace," in *Berta, R., De Gloria, A. (eds) Applications in Electronics Pervading Industry, Environment and Society. ApplePies 2022*. Lecture Notes in Electrical Engineering, vol 1036. Springer, Cham., 2023, https://doi.org/10.1007/978-3-031-30333-3_39

Conference proceedings

[11] M. N, Armenise, A. di Toma, G. Brunetti, N. Saha, C. Ciminelli, "Flexible photonic integrated circuits: a new paradigm to process data on-board satellites," in *2023 23rd International Conference on Transparent Optical Networks (ICTON)*, Bucharest, Romania, July 2-6, 2023, p. 1, doi: 10.1109/ICTON59386.2023.10207537.

[12] C. Ciminelli, N. Saha, G. Brunetti, A. di Toma, M. N. Armenise, "Reconfigurable Optical Beam Forming Network for Telecom Payloads," in *2024 24th International Conference on Transparent Optical Networks (ICTON), Bari, Italy, July 14-18, 2024,* pp. 1-4, doi: 10.1109/ICTON62926.2024.10647596.

[13] A. di Toma, G. Brunetti, M. N. Armenise, C. Ciminelli, "Synthetic aperture radar payloads: migration towards photonic approach," in *Small Satellites Systems and Services Symposium (4S 2024),* Palma de Mallorca, Spain, May 27-31, 2024, vol. 13546, pp. 1372-1383, doi: https://doi.org/10.1117/12.3062644.

[14] N. Saha, A. di Toma, G. Brunetti, M. N. Armenise, C. Ciminelli, "Shaping Signals in Space: Next-Gen Satellites with Reconfigurable Photonic Filters", in International Conference on Space Optics *(ICSO),* Antibes Juan-les-Pins, France, October 21-25, 2024, pp. 136996I, doi: https://doi.org/10.1117/12.3075366.

Posters

[15] A. di Toma, G. Brunetti, M. N. Armenise, C. Ciminelli, "Photonic on-board Processing," poster for the *ePIXfab 2023 – 8th Silicon Photonics Summer School*, Ghent, Belgium, July 3-7, 2023.

[16] P. Colapietro, G. Brunetti, A. di Toma, M. N. Armenise, C. Ciminelli, "Lab-On-Chip for Liquid Biopsy", poster for the *ePIXfab 2023 – 8th Silicon Photonics Summer School*, Ghent, Belgium, July 3-7, 2023.

[17] N. Saha, A. di Toma, G. Brunetti, M. N. Armenise, C. Ciminelli, "Shaping Signals in Space: Next-Gen Satellites with Reconfigurable Photonic Filters," poster for the International Conference on Space Optics *(ICSO),* Antibes Juan-les-Pins, France, October 21-25, 2024.

[18] A. di Toma, G. Brunetti, M. N. Armenise, C. Ciminelli, "Optical Intersatellite Links enabled by PCM-based Reconfigurable Photonic Beamformer," poster for the Swiss NanoConvention, Brugg, Switzerland, June 12-13, 2025.

[19] D. R. Callegari, A. di Toma, S. Iadanza, K. E. Moselund, "High Q-factor photonic crystal cavities on SiN slab," poster for the Swiss NanoConvention, Brugg, Switzerland, June 12-13, 2025.

Patent

[20] "Fully reconfigurable photonic filter in central frequency and bandwidth" pending patent.

References

[1] G. Brunetti, N. Sasanelli, N. Saha, G. Campiti, F. Hassan, A. di Toma, M. N. Armenise, C. Ciminelli, "Integrated photonics for NewSpace," in *Berta, R., De Gloria, A. (eds) Applications in Electronics Pervading Industry, Environment and Society. ApplePies 2022*. Lecture Notes in Electrical Engineering, vol 1036. Springer, Cham., 2023, https://doi.org/10.1007/978-3-031-30333-3_39

[2] Yole Group, "Silicon Photonics 2024 - Focus on SOI, SiN, and LNOI platforms", Accessed May 05, 2025. [Online]. Available: https://www.yolegroup.com/product/report/silicon-photonics-2024/

[3] European Space Agency, "Report on the Space Economy 2025," March 2025 Accessed May 05, 2025. [Online]. Available: https://space-economy.esa.int/article/287/esa-report-on-the-space-economy-2025

[4] T. R. Brashears, "Achieving 99% link uptime on a fleet of 100G space laser inter-satellite links in LEO," In *Free-Space Laser Communications XXXVI*, San Francisco, California, USA, January 27-1, 2024, vol. 12877, p. 1287702, doi: https://doi.org/10.1117/12.3005057

[5] V. Fernandez, S. Mariojouls, D. Kokkinos, "Space Photonics Unified Roadmap Airbus Space Systems Initiative SPUR Team," EPIC Meeting on Photonics for Space: Opening New Horizons, Paris, France, September 21-22, 2023. Available: https://epic-photonics.com/events/epic-meeting-on-photonics-for-space-opening-new-horizons-at-exail/

[6] T. Laurent, M. Binder, K. Nieradka, S. Ströhl, "Low Latency Global Point-to-Point Connectivity Realised with Optical Intersatellite Links", EPIC Meeting on Photonics at the Final Frontier at ESA, Noordwijk, Netherlands, September 13-14, 2022. Available: https://epic-photonics.com/wp-content/uploads/2022/04/4.8-Thomas-Laurent-Rivada.pdf

[7] J. J. Bonnefois, J. Bek, M. Collignon, G. Lecamp, C. Ollivier, N. Pirrone, A. Sekeriyan, S. Shariati, E. de Toldi, X. Weilemann, "A new compact fiber optic gyroscope for a better line of sight management," In *International Conference on Space Optics (ICSO 2022),*

Dubrovnik, Croatia. October 3–7, 2022, vol. 12777, pp. 2632-2640, doi: https://doi.org/10.1117/12.2691120.
[8] Photonics21 project, Accessed May 05, 2025. [Online]. Available: https://www.photonics21.org/
[9] Inphomir project, Accessed May 05, 2025. [Online]. Available: https://inphomir.eu/
[10] SiPhoDiAS project, Accessed May 05, 2025. [Online]. Available: https://www.space-siphodias.eu/
[11] SpaceBEAM project, Accessed May 05, 2025. [Online]. Available: https://www.spacebeam-project.eu/
[12] NASA, "Optical Communications," Accessed May 09, 2025. [Online]. Available: https://www.nasa.gov/glenn/research/optical-communications/
[13] NASA, "Spaceflight Photonics: Fiber Optics and Optoelectronics," Accessed May 09, 2025. [Online]. Available: https://etd.gsfc.nasa.gov/capabilities/capabilities-listing/spaceflight-photonics/
[14] eoPortal, "GOMX-3 (GomSpace Express-3)," Accessed May 27, 2025 [Online]. Available: https://www.eoportal.org/satellite-missions/gomx-3
[15] eoPortal, "OPS-SAT (Operations nanoSatellite)," Accessed May 27, 2025 [Online]. Available: https://www.eoportal.org/satellite-missions/ops-sat#overview
[16] G. Brunetti, N. Sasanelli, N. Saha, G. Campiti, F. Hassan, A. di Toma, M. N. Armenise, C. Ciminelli, "Integrated photonics for NewSpace," in Berta, R., De Gloria, A. (eds) Applications in Electronics Pervading Industry, Environment and Society. ApplePies 2022. Lecture Notes in Electrical Engineering, vol 1036. Springer, Cham., 2023, https://doi.org/10.1007/978-3-031-30333-3_39
[17] A.N. Bozovich "Photonic integrated circuits (PICs) for next generation space applicationsm," In 2022 NEPP Electronics Technology Workshop (ETW), Greenbelt, Massachusetts, 2022.
[18] A.N. Bozovich "Integrated Photonics Qualification Guidelines for Aerospace Applications," In 2024 NEPP Electronics Technology Workshop (ETW), Greenbelt, Massachusetts, 2024.
[19] S. V. Weston, C. D. Burkhard, J. M. Stupl, R. L. Ticknor, B. D. Yost, R. A. Austin, P. Galchenko, L. K. Newman, L. S. Soto, "State-of-the-art small spacecraft technology," 2025.
[20] K. Schauer, "NASA's Record-Breaking Laser Demo Completes Mission", Accessed June 03, 2025 [Online]. Available: https://www.nasa.gov/directorates/somd/space-communications-navigation-program/nasas-record-breaking-laser-demo-completes-mission/

Chapter 2

Shaping signals in Space with reconfigurable photonic filters

2.1 Introduction

Communication systems are a fundamental component of spacecraft, supporting mission operations by enabling data transmission, command reception, and inter-satellite information exchange. These systems are generally composed of two segments, the space segment, which includes one or more spacecraft equipped with communication payloads, and the ground segment, comprising ground stations distributed on Earth. The communication system fulfils three essential functions: uplink (receiving commands from Earth), downlink (transmitting telemetry and data to Earth), and crosslink (exchanging information between spacecraft). Two primary technologies are employed in space communication, radio frequency (RF) systems and free-space optical (FSO) systems, the latter commonly referred to as laser communications or lasercom.

Currently, most spacecraft rely on RF systems that operate within IEEE-designated bands spanning 300 MHz to 40 GHz. These systems modulate information onto electromagnetic carrier waves that propagate through space or the atmosphere, eventually reaching a receiving antenna where the signal is demodulated. RF systems are mature and widely adopted, offering robust capabilities for telemetry, tracking, and command (TT&C). Satellite communication networks, complementing terrestrial infrastructure, are increasingly critical to the development of global broadband services. Growing data demands from both governmental and commercial sectors are accelerating innovations across the communication ecosystem, driven by advances in digital platforms, cloud technologies, and evolving standards (See Figure 2.1.1). The shift toward lower latency and higher data throughput is supported by the proliferation of SmallSats and the increasing availability of reusable launch vehicles, which have significantly reduced the cost and complexity of deploying satellites in Low Earth Orbit.

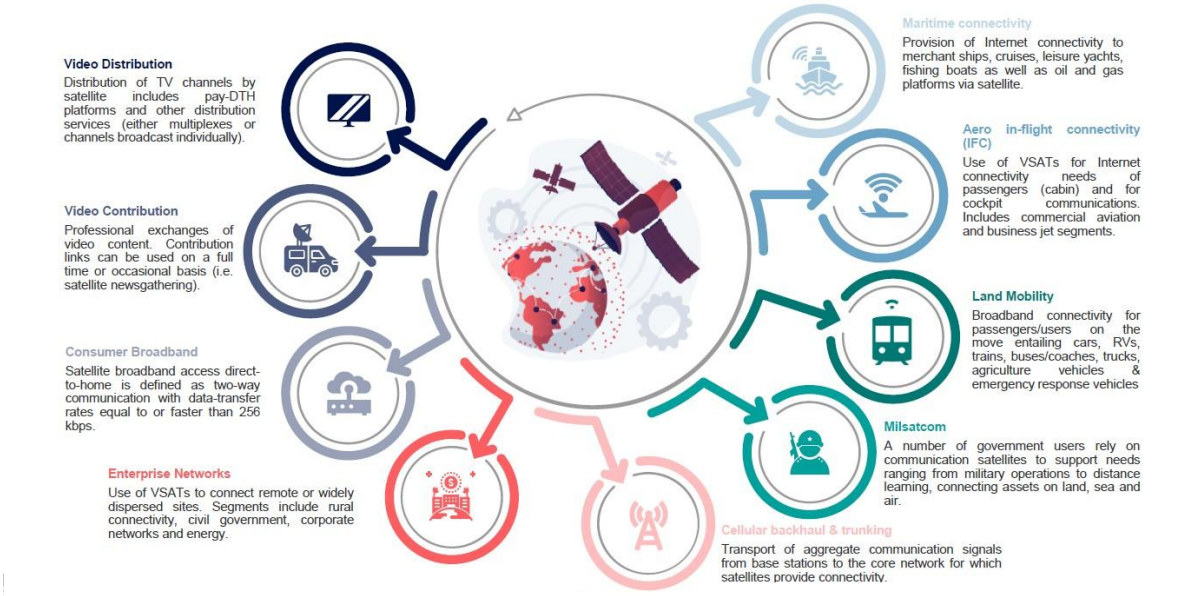

Figure 2.1.1 Satellite Communication private and institutional applications [1]

This shift aligns with the growing interest in 5G and Internet of Things (IoT) constellations. Within small satellite communications, there has been a transition from traditionally used VHF and UHF bands toward higher frequency bands such as S, X, and Ka.

However, higher frequencies demand more sophisticated hardware and link budgeting. NASA missions typically operate in government-allocated S-, X-, and Ka-bands, often utilizing the Near Space Network (NSN), which offers reduced interference and increased reliability compared to the more congested UHF spectrum [1]. S-band is particularly preferred for TT&C functions. In contrast, non-NASA missions have access to a broader array of ground communication options, ranging from low-cost, user-developed systems to commercial ground station services. Higher frequency bands like K-, Ku-, and Ka-band are becoming more prevalent in large spacecraft and are gradually entering the CubeSat domain. These higher bands offer greater data rates but also pose technical challenges, including increased free-space loss, atmospheric attenuation, and susceptibility to rain fade. Despite their challenges, especially signal degradation due to rain fade, these bands offer substantial bandwidth advantages and are the focus of ongoing development. Notable missions have demonstrated the feasibility of high-frequency CubeSat communications. For instance, NASA's ISARA mission showcased Ka-band communications with downlink rates exceeding 100 Mbps by integrating a high-gain reflectarray antenna into a CubeSat's solar array. This technology laid the groundwork for the Mars Cube One (MarCO) mission, which used twin CubeSats with X-band reflectarrays to successfully relay data from the InSight lander to Earth. Similarly, the Kepler Space Telescope employed Ka-band for high-volume downlinking, signaling a trend toward greater adoption of high-frequency systems to meet the growing data needs of future missions [2].

Projections indicate that satellite communication capacity demand will grow significantly, with estimates reaching 51 Tbps by 2032, representing a compound annual growth rate (CAGR) of 31%. Notably, the share of non-geostationary satellite

orbit (NGSO) systems is expected to increase dramatically, from 76% in 2022 to over 95% post-2026, underscoring the sector's rapid evolution toward higher-throughput, lower-latency, and more flexible communication infrastructures [3]. NASA has estimated that the transition towards photonics technology could potentially result in a data rate increase of up to 100 times. This advance would significantly enhance data collection capabilities and reduce the complexity of mission operations while offering reconfiguration capability. It would also address challenges associated with microwave spectral congestion, spectrum allocation, and the limited bandwidth (BW) typically encountered in RF communications. Indeed, future advanced satellite communication missions demand highly adaptable payloads capable of post-deployment reconfiguration to meet evolving user requirements in terms of bandwidth, coverage area, and frequency allocation. Current research in space photonics is increasingly directed toward the development of next-generation optical communication systems, which include both inter-satellite links and satellite-to-ground transmission. This research also encompasses the design of advanced optical modulators and filters to support satellite-based broadband internet access. The objective of overarching is to enable satellite links with high data rates and improved spectral efficiency, thereby supporting high-speed, reliable communications.

A critical element of a flexible telecommunications payload is the reconfigurable radio frequency (RF) front-end, which incorporates band-pass filters (BPFs) capable of dynamically adjusting their central frequency and bandwidth. This chapter is discussing innovative strategies to expand filter reconfigurability through novel integrated photonic architectures being compliant with the stringent spatial and functional requirements of telecom payloads in spaceborne systems, to fulfil the growing demand for compact, energy-efficient, and dynamically reconfigurable solutions.

2.2 Telecommunication Payload Architecture

Conventional electronic communication payloads in small satellite platforms rely on a series of discrete RF components, including modulators/demodulators, frequency mixers, amplifiers, filters, and antennas.

On the transmission side, the modulator generates, encodes, and amplifies the RF signal, while the receiving chain involves signal demodulation and decoding. Frequency translation is achieved via RF mixers, which either up-convert or down-convert signals to the appropriate frequency bands using local oscillators (LOs). Bandpass filters suppress out-of-band interference typically upstream of low-noise amplifiers (LNAs), which amplify weak incoming signals and mitigate overall system noise. High-power amplifiers (HPAs) support transmission, while antenna subsystems ensure free-space propagation, employing either omnidirectional low-gain or directional high-gain configurations based on mission-specific requirements. Cryptographic units may be included for link security and spread-spectrum modulation techniques are employed to enhance interference resilience and spectral efficiency in shared environments [3].

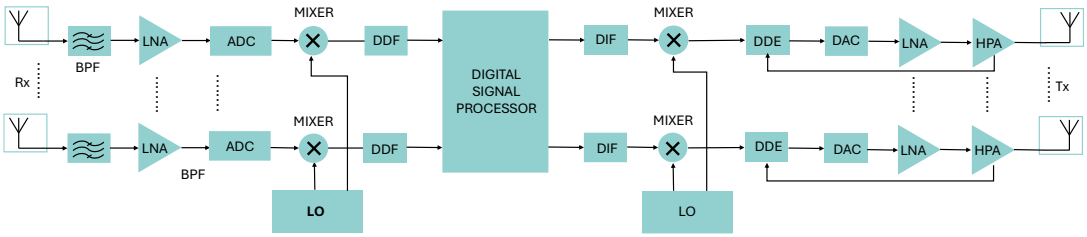

Figure 2.2.1 Electronic transceiver scheme. (Rx: receiving antenna, BPF: bandpass filter, LNA: low-noise amplifier, ADC: analog-digital converter, LO: local oscillator, DDF: digital decimation filter, DIF: digital interpolation filter, DDE: dynamic digital equalizer, DAC: digital-analog converter, HPA: high power amplifier, Tx: transmitting antenna)

However, this architecture, represented in Figure 2.2.1, presents inherent limitations in terms of scalability, spectral flexibility, and hardware complexity—particularly when managing multiple frequency channels and transmission bands. Photonic transceiver architectures have thus emerged as a compelling alternative, particularly for next-generation, high-throughput satellite communication systems constrained by size, weight, and power (SWaP) limitations.

A significant enhancement offered by photonic systems is the ability to perform multi-frequency conversion using a single Photonic Frequency Converter, thereby eliminating the need for multiple parallel RF mixers, each driven by separate local oscillators (LOs). In this architecture, LO signals are optically generated by a Photonic Frequency Generation Unit (PFGU) and fed into a Photonic Multi-Frequency Converter (PMFC). The amplified RF input from the antenna is mixed with these LO signals to perform simultaneous frequency translations across multiple channels. The resulting optical signals are then routed through an Optical Switching Matrix (OSM), which enables dynamic beam routing and reconfigurable output paths. Prior to transmission, the optical signals are detected, converted back to the electrical domain, and processed through conventional RF filtering and amplification stages before being radiated by the transmit antenna [4, 5].

This photonic-based approach, shown in Figure 2.2.2, offers several advantages over traditional architectures. By consolidating multiple frequency translation stages into a single optical unit, photonic transceivers significantly reduce system mass, volume, and power consumption. Moreover, they enable increased frequency agility, scalability, and spectral efficiency, while simplifying payload design and reducing the number of required RF components. The degree of hardware reduction achievable is directly proportional to the number of LO frequencies originally required in the RF payload, thereby offering substantial gains for complex multi-band satellite communication missions.

The Microwave Photonic Filter (MPF) serves as a critical element within next-generation photonic transceiver architecture, wherein traditional RF filters are supplanted by their photonic counterparts. In this configuration, the input RF signals are first modulated onto an optical carrier, after which the in-band signal undergoes processing entirely in the optical domain through the use of optical filters and related photonic components.

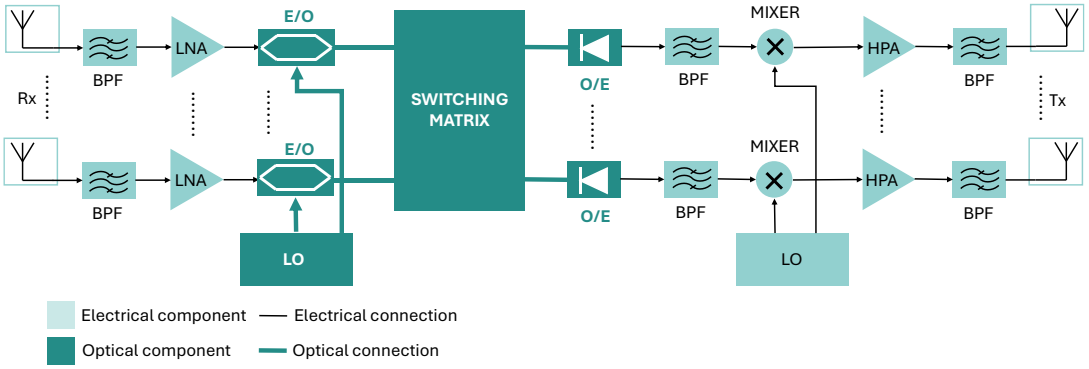

Figure 2.2.2 Electronic-Photonic transceiver scheme. (Rx: receiving antenna, BPF: bandpass filter, LNA: low-noise amplifier, E/O electro-optical converter, LO: local oscillator, O/E: opto-electronic converter, HPA: high power amplifier, Tx: transmitting antenna)

2.3 Telecom Payload requirements for Reconfigurable Filters

A fundamental step in the development of reconfigurable radio-frequency devices for space applications is the design and in-orbit validation of a reconfigurable bandpass filter. For this reason, project as the ESA/ESTEC ARTES 5 was developed, and, specifically, the activity titled "Bandpass Filter with In-Orbit Reconfigurable Bandwidth", through which the technical specifications and operational requirements of the filter were defined. The targeted filter must operate within the Ku- and Ka-band frequency ranges and must be capable of dynamically adjusting both its central frequency and bandwidth to accommodate changing mission requirements [6].

In keeping with the prevailing trend toward the miniaturization of microwave hardware for spaceborne platforms, the filter design must adopt a compact form factor. This necessitates exceptionally high positioning precision within the actuation mechanism, as even minor inaccuracies can impact performance. A key constrain of the proposed design is its low power consumption during reconfiguration, lower than 1 W, with no power required to maintain the configured state, thus enhancing energy efficiency for satellite payloads.

The filter must be capable of switching between channel bandwidths ranging from 30 MHz to 300 MHz, while supporting central frequency tuning across the 4 to 40 GHz range. Performance specifications include insertion losses below 5 dB, flat-top passband shaping with ripple less than 0.5 dB, and out-of-band rejection exceeding 30 dB. Additionally, the reconfiguration time must remain under 1 μs to enable rapid adaptability in dynamic operational scenarios.

Beyond these performance metrics, the filter must also comply with electromagnetic compatibility (EMC) standards and demonstrate operational robustness in the harsh conditions of the space environment, including tolerance to microvibrations and thermal cycling [7, 8].

The aforementioned requirements are summarized and reported in Table 2.3.1.

Table 2.3.1 Reconfigurable band-pass filter requirements

Performance	Value
Tunable central frequency (Δf_0)	4-40 GHz
Tunable bandwidth (ΔBW)	30-300 MHz
Insertion loss (IL)	< 5 dB
Bandpass ripple (δ)	< 0.5 dB
Out of band rejection (ER)	> 30 dB
Power consumption (P)	< 1 W
Reconfiguration time (Δt)	< 1 μs

2.4 Reconfigurable band-pass filter state of the art

A typical architecture of a microwave photonic (MWP) system, sketched in Figure 2.4.1, involves an optical carrier, generated by a laser source, modulated by an RF signal. The resulting modulated optical signal undergoes processing through high-speed, compact photonic integrated circuit, followed by optical-to-electrical conversion via photodetectors. An electro-optic (E/O) transducer performs the upconversion from RF to optical frequencies, while an opto-electronic (O/E) transducer, based on photodetection, realizes the downconversion to the RF domain. Signal conditioning, including spectral filtering of unwanted components, is carried out in the optical domain using integrated photonic devices. The cascade of the E/O transducer, the integrated photonic filter, and the O/E transducer constitutes the integrated microwave photonic filter (IMWPF) [9].
MWP filter architectures are commonly classified into two main categories, tapped delay line filters and coherent optical filters. In the tapped delay line configuration, the RF signal is replicated into multiple delayed and weighted copies, whose constructive and destructive interference generates the desired spectrum. This architecture can produce either a finite impulse response (FIR) when the number of taps is limited, or an infinite impulse response (IIR) when an effectively infinite number of taps is approximated, offering sharper filtering characteristics and enhanced extinction ratios [10].
However, this approach typically requires multiple discrete frequency sources, increasing system complexity and cost. To address this limitation, optical frequency combs, such as those based on microresonators, have been introduced. These comb sources enable flexible and reconfigurable tap generation. The filter configuration generally consists of a multi-wavelength source, a spectral shaper to control tap amplitude and phase, and a dispersive delay line to impose the required time delays between taps. Components such as arrayed waveguide gratings (AWGs) combined with semiconductor optical amplifiers (SOAs) can provide tunable spectral shaping, while photonic crystal-based waveguides serve as compact dispersive delay elements [11].

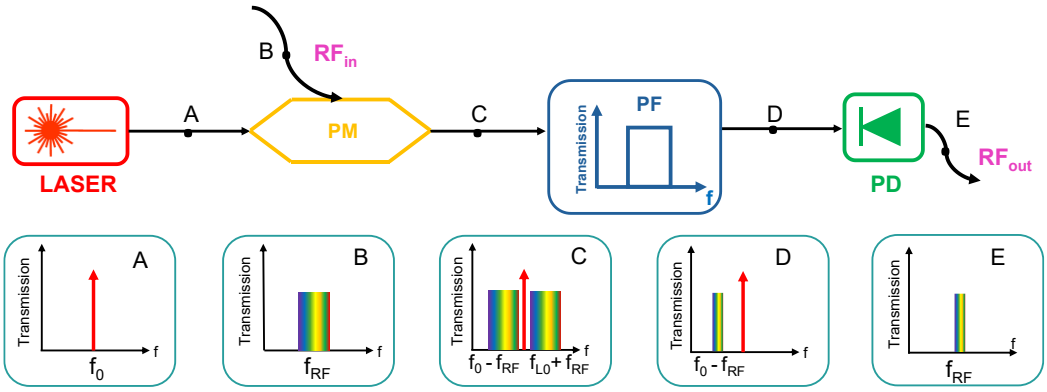

Figure 2.4.1 Integrated microwave photonic filter architecture. (PM: phase modulator, PF: photonic filter, PD: photodiode, RF_{in}/RF_{out}: input/output radio frequency signal, f_0: optical signal, f_{RF}: radio frequency signal) [12]

In contrast, coherent optical filters operate using a single-wavelength laser source and an integrated optical filter with a designed spectral response. An RF signal modulates the optical carrier through a phase modulator, generating sidebands around the carrier frequency. These sidebands are then selectively modified by the optical filter. The modified optical signal is subsequently converted back to the RF domain by a photodetector. Coherent filters offer greater flexibility and spectral reconfigurability than multitapped designs, as their RF response can be dynamically tuned by adjusting either the optical carrier or the filter's central frequency. To realize bandpass or band-stop functionalities, techniques such as single-sideband (SSB) modulation are employed, wherein the RF-to-optical spectrum mapping is achieved either by sideband filtering or by using dual-parallel Mach-Zehnder modulators (DPMZMs) or dual-drive MZMs (DDMZMs) [10].

A key requirement for next-generation MWP filters is tunability, which enables adaptable RF functionality. The two most widely adopted tuning mechanisms for optical filters are electro-optic (EO) and thermo-optic (TO) control. EO tuning offers nanosecond-scale reconfiguration speeds but is limited in tuning range, while TO tuning provides broader tuning capabilities with lower power consumption, even if with slower response times on the order of microseconds.

To meet various application-specific requirements, multiple IMWPF topologies have been proposed in the literature. These include designs based on ring resonators (RRs), subwavelength gratings (SWGs), ring-assisted Mach–Zehnder interferometers (RAMZIs), and nonlinear phenomena such as stimulated Brillouin scattering (SBS), each offering distinct trade-offs in terms of footprint, spectral resolution, tuning range, and integration complexity.

In 2022, Liu et al. [13] introduced a photonic bandpass filter (BPF) architecture based on four cascaded silicon microring resonators, featuring a coupling region with a geometrically engineered profile. The filter demonstrated tunability of its central frequency from 5.20 GHz to 35.80 GHz and bandwidth adjustability between 0.70 GHz and 2 GHz, achieved through electrical control of electrodes integrated within the coupling regions and ring segments. However, dynamic tuning of the coupling coefficient resulted in a degradation of the coupling ratio by approximately 20 dB during bandwidth adjustment.

Subsequently, in 2023, Cheng et al. [14] proposed a filter composed of two cascaded silicon nitride ring resonators, incorporating a Mach–Zehnder interferometer (MZI)

in the coupling region. This configuration enabled bandwidth reconfigurability from 0.38 GHz to 15.74 GHz and frequency tuning in the range of 4 GHz to 21.50 GHz. Despite its wide tunability, the filter exhibited a transition bandwidth roll-off of 20 dB per octave, deviating significantly from the ideal square-shaped filter response. Additionally, nonlinear optical effects have been leveraged in a ring-assisted MZI configuration [15], allowing for broad reconfigurability. However, these approaches typically involve large bandwidths, up to 26 GHz, and suffer from relatively slow roll-off characteristics, approximately 22 dB per octave, limiting spectral selectivity. Recently, a silicon-based dual-drive high-Q racetrack microring resonator (MRR) employing a multimode waveguide was developed to enable wide and fast frequency tunability through combined thermal and electrical tuning mechanisms. Integrated into a microwave photonic filter system, it demonstrated a tunable bandwidth from 1.27 to 4.47 GHz, a frequency tuning range from 3 to 51 GHz, and sub-nanosecond reconfiguration speeds. However, these capabilities came with performance trade-offs, indeed, bandwidth tuning increased insertion losses from 35 dB to 45 dB and reduced the extinction ratio (ER) from 4.95 dB to 1.63 dB, while frequency tuning involves a decrease in ER from 4.95 dB to 1.52 dB and in the meanwhile bandwidth increases [16].

2.5 Widening the filter reconfigurability exploiting novel photonic architectures

In pursuit of overcoming the limitations of current state-of-the-art solutions and addressing the evolving requirements set forth by the NewSpace economy, the European Space Agency (ESA), and commercial stakeholders in the aerospace sector, various coherent filter architectures have been investigated and simulated. This effort includes a comparative analysis of multiple tuning strategies and fabrication technologies, aimed at enhancing reconfigurability, spectral selectivity, and integration potential. The following discussion presents a critical assessment of each proposed solution, highlighting their respective advantages, limitations, and innovative contributions within the context of next-generation microwave photonic systems for space applications.

2.5.1 Independent cascaded tunable ring resonators

The proposed solution consists of a coherent microwave photonic filter architecture, in which the key functional element is an optical notch filter. This device is implemented through a cascade of two silicon ring resonators (RRs), both possessing the same radius. Each ring is individually tuned via thermo-optic tuning, enabling independent reconfiguration of both the central wavelength and the bandwidth [17]. A schematic representation of the optical filter structure is reported in Figure 2.5.1. The device is realized in Silicon-on-Insulator (SOI) technology, in which the silicon (Si) waveguides are fully embedded in silicon dioxide (SiO_2).

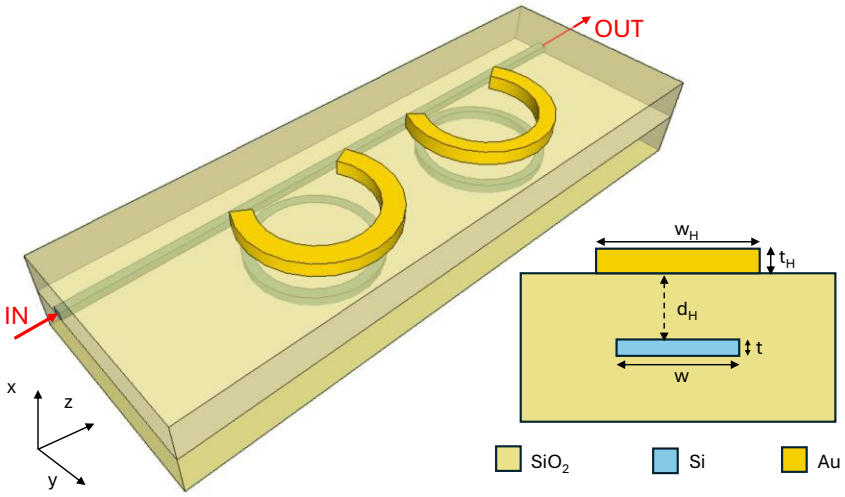

Figure 2.5.1 Independent cascaded tunable ring resonators photonic filter structure and cross-section (w: core width; t: core height; d_H: electrode-waveguide gap; w_H: electrode width; t_H: electrode height) [17]

The core width w = 440 nm and thickness t = 220 nm are selected to ensure single-mode propagation for the fundamental TE_0 mode. Modal analysis was conducted via finite element method (FEM) simulations using COMSOL Multiphysics, also incorporating the effect of waveguide dispersion. A comprehensive overview of COMSOL Multiphysics capabilities and the underlying FEM method is provided in Appendix A. This SOI technology choice is motivated by the intrinsic advantages of silicon photonics in meeting the stringent performance requirements of modern datacom and telecom applications. Silicon photonics leverages a mature and scalable CMOS-compatible fabrication infrastructure, which facilitates the transition from research-scale prototyping to industrial-scale production. Furthermore, the high refractive index contrast between silicon (n_{Si} = 3.47 at 1550 nm) and its surrounding cladding materials, such as silicon dioxide (n_{SiO_2} = 1.44), enables compact device geometries, reduces bend radii, enhances integration density, and lowers power consumption.

Recent advances in heterogeneous integration techniques, such as wafer bonding, micro-transfer printing, and hybrid integration, have enabled the co-integration of key active and passive photonic components—including high-speed germanium photodetectors, modulators, filters, wavelength routers, and even light sources—on a single silicon chip [18]. This technological maturity renders silicon a compelling material platform for the implementation of tunable filters, particularly owing to its compatibility with a variety of tuning mechanisms. These mechanisms include the plasma dispersion effect via carrier injection, accumulation, or depletion, the Pockels effect when integrated with piezoelectric materials, the Franz–Keldysh effect in germanium, and the Quantum-Confined Stark effect when employing Ge–Si–Ge quantum wells.

Although lower propagation losses have been reported in literature for the same technology and wavelength (λ = 1550 nm) [19], a conservative value of α = 0.4 dB/cm has been adopted in this work to account for additional fabrication-related loss contributions [20]. The design parameters, including the ring radius R and the power coupling coefficient K between the bus waveguide and each resonator, were optimized with the goal of maximizing stopband rejection. It was observed that an increase in R leads to a reduction in K, primarily due to enhanced bending losses.

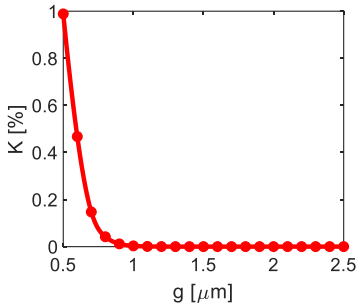

Figure 2.5.2 Power coupling coefficient (%) variation versus centre-centre gap between bus waveguide and ring resonator

To eliminate mutual coupling between the two rings, a separation of 1 μm is introduced, ensuring negligible interaction.
The *R* value is set at *R* = 10 μm, minimizing bending losses while achieving the target central wavelength of 1550 nm. In the low-coupling regime of microring resonators, a *K* value *K* = 2.24% was selected to achieve an optimal trade-off between bandwidth and stopband rejection. A physical gap of g = 710 nm between the bus waveguide and the resonator was engineered via Beam Propagation Method (BPM) parametric simulations to realize this coupling condition, as represented in Figure 2.5.2. This configuration yielded a Lorentzian-shaped notch with a stopband rejection (SBR) of approximately 45 dB and a bandwidth (BW) of 610 MHz, suitable for 5G networks.
A detailed description of the BPM is provided in Appendix B.
The optical response of the filter was modeled using the scattering matrix formalism [21]. The total system transmission coefficient, $T_{OUT} \equiv S_{21}$ is given by:

$$T_{OUT} = |t_1 \cdot t_2|^2 \quad (1)$$

where t_1 and t_2 are the S_{21} transmission coefficients of the individual ring resonators. These coefficients were derived using the analytical expression from the scattering matrix theory [22]:

$$t_{1/2} = \frac{(1-k^2)\cdot e^{j2\pi R\beta} - \sqrt{1-k^2} + k^2 \cdot e^{j2\pi R\beta}}{\sqrt{1-k^2}\cdot e^{j2\pi R\beta} - 1} \quad (2)$$

Here, k denotes the amplitude coupling coefficient, $\tau = \sqrt{1-K}$ is the amplitude transmission coefficient, and $\beta = \frac{2\pi}{\lambda} n_{eff} - j\alpha$ is the complex propagation constant. The same R value is assumed for both resonators. The effective refractive index n_{eff} is computed using FEM simulations in COMSOL Multiphysics, incorporating both Sellmeier dispersion relations and the thermal effects induced by the TO phase shifters. A comprehensive description of the scattering matrix theory is presented in Appendix C.
The variation in n_{eff} due to the TO phase shifters is quantitatively estimated through the coupled thermal-optical simulation framework, allowing for precise evaluation of both central frequency and bandwidth tuning capabilities.
Indeed, the optical filter reconfigurability is achieved by modifying the effective refractive index n_{eff} of the guided mode. The two principal mechanisms that can be employed are the thermo-optic (TO) [23] and the electro-optic (EO) effects [24]. In

this work, TO tuning is exploited through the use of titanium nitride (TiN) heaters positioned in proximity to the waveguide core. These heaters are resistively powered, generating localized heating via the Joule effect, which induces a refractive index change in the silicon waveguide, proportional to its high thermo-optic coefficient $dn/dT = 1.80 \cdot 10^{-4}$ a.u. in C band band [25].

Two TiN electrodes, each with thickness t_H and width w_H, are placed above the ring resonators with a vertical separation d_H from the Si core (as shown in Figure 2.5.1). Although thicker metal heaters increase tuning efficiency, power consumption constraints restrict t_H to 100 nm. Furthermore, to prevent unintended modulation of the k, the metal heaters are strategically positioned away from the coupling regions. Identical tuning lengths are assigned to both ring resonators to maintain symmetry. The total length of each heater is 25.12 μm, ensuring no heater coverage over the coupling regions, which are assumed to occupy approximately 20% of the total resonator length.

The d_H value must be optimized to balance tuning efficiency against optical absorption losses due to proximity to the metal. Lower d_H values enhance thermal efficiency but increase losses. An important performance metric is the phase shifter's response time τ_H, typically defined as the 10–90% (rise) or 90–10% (fall) transition time of the output signal in response to a step input. The filter design process involved the joint use of a thermal solver and an optical mode solver, enabling the simulation of heat distribution, thermal efficiency, and transient response. Simulations assumed an ambient temperature of 300 K and adopted thermal material parameters of 0.8 J/g°C and 150 W/mK for silicon, 0.8 J/g°C and 1.5 W/mK for SiO_2, and 0.5 J/g°C and 30 W/mK for TiN.

The design of d_H and w_H is optimized to reduce power consumption and minimize the figure of merit (FOM), defined as $FOM = P_\pi \cdot \tau_H$ where P_π is the electrical power required to induce a π phase shift. Reducing w_H lowers P_π while preserving τ_H, similarly, increasing d_H improves thermal isolation and reduces P_π, although it may degrade efficiency. A final choice of $w_H = 0.8$ μm and $d_H = 0.4$ μm yielded $\tau_H = 5.34$ μs and $P_\pi = 19.7$ mW, in agreement with experimental benchmarks reported in the literature [26]. The temperature distribution in the cross-section of the phase shifter and its time response are represented in Figure 2.5.3(a) and (b), respectively. In particular, Figure 2.5.3(b) shows the normalized injected current step used to induce the Joule effect, along with the corresponding normalized temperature variation in the waveguide core.

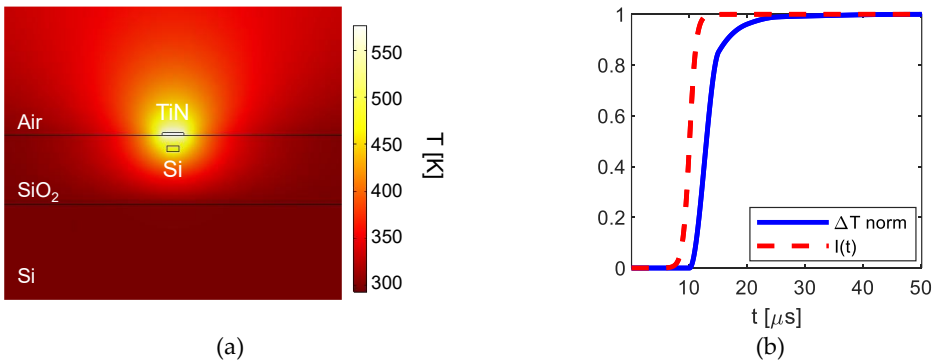

(a) (b)

Figure 2.5.3 Thermo-optical tuning mechanism. (a) The temperature distribution in the cross-section of the phase shifter (b) The temperature variation versus time in the waveguide core when the heater is fed ($0 \rightarrow P_\pi$)

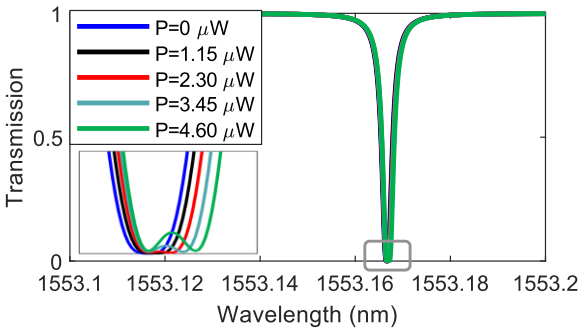

Figure 2.5.4 Photonic filter spectra vs. power (P) fed second RR. The inset represents a zoom on the stopband region [17]

By modulating the electrical power supplied to either one or both RRs, it is possible to independently adjust the filter's bandwidth or central frequency, respectively. Specifically, applying an electrical power ranging from 0 to 4.60 μW to the second RR enables the bandwidth to be increased from approximately 500 MHz to 520 MHz, while preserving the stopband rejection ratio (SBR) at 45 dB. This bandwidth broadening is attributed to the red shift of the resonance peak of the second RR, which, due to the cascaded configuration, results in an overall expansion of the filter's transmission envelope. A minor consequence of this shift is a variation of the central frequency by about 37 MHz, as illustrated in Figure 2.5.4. However, increasing the supplied current beyond this range, although effective in further broadening the bandwidth, also induces in-band ripple, thus compromising the spectral flatness of the filter response (as shown in the inset of Figure 2.5.4).

In contrast, if central frequency tuning is desired without affecting the bandwidth, both RRs must be simultaneously and equally tuned. This symmetric tuning enables the resonance peaks to shift together while maintaining their relative alignment, thereby ensuring constant bandwidth. The Free Spectral Range (FSR) of the two resonators is sufficiently large to prevent resonance overlap for electrical power values up to 11.50 mW, allowing for a maximum central frequency shift of approximately 180 MHz, as shown in Figure 2.5.5. However, the extent of this frequency shift is inherently constrained by the thermo-optic tuning mechanism. Elevated power levels, while enhancing tunability, inevitably introduce higher propagation losses, which degrade both the bandwidth and SBR performance.

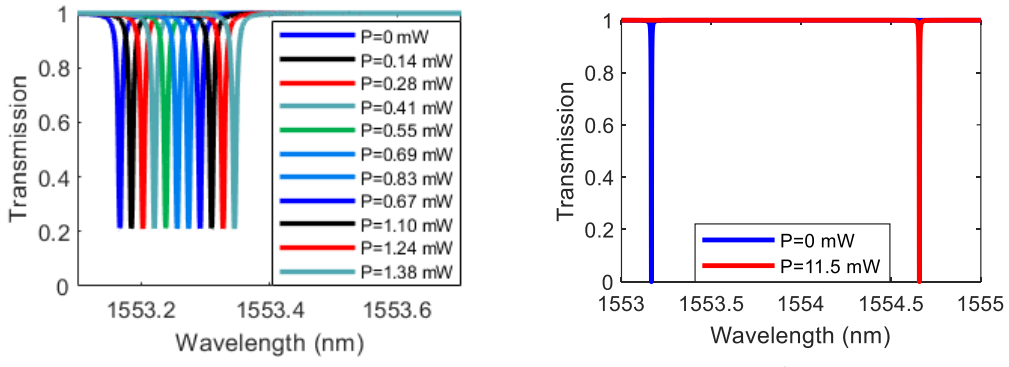

(a) (b)

Figure 2.5.5 (a) Photonic filter spectra vs. power (P) fed to both RRs; (b) Photonic filter spectra at the power (P) range ends [17]

During device operation, the applied electrical power may deviate from its nominal values due to practical implementation constraints. However, such variations have a limited impact on overall device performance. Specifically, the relationship between the applied electrical power and the resulting bandwidth exhibits a parabolic behavior. For instance, when the maximum bandwidth of 520 MHz—achieved at an optimal power value of 4.60 μW—is targeted, rounding the power value to the nearest integer results in a bandwidth variation between 515 MHz and 530 MHz, while maintaining acceptable ripple characteristics. In the case of central frequency tuning, rounding the electrical power does not present a significant issue, as the resulting central frequency remains well within the designed tuning range.

Regarding the coupling region, a value of 2.24% is achieved by setting the bus-to-ring gap to 710 nm. Accounting for typical fabrication tolerances of ±10 nm, the coupling coefficient is expected to vary by approximately $\pm 1.4 \times 10^{-3}$. This variation may influence key performance parameters of the individual resonator, including the stopband rejection—which may range from 34 dB to 72 dB—and the bandwidth, which could fluctuate between 472 MHz and 534 MHz.

The sensitivity of the filter's performance to fabrication process variations is also investigated. Tolerances of ±10 nm in g, R, and w were individually assessed to isolate the influence of each parameter on central wavelength, bandwidth, and stopband rejection.

The most critical condition—corresponding to the first ring with w = 430 nm, R = 10 μm - 10 nm, and g = 700 nm, and the second ring with w = 450 nm, R = 10 μm + 10 nm, and g = 720 nm—produces the largest deviation between the two RRs. Nonetheless, even in this worst-case scenario, a bandwidth of 510 MHz and a stopband rejection of 49 dB are obtained, demonstrating the robustness of the proposed design against fabrication tolerances.

Here, it is proposed and validated a fully reconfigurable microwave photonic filter based on two thermally tunable and decoupled silicon ring resonators. The architecture allows independent control over the bandwidth and central frequency using electrical power ranging from 0 to 11.50 mW, thanks to the efficient thermo-optic tuning properties of silicon. The filter demonstrates a stopband rejection as high as 45 dB and is capable of achieving a 20 MHz bandwidth tuning range through single-ring actuation and a central frequency tuning range of up to 180 MHz when both rings are symmetrically tuned. Although the tuning speed is relatively slow (5 μs), the proposed device strikes an effective balance between performance, power efficiency, and scalability, making it well-suited for next-generation reconfigurable photonic systems. The proposed filter successfully satisfies many of the performance criteria listed in Table 2.3.1, including an in-band ripple of less than 0.5 dB, a stopband rejection of 45 dB, and low power consumption (0–11.50 mW), while maintaining a compact and simplified architecture compatible with the constraints imposed by the NewSpace Economy. The primary limitation in reconfigurability arises from the use of the thermo-optic effect, which, although efficient and CMOS-compatible, inherently requires high thermal energy to achieve large index shifts. Consequently, higher powers lead to increased losses, adversely affecting bandwidth and SBR. In response, ongoing research is exploring alternative tuning mechanisms that offer improved performance. For example, the electro-optic (EO)

effect allows for rapid reconfiguration and low power operation but typically suffers from limited tunability and more complex fabrication requirements [24].
Among the most promising approaches for future development is the use of nonvolatile phase-change materials. These materials enable persistent and reconfigurable optical responses without continuous power consumption and are currently under investigation for a wide range of integrated photonic applications, including switches, filters, lenses, absorbers, and sensors [27]. Their integration could pave the way toward fully reconfigurable and energy-efficient microwave photonic subsystems, fulfilling the requirements for a tunable bandpass filter and advancing the development of flexible photonic telecommunication payloads.

2.5.2 Cascaded CROW architecture

The photonic filter (PF) proposed here is implemented on a low-loss TriPleX™ waveguide platform, represented in the inset of Figure 2.5.6, which employs a double-layer silicon nitride (Si_3N_4) core structure fully embedded in silicon dioxide (SiO_2), as detailed in [28]. This waveguide configuration enables low propagation losses while maintaining compatibility with standard fabrication processes.
The architecture of the PF, shown in Figure 2.5.6, comprises two cascaded coupled-resonator optical waveguides (CROWs). Each CROW contains two racetrack-shaped resonators (RTRRs), designated RTRR1 and RTRR2. RTRR2 is the resonator directly adjacent to the bus waveguide, while RTRR1 is positioned externally.
To minimize bending losses and simplify the fabrication process, each racetrack features a bending radius of 350 µm— significantly larger than the 100 µm lower limit demonstrated for the TriPleX platform [29]. For a conservative analysis that accounts for potential fabrication imperfections, the propagation loss is assumed to be 0.5 dB/cm, which is higher than typical values reported for TriPleX waveguides.
Coupling of optical power within each CROW is facilitated by integrated directional couplers. Specifically, a two-waveguide directional coupler (2WG-DC) couples light from the bus waveguide into RTRR2, while a three-waveguide directional coupler (3WG-DC) enables coupling between RTRR1 and RTRR2.

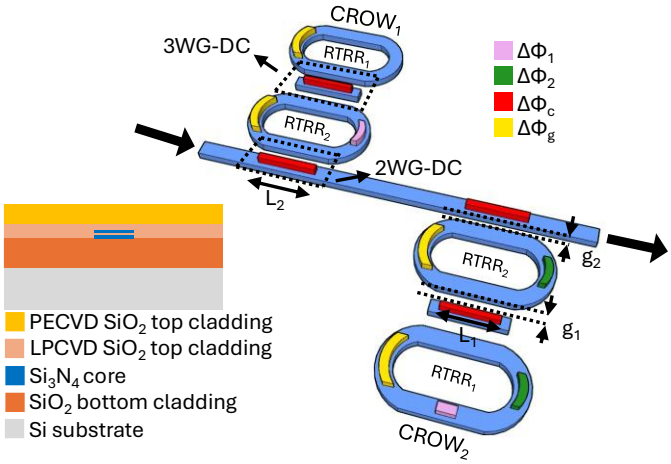

Figure 2.5.6 Cascaded CROWs reconfigurable photonic filter architecture (RTRR: racetrack resonator; 2WG-DC: two-waveguide directional coupler; 3WG-DC: three-waveguide directional coupler, *L*: coupling length; *g*: waveguide gap; $\Delta\Phi$: phase shifter). The inset represents the technological platform cross-section

To provide tunability and control over the filter's spectral characteristics, phase-change material (PCM) based phase shifters are incorporated into the structure. The material chosen is GeSe, which exhibits a refractive index of 2.4 in the amorphous state and 2.97 in the crystalline one at 1550nm. In both phases, the extinction coefficient remains low, on the order of 6×10^{-6}, thereby ensuring minimal optical absorption [28]. Phase shifters labeled $\Delta\phi_c$ (red in Figure 2.5.6) are situated above the directional couplers to tune the power distribution between the resonators. Additional phase shifters, $\Delta\phi_g$ (yellow), are positioned on top of each RTRR to adjust the resonance wavelength. Furthermore, $\Delta\phi_1$ and $\Delta\phi_2$ (pink and green, respectively) serve to fine-tune the overall bandwidth and extinction ratio of the filter. All PCM-based shifters are designed with a width of 500 nm and a thickness of 10 nm [29, 30]. The optical behavior of the proposed structure is rigorously analyzed using the transfer matrix method (TMM) [12], supported by modal profiles obtained through finite element method (FEM) simulations. The performance of the directional couplers is independently evaluated using coupled mode theory (CMT). Detailed descriptions of both TMM and CMT are provided in Appendix C and Appendix D, respectively. Wavelength-dependent refractive index dispersion for the Si_3N_4 and SiO_2 layers is incorporated through their respective Sellmeier equations to ensure accurate modeling of spectral responses.

The optimization of the proposed photonic filter begins with the two directional couplers, which are critical to achieving efficient optical power transfer both from the bus waveguide to RTRR2 and between the two resonators in each CROW. To satisfy the phase-matching condition, the width of the bus waveguide is fixed at 1.01 μm in both couplers. For the two-waveguide directional coupler (2WG-DC), the coupling length L_2 and gap g_2 are designed such that, in the PCM amorphous state, the coupling length is twice that in the crystalline state. This ensures complete power transfer to RTRR2 in the amorphous phase and to the bus waveguide in the crystalline one. The optimization performed by employing the CMT leads to L_2 = 205 μm and g_2 = 1.2 μm. Additionally, arbitrary coupling ratios can then be achieved via partial crystallization of the PCM. Indeed, by properly modifying the energy and number of light pulses applied to PCMs, it occurs a platform broadband attenuation and optical phase modulation effect, enabling a non-volatile quasi-continuous tuning through the thermo-optical induction of a phase change [31].

Similarly, for the three-waveguide directional coupler (3WG-DC), parametric CMT simulations yield optimal values of L_1 = 195 μm and g_1 = 0.5 μm, allowing the device to mimic the behavior of a 2WG-DC. This configuration ensures efficient coupling between RTRR1 and RTRR2 while minimizing unintended coupling to the central waveguide.

The coupling coefficients of both couplers significantly influence the spectral shape of the filter. Depending on these coefficients, the transmission spectrum can exhibit a bell-shaped, split, or flat-bottom profile. To obtain a flat-bottom response with minimal ripple (< 0.1 dB), the self-coupling coefficients κ_2 and κ_1 (corresponding to the 2WG-DC and 3WG-DC, respectively) must satisfy the following relationship, derived through parametric analysis

$$\kappa_2 = 23.45\kappa_1^4 - 59.61\kappa_1^3 + 56.94\kappa_1^2 - 23.64\kappa_1 + 3.7 \quad (3)$$

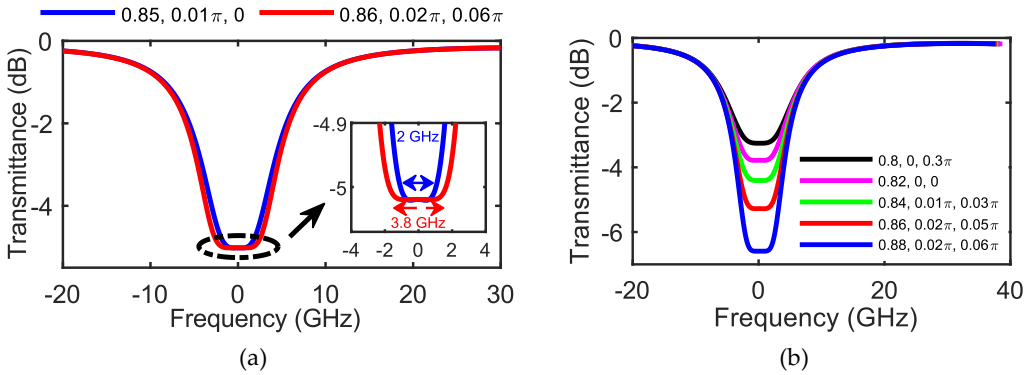

(a) (b)

Figure 2.5.7 The variation of bandwidth (a) and ER (b) through controlling the relevant phase shifters ($|\kappa_1|^2$, $\Delta\phi_1$ and $\Delta\phi_2$) [12]

These coefficients are dynamically tuned using the $\Delta\phi_a$ phase shifters, which exploit partial crystallization of the GeSe layer to modulate the effective refractive index, while the physical gaps remain fixed.

Simultaneous control over the operating bandwidth and extinction ratio (ER) of the flat-bottom band-stop filter is achieved using $\Delta\phi_c$ in conjunction with two additional phase shifters, $\Delta\phi_1$ and $\Delta\phi_2$. Figure 2.5.7(a) illustrates the transmission spectra for two different parameter combinations. These examples demonstrate that the flat-bottom bandwidth can be varied from 2 GHz to 3.8 GHz while maintaining a fixed ER of 5 dB. The $\Delta\phi_2$ shifter introduces a relative spectral shift between the two CROWs, which can distort the filter profile.

Therefore, $\Delta\phi_1$ is employed to correct the spectral envelope and preserve the flat-bottom shape. The lengths of $\Delta\phi_1$ and $\Delta\phi_2$ are set to 10 μm and 15 μm, respectively, to enable the full tuning range without compromising spectral integrity. In Figure 2.5.7(b), the ER is varied while maintaining a constant bandwidth of 3 GHz. This is accomplished by adjusting $|\kappa_1|^2$, while the $\Delta\phi_1$ and $\Delta\phi_2$ values are held constant to stabilize the bandwidth. The proper combination among phase shifts and self-coupling coefficients to achieve the desired filter response can be automated using electronic control systems, as demonstrated in [32].

The proposed device has been designed in compliance with the TriPleX technological platform —waveguide width W =1.1 μm, layer heights H_1 = 75 nm and H_2 = 175 nm, an inter-stack gap g = 100 nm, an etching angle of 82°, and a minimum bending radius of 350 nm — considering established fabrication constraints and performance benchmarks reported in the literature [33].

A tolerance analysis has been conducted to assess the robustness of the design against fabrication-induced dimensional variations. Specifically, simultaneous deviations of ±10 nm in waveguide width, layer heights, and gap are considered, consistent with standard electron-beam lithography and etching processes. The resulting changes in the effective refractive index induce a blue shift of approximately 45 GHz in the worst case, while the spectral response shape remains preserved. The combined impact on performance metrics of geometrical waveguide changes together with a ±1‰ variation in the coupling coefficient is minimal, leading to an estimated variation of the extinction ratio limited to ∓1%. Overall, these results demonstrate that the proposed device exhibits strong tolerance to realistic fabrication imperfections and is well suited for reliable implementation on the TriPleX platform.

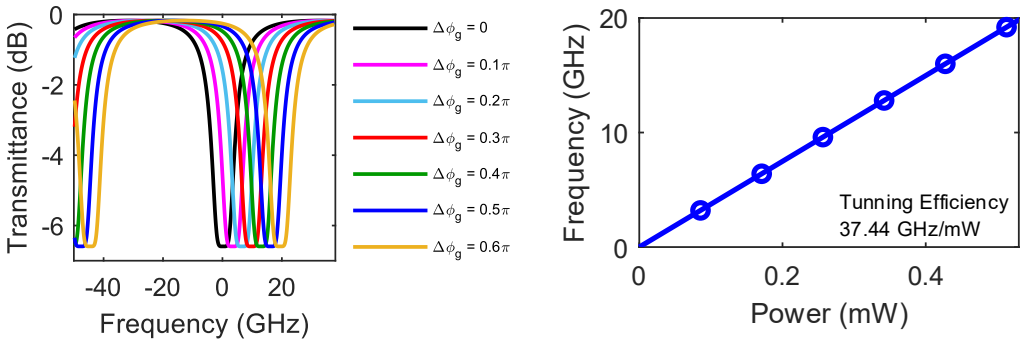

(a) (b)

Figure 2.5.8 (a) Central frequency shift tuning the phase shifter $\Delta\phi g$ (b) Central frequency shift vs peak power applied [12]

Spectral tuning of the central frequency is realized using the $\Delta\phi_g$ phase shifters, which are positioned directly atop the resonators to locally adjust the effective refractive index. This shift alters the phase-matching condition and consequently tunes the resonance frequency.

Figure 2.5.8(a) shows the transmission spectra for seven values of $\Delta\phi_g$, revealing a central frequency shift of nearly 20 GHz as $\Delta\phi_g$ varies from 0 to 0.6π. Throughout this tuning range, both the bandwidth and ER remain constant at 3 GHz and 6.6 dB, respectively. These values are maintained by fixing $|\kappa_1|^2 = 0.88$, $\Delta\phi_1 = 0.02\pi$, and $\Delta\phi_2 = 0.06\pi$, as shown in Figure 2.5.8(a).

A key advantage of using non-volatile materials like GeSe is that the programmed state is retained without any static power consumption. Once programmed, spectral tuning can be achieved solely through dynamic modulation of the $\Delta\phi_g$ phase shifters. To actively modulate the phase of the PCM, a 30 nm thick indium tin oxide (ITO) layer, 2 µm wide, is deposited atop the PCM with a 1.5 µm spacing to minimize insertion losses. Electrical pulses are delivered through this ITO electrode to control the crystallization of GeSe. Full crystallization requires the PCM to be heated above 275 °C for approximately 100 ns [29]. Partial crystallization can be finely tuned by adjusting either the pulse voltage or its duration [34].

The tuning efficiency of the proposed structure is calculated to be 37.44 GHz/mW, as shown in Figure 2.5.8(b), confirming the excellent power efficiency of the filter architecture.

This work introduces a reconfigurable photonic filter architecture based on two cascaded coupled-resonator optical waveguides (CROWs), each composed of a pair of racetrack resonators (RTRRs) integrated on a low-loss TriPleX platform. A key innovation lies in the strategic placement of PCM-based phase shifters, which enable simultaneous control over the filter's flat-top bandwidth, extinction ratio, and central frequency. Specifically, the design achieves a tunable bandwidth range of 2 GHz, an ER reconfigurability of 3.5 dB, and central frequency tuning over 20 GHz, all with a remarkably high tuning efficiency of 37.4 GHz/mW.

This level of spectral agility combined with the inherent low-loss and non-volatile characteristics of the PCM marks a significant advancement in photonic signal processing. The proposed filter is particularly suited for high-frequency telecommunications applications, including radio astronomy, microwave radio relay systems, remote sensing, and next-generation wireless LANs (e.g., IEEE

802.11ad). Its ability to provide dynamic, real-time spectral reconfiguration surpasses the flexibility and speed limitations of electronic counterparts.
By enabling compact, power-efficient, and ultra-fast tuning, this architecture holds strong promise for integration into satellite communication payloads. It supports the development of agile and lightweight systems capable of adapting to rapidly changing spectral environments, an essential requirement for modern high-capacity, multi-service satellite platforms.

2.6 Conclusions

In this chapter, innovative architectures for reconfigurable microwave photonic band-pass filters have been proposed and critically assessed in light of the stringent requirements of the NewSpace economy and the needs of next-generation satellite communication systems. The focus has been placed on improving spectral selectivity, enhancing reconfigurability, and ensuring compliance with SWaP constraints while advancing integration potential on scalable photonic platforms.

The first solution investigated relies on two thermally tunable and decoupled silicon ring resonators, demonstrating independent control of both central frequency and bandwidth with electrical powers ranging from 0 to 11.50 mW. This device achieves a stopband rejection of 45 dB, a 20 MHz bandwidth tuning range, and a central frequency reconfigurability of up to 180 MHz. Despite its relatively slow tuning speed (≈ 5 μs), the filter combines high selectivity, low in-band ripple (< 0.5 dB), and compact footprint, making it a strong candidate for low-power reconfigurable payloads. Its main limitation stems from the thermo-optic effect itself, which requires higher thermal energies for larger index shifts, inevitably increasing optical losses.

Building upon this, a second architecture based on cascaded coupled-resonator optical waveguides (CROWs) with racetrack resonators (RTRRs) on a low-loss TriPleX platform has been proposed. By incorporating PCM-based phase shifters, the filter demonstrates simultaneous reconfigurability of flat-top bandwidth, extinction ratio, and central frequency. The simulated performance includes a tunable bandwidth of 2 GHz, extinction ratio control of 3.5 dB, and central frequency tuning across a wide 20 GHz range, all achieved with a remarkable tuning efficiency of 37.4 GHz/mW. The use of PCM ensures both ultra-fast operation and non-volatility, allowing the filter to maintain its state without continuous power consumption. These attributes make the architecture particularly attractive for applications requiring spectral agility and adaptability, such as radio astronomy, remote sensing, high-capacity wireless links, and next-generation satellite payloads.

A further advancement is represented by the design of a fully reconfigurable microwave photonic band-pass filter capable of independent and simultaneous tuning of bandwidth and central frequency, without preserving a flat-top spectral profile. By leveraging the capability of PCMs to achieve quasi-continuous refractive index variation between amorphous and crystalline states, the filter pending patent

enables a quasi-continuous frequency tuning ranging from 0.91 GHz to 101.93 GHz with respect to the mid-state condition, while maintaining a stable bandwidth. Moreover, by selectively activating specific combinations of PCM tunable regions, the filter bandwidth can be adjusted from 0.87 MHz to 295 MHz, without altering the central frequency. Importantly, proper activation patterns of the PCM regions allow simultaneous reconfiguration of both bandwidth and central frequency, providing an unprecedented level of control and versatility for integrated microwave photonic filters. This architecture represents a significant step toward achieving continuous, non-volatile, and energy-efficient reconfiguration in photonic subsystems for satellite payloads.

Taken together, the results presented in this chapter highlight a clear evolution of microwave photonic filtering technologies—from thermally tuned, low-power, high-rejection filters toward PCM-based, high-speed, and spectrally agile architectures. Beyond their technical performance, these devices demonstrate compatibility with scalable photonic integration platforms such as silicon and TriPleX, effectively addressing the critical challenges of compactness, energy efficiency, and radiation resilience required for future space missions.

Overall, the findings of this chapter confirm that reconfigurable photonic band-pass filters represent a pivotal enabling technology for flexible telecommunication payloads. Future research will likely focus on the full exploitation of phase-change materials, the adoption of novel electro-optic tuning mechanisms, and hybrid integration strategies that jointly optimize speed, tunability, and power efficiency. These advancements will lay the groundwork for the next generation of fully reconfigurable, adaptive, and intelligent satellite systems that embody the principles of the NewSpace paradigm.

References

[1] Novaspace, “Satellite Connectivity & Video Market 2024,” Report, September 2024.

[2] S. V. Weston, C. D. Burkhard, J. M. Stupl, R. L. Ticknor, B. D. Yost, R. A. Austin, P. Galchenko, L. K. Newman, L. S. Soto, “State-of-the-art small spacecraft technology,” 2025.

[3] Novaspace, “Satcom and Connectivity,” Accessed June 06, 2025 [Online]. Available: https://nova.space/markets/satcom-and-connectivity/

[4] J. Anzalchi, J. Wonga, T. Vergesb, O. Navasquilloc, T. Mengualc, M. A. Piquerasc, E. Prevostd, K. Raveld, N. Parsonse, M. Enricoe, J. Bauwelinkf, M. Vanhoeckef, A. Vannuccig, M. Tienfortig, “Towards demonstration of photonic payload for telecom satellites,” In *International Conference on Space Optics (ICSO), Chania, Greece, October 9-12, 2018*, pp. 1805-1813, doi: https://doi.org/10.1117/12.2536092.

[5] C. Ciminelli, F. Dell’Olio, G. Brunetti, A. Di Benedetto, M. N. Armenise, “Integrated microphotonic switching matrices for flexible and broadband telecom satellite payloads,” In *2019 21st International Conference on Transparent Optical Networks (ICTON), Angers, France, July 9-13, 2019*, pp. 1-4, doi: 10.1109/ICTON.2019.8840425.

[6] ESA, “Photonic RF Filtering,” Report, June 2017. Accessed July 17, 2025 [Online]. Available: https://www.esa.int/Enabling_Support/Space_Engineering_Technology/Shaping_the_Future/Photonic_RF_Filtering

[7] N. Sidiropoulos, L. Scialino, A. Morini, G. Venanzoni, P. M. Iglesias, C. Ernst, "Bandpass Filter With In-Orbit Reconfigurable Bandwidth," In *31st AIAA International Communications Satellite Systems Conference, Florence, Italy, October 14-17, 2013*, p. 5681, doi: 10.2514/6.2013-5681.

[8] M. Sotom, B. Benazet, A. Le Kernec, M. Maignan, "Microwave photonic technologies for flexible satellite telecom payloads," In *European Conference on Optical Communication, Vienna, Austria, 20-24 September 2009*, pp. 20-24, doi: https://ieeexplore.ieee.org/document/5287335.

[9] N. Saha, G. Brunetti, A. di Toma, M. N. Armenise, C. Ciminelli, "Silicon Photonic filters: A pathway from basics to applications," *Advanced Photonics Research*, vol. 5, no. 10, p. 2300343, 2024, doi: https://doi.org/10.1002/adpr.202300343.

[10] D. Marpaung, J. Yao, J. Capmany, "Integrated microwave photonics," *Nature photonics*, vol. 13, no. 2, pp. 80-90, doi: https://doi.org/10.1038/s41566-018-0310-5.

[11] J. Sancho, J. Bourderionnet, J. Lloret, S. Combrié, I. Gasulla, S. Xavier, S. Sales, P. Colman, G. Lehoucq, D. Dolfi, J. Capmany, "Integrable microwave filter based on a photonic crystal delay line," *Nature communications*, vol. 3, no. 1, p. 1075, 2012, doi: 10.1038/ncomms2092.

[12] N. Saha, A. di Toma, G. Brunetti, M. N. Armenise, C. Ciminelli, "Shaping Signals in Space: Next-Gen Satellites with Reconfigurable Photonic Filters", in *International Conference on Space Optics (ICSO),* Antibes Juan-les-Pins, France, October 21-25, 2024, pp. 136996I, doi: https://doi.org/10.1117/12.3075366.

[13] Y. Liu, Y. Chen, L. Wang, Y. Yu, Y. Yu, X. Zhang, "Tunable and Reconfigurable microwave photonic bandpass filter based on cascaded silicon microring resonators," *Journal of Lightwave Technology*, vol .40, no. 14, pp. 4655–4662, 2022, doi: 10.1109/JLT.2022.3169723

[14] W. Cheng, D. Lin, P. Wang, S. Shi, M. Lu, J. Wang, C. Guo, Y. Chen, Z. Cang, Z. Tian, Z. Liang, G. Hu, B. Yun "Tunable bandpass microwave photonic filter with largely reconfigurable bandwidth and steep shape factor based on cascaded silicon nitride micro-ring resonators," *Optics Express*, vol 31, no. 16, pp. 25648–25661, 2023, doi: https://doi.org/10.1364/OE.496771.

[15] Y. Ren, D. Perron, F. Aurangozeb, Z. Jiang, M. Hossain, V. Van, "Silicon photonic Vernier cascaded microring filter for broadband tunability," *IEEE Photonics Technology Letters*, vol. 31, no. 18, pp. 1503–1506, 2019, doi: 10.1109/LPT.2019.2935412.

[16] W. Zhang, Y. Jiang, Y. Liu, B. Wang, B. "Fully tunable microwave photonic narrow bandpass filter using an on-chip dual-drive microring resonator," *Optics Express*, vol. 32, no. 18, pp. 31043-31054, 2024, doi: https://doi.org/10.1364/OE.532860.

[17] A. di Toma, G. Brunetti, N. Saha, C. Ciminelli, "Fully reconfigurable photonic filter for flexible payloads," *Applied Sciences*, vol. 14, no. 2, p. 488, 2024, doi: https://doi.org/10.3390/app14020488.

[18] A. Rahim, T. Spuesens, R. Baets, W. Bogaerts, "Open-access silicon photonics: Current status and emerging initiatives," In Proceedings of the IEEE, vol. 106, no. 12, pp. 2313-2330, 2018, doi: 10.1109/JPROC.2018.2878686.

[19] K. Solehmainen, T. Aalto, J. Dekker, M. Kapulainen, M. Harjanne, K. Kukli, P. Heimala, K. Kolari, M. Leskelä, "Dry-etched silicon-on-insulator waveguides with low propagation and fiber-coupling losses," *Journal of Lightwave Technology*, vol. 23, no. 11 p. 3875, 2015, doi: 10.1109/JLT.2005.857750.

[20] T. Horikawa, D. Shimura, T. Mogami, "Low-loss silicon wire waveguides for optical integrated circuits," *MRS Communication*, vol. 6, no. 1, pp. 9-15, 2016, doi: https://doi.org/10.1557/mrc.2015.84.

[21] M. Born, E. Wolf, "Principles of optics: electromagnetic theory of propagation, interference and diffraction of light," 6th Ed., Oxford, United Kingdom: Pergamon Press, 2013.

[22] A. Yariv, "Critical coupling and its control in optical waveguide-ring resonator systems," *IEEE Photonics Technology Letters*, vol. 14, no. 4, pp. 483-485, 2002, doi: 10.1109/68.992585.

[23] A. H. Atabaki, E. S. Hosseini, A. A., Eftekhar, S. Yegnanarayanan, A. Adibi, "Optimization of metallic microheaters for high-speed reconfigurable silicon photonics," *Optics Express*, vol. 18, no. 17, pp. 18312-18323, 2010, doi: https://doi.org/10.1364/OE.18.018312.

[24] G. Brunetti, F. Dell'Olio, D. Conteduca, M. N. Armenise, C. Ciminelli, "Ultra-Compact Tuneable Notch Filter Using Silicon Photonic Crystal Ring Resonator," *Journal of Lightwave Technology*, vol. 37, no. 13, pp. 2970-2980, 2019, doi: 10.1109/JLT.2019.2908364.

[25] N. Saha, G. Brunetti, M. N. Armenise, C. Ciminelli, "Tuneable narrow band add-drop filter design based on apodized long period waveguide grating assisted co-directional coupler," *Optics Express*, vol. 30, no. 16, pp. 28632-28646, 2022, doi: https://doi.org/10.1364/OE.461876.

[26] M. R. Watts, J. Sun, C. DeRose, D. C. Trotter, R. W. Young, G. N. Nielson, "Adiabatic thermo-optic Mach–Zehnder switch," Optics Letters, vol. 38, no. 5, pp. 733–735, 2013, doi: https://doi.org/10.1364/OL.38.000733.

[27] Z. Gong, F. Yang, L. Wang, R. Chen, J. Wu, C. P. Grigoropoulos, J. Yao, "Phase change materials in photonic devices," Journal of Applied Physics, vol. 129, no. 3, 2021, doi: https://doi.org/10.1063/5.0027868.

[28] C. G. Roeloffzen, M. Hoekman, E. J. Klein, L. S. Wevers, R. B. Timens, D. Marchenko, D. Geskus, R. Dekker, A. Alippi, R. Grootjans, A. van Rees, R. M. Oldenbeuving, J.P. Epping, R. G. Heideman, K. Worhoff, A. Leinse, D. Geuzebroek, E. Schreuder, P. W. L. van Dijk, I. Visscher, C. Taddei, Y. Fan, C. Taballione, Y. Liu, D. Marpaung, L. Zhuang, M. Benelajla, K.-J. Boller, "Low-loss Si3N4 TriPleX optical waveguides: Technology and applications overview," *IEEE journal of selected topics in quantum electronics*, vol. 24, no. 4, pp. 1-21, 2018, doi: https://doi.org/10.1109/JSTQE.2018.2793945

[29] R. Soref, J. Hendrickson, H. Liang, A. Majumdar, J. Mu, X. Li, W. P. Huang, "Electro-optical switching at 1550 nm using a two-state GeSe phase-change layer," *Optics Express*, vol. 23, no. 2, pp. 1536-1546, 2015, doi: https://doi.org/10.1364/OE.23.001536.

[30] Y. Zhang, Y. Wu, X. Zhang, H. Li, P. Yuan, "Series-coupled fiber double-ring in Mach–Zehnder interferometer for temperature sensing," *Infrared Sensors, Devices, and Applications*, SPIE, San Diego, California, vol. 96090I, pp. 73–81, 2015, doi: https://doi.org/10.1117/12.2187175.

[31] J. Zheng, A. Khanolkar, P. Xu, S. Colburn, S. Deshmukh, J. Myers, J. Frantz, E. Pop, J. Hendrickson, J. Doylend, N. Boechler, A. Majumdar, "GST-on-silicon hybrid nanophotonic integrated circuits: a non-volatile quasi-continuously reprogrammable platform," *Optical Materials Express*, vol. 8, no. 6, pp. 1551-1561, 2018, doi: https://doi.org/10.1364/OME.8.001551.

[32] L. Bliek, S. Wahls, I. Visscher, C. Taddei, R.B. Timens, R. Oldenbeuving, C. Roeloffzen, M. Verhaegen, "Automatic Delay Tuning of a Novel Ring Resonator-Based Photonic Beamformer for a Transmit Phased Array Antenna," *Journal of Lightwave Technology*, vol. 37, no. 19, pp. 4976–4984 2019, doi: https://doi.org/10.1109/JLT.2019.2926621.

[33] C. G. H. Roeloffzen, M. Hoekman, E. J. Klein, L. S. Wevers, R. Bernardus Timens, D. Marchenko, D. Geskus, R. Dekker, A. Alippi, R. Grootjans, A. van Rees , R. M. Oldenbeuving, J. P. Epping, Rene, G. Heideman, K. Worhoff, A. Leinse, D. Geuzebroek, E. Schreuder, P. W. L. van Dijk, I. Visscher, C. Taddei, Y. Fan, C. Taballione, Y. Liu, D. Marpaung, L. Zhuang, M. Benelajla, K.-J. Boller "Low-loss Si_3N_4 TriPleX optical waveguides: Technology and applications overview," *IEEE Journal of Selected Topics in Quantum Electronics*, vol. 24, no. 4, pp. 1–21, 2018, doi: 10.1109/JSTQE.2018.2793945

[34] Y. Zhang, C. Fowler, J. Liang, B. Azhar, M. Y. Shalaginov, S. Deckoff-Jones, S. An, J.B. Chou, C. M. Roberts, V. Liberman, M. Kang, C. Ríos, K. A. Richardson, C. Rivero-Baleine, T. Gu, H. Zhang, J. Hu, "Electrically reconfigurable non-volatile metasurface using low-loss optical phase-change material," *Nature Nanotechnology*, vol. 16, no. 6, pp. 661-666, 2021, doi: https://doi.org/10.1038/s41565-021-00881-9.

Chapter 3

Photonic Beamforming for next generation satellites

3.1 Introduction

Beamforming refers to a signal processing technique that concentrates the emitted energy from a transmitter into a specific direction, thereby generating a narrow, high-gain beam. This focused radiation pattern is particularly effective in counteracting issues such as propagation losses, signal fading, and multipath interference.

To enable dynamic control over the beam direction, reconfigurable antenna architectures are employed. These systems, known as beam steering antennas, allow the orientation of the radiated beam to be manipulated without mechanical movement. As a result, beam steering antennas have become a rapidly advancing research domain in the field of antennas and wave propagation, gaining widespread interest not only for next-generation mobile communications, but also in mission-critical domains including aerospace platforms, satellite-based systems, and military defense technologies. The growing demand for high-speed beam steering in satellite systems for both communication and Earth observation is increasingly driven by the need for high-data-rate transmission and the development of advanced systems based on radar and laser technologies. This trend reflects not only technological progress in spacecraft platforms but also the evolution of mission requirements that now emphasize agility, data throughput, and adaptability.

Historically, space-based communications and Earth observation have relied predominantly on geostationary (GEO) satellites. These platforms offer extensive coverage but are typically associated with large, expensive, and inflexible systems that involve long development cycles. Thanks to satellite miniaturization, reusable launchers, and mass-production techniques,

Low-Earth-Orbit (LEO) constellations are now displacing traditional GEO solutions. These constellations are now being deployed for both communication and EO applications, offering improved scalability and performance.

LEO satellites, operating at significantly lower altitudes, inherently provide reduced latency (on the order of a few milliseconds) and enhanced data throughput. These characteristics make them highly suitable for real-time and high-bandwidth applications in telecommunications. As a result, the satellite communication market is undergoing rapid expansion, particularly in mobile-centric sectors such as in-flight connectivity, satellite internet for maritime transportation, and communication on-the-move. Furthermore, LEO constellations are playing a key role in bridging digital divides by enabling high-speed internet access in remote and underserved areas. The accelerating deployment of LEO networks is underscored by forecasts projecting over 180% growth, with commercial systems such as SpaceX's Starlink already operational and offering global broadband access that competes with traditional terrestrial networks [1].

In parallel, LEO constellations have transformed the field of remote sensing. Operating at low altitudes has not only enhanced spatial resolution but also significantly increased revisit frequency compared to GEO satellites. Furthermore, relocating remote sensing platforms to LEO has facilitated the use of Synthetic Aperture Radar (SAR), which was previously impractical at GEO due to prohibitive antenna sizes and power demands. Modern SAR constellations, such as those operated by Iceye and Capella Space, now provide persistent, all-weather, day-and-night imaging capabilities. A deeper understanding of conventional SAR systems is provided in Appendix E.

Despite their clear advantages, LEO constellations pose considerable technical and financial challenges. The large number of satellites required for continuous global coverage introduces complexity in terms of both satellite hardware and ground infrastructure. Unlike GEO satellites that maintain a fixed position relative to Earth, LEO satellites move rapidly across the sky, necessitating high-speed, continuously tracking antennas capable of seamless beam switching within milliseconds. This is particularly critical for ensuring uninterrupted communication links and accurate data acquisition.

Beam steering plays a fundamental role in the performance of modern SAR systems. It directly affects imaging capabilities and overall system efficiency. For instance, SAR platforms such as NovaSAR-1 and multi-satellite systems like Cosmo-SkyMed and SAOCOM leverage a beam steering angle of ±30° to enhance imaging flexibility and adaptability to various observational scenarios [2–5]. However, conventional spaceborne SAR systems face challenges related to measurement consistency across different ranges. Variations in signal backscattering and attenuation between near and far ranges result in uneven image quality. Optimizing beam steering angles can mitigate these issues by improving far-range performance and enabling multi-perspective imaging, thus enhancing overall scene quality [6].

Nonetheless, beam steering at space-to-Earth distances involves extreme path losses that demand high RF transmission power. This often exceeds what is feasible for satellite power systems. For example, the Cosmo-SkyMed

constellation requires 17.3 kW for one imaging mode, while its solar panels provide only approximately 4 kW, necessitating a 136 kg battery to bridge the gap [3]. Therefore, developing beam steering networks that offer both high-speed operation and low power consumption is critical.

3.2 Existing beamforming technologies

The first attempts to steer the beam toward a different location were carried out thought mechanical platforms. However, these mechanically steerable antennas, like the motorized tracking antennas used in O3b MEO systems, are inadequate due to slow response times and wear limitations that make them incompatible with the fast-switching requirements of modern beam steering.
Mechanical solutions have been explored—as a reflectarray system driven by a stepper motor achieved ±60° beam steering—but scanning speed limitations introduced latency that undermines real-time performance [7]. Consequently, the focus has shifted toward electronically steerable antennas, which steer beams dynamically without any moving part. This technology has been widely adopted in both space- and ground-based segments of LEO constellations such as Starlink and OneWeb. However, electronic beam steering systems face stringent performance requirements, including high gain (>30 dB), elevation scanning capabilities of ±30°, cross-polarization rejection below –30 dB to enable polarization reuse, and overall efficiency between 70–90% in the Ka-band [8].
Electronically steerable antennas generally rely on phased array antennas (PAAs), which consist of an N×M matrix of radiating elements each connected to individual transceivers. Beam steering is achieved by manipulating the phase of signals at each element [9]. More advanced configurations also support beamforming, where both phase and amplitude are tuned to improve signal quality. However, these systems impose substantial computational loads, which may exceed the limited onboard processing capacity of LEO satellites. Additionally, PAAs require complex phase shifters and costly solid-state components. To address these constraints, research has focused on optimizing the design of individual radiating elements to reduce system complexity without compromising performance. Microstrip patch antennas (MPAs) are the most widely used radiating elements in PAAs due to their compact size, affordability, and straightforward fabrication. Nevertheless, MPAs do not inherently support beam steering and require external tuning or structural modifications to achieve directional control. Several techniques have been explored to enable beam steering with MPAs. One of such methods achieved ±25° steering by partially covering the antenna with a high-index substrate, although this approach reduced directivity and increased bulkiness [10]. A more sophisticated approach employed a six-element circular array with time-modulated reactive loading optimized using a genetic algorithm, achieving beam steering at the cost of increased return loss [11]. Other studies have sought to integrate phase-shifting mechanisms directly into the antenna system.
For example, the design proposed in [12] incorporates low-cost digital phase shifters within the antenna panel itself, achieving a resonant frequency of 2.4

GHz and a steering range of ±60°. This integration reduces cabling complexity by replacing separate phase shifter boards and coaxial RF feeds with a simplified arrangement of RF cables and control lines. However, performance degrades with steering angle widening, with increased main lobe broadening, higher sidelobe levels, reduced gain, and the appearance of grating lobes.

To overcome the inherent limitations of electronic beam steering, research has increasingly turned toward photonic solutions. Various optical beam steering techniques have been proposed, including emitter arrays, fiber-optic phased arrays, photonic crystal waveguides integrated with diffraction gratings, liquid-crystal (LC) phased arrays, and MEMS-based mirror or grating systems [13].

LC-phased arrays are among the most mature options, offering electrically tunable refractive indices that allow them to function as programmable lens. Although these devices feature wide fields of view and low operating voltages, their response times are limited to milliseconds. MEMS-based solutions suffer from similar limitations, including mechanical fragility and the emergence of grating lobes in the far field [14, 15].

More recently, integrated photonic beam steering technologies, particularly optical phased arrays (OPAs), have demonstrated enhanced mechanical robustness and reliability of systems. This solution is well-suited for free-space communication, imaging, and LiDAR applications [16].

A reconfigurable dielectric metasurface demonstrates 11° steering with over 35% efficiency [17], while silicon-based OPAs have demonstrated two-dimensional steering ranges from 3°×17.6° to 46°×10.2°, with improved beam resolution [18, 19]. However, many of these OPAs rely on thermo-optic (TO) tuning, which introduces challenges such as limited field of view, thermal management issues, and high-power consumption [20].

The main pros and cons of the aforementioned technologies are schematized in Figure 3.2.1.

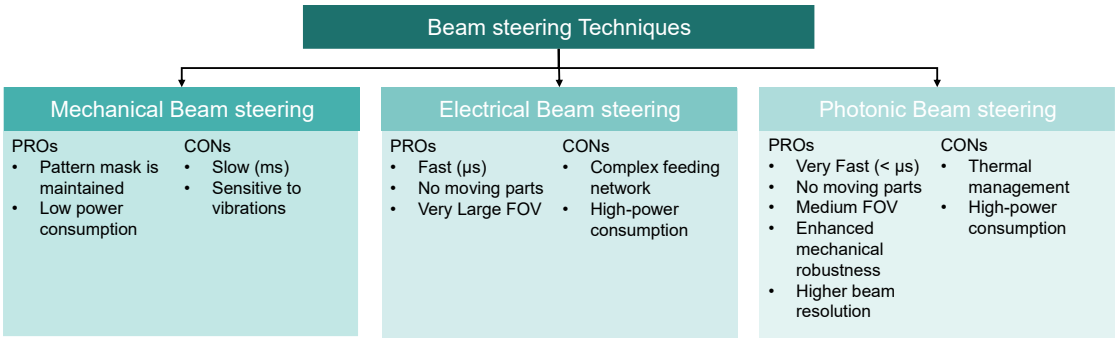

Figure 3.2.1 Beam steering techniques advantages and drawbacks

3.3 Innovative Photonic Beamforming Networks for space satellites

Within the NewSpace framework—where efficiency, scalability, and low power consumption are paramount—the development of alternative OBFN solutions is crucial to meet the stringent demands of next-generation satellite payloads. This research effort encompasses a comparative analysis of diverse tuning strategies and integration technologies, aimed at enhancing reconfigurability, minimizing system footprint, and enabling seamless scalability.

Beyond low power operation, two additional performance criteria are fundamental for an efficient OBFN, the capability for continuous delay tuning, which ensures fine-resolution beam steering across a wide angular range (up to ±60°), and precise bandwidth control, spanning several gigahertz to support wideband operation in the Ku- and Ka-bands [21]. These features are critical for achieving flexible beam steering, efficient spectrum management, and interference mitigation, while simultaneously addressing the growing demand for high-capacity communication services. The following discussion provides a critical assessment of each proposed OBFN solution, underlining their specific advantages, inherent limitations, and innovative contributions to the advancement of photonic beamforming for space applications.

3.3.1 OBFN based on cascaded coupled-resonator optical waveguides (CROWs)

A key element in OBFNs is the optical true time delay line (TTDL), typically implemented as a parallel array to control both the relative delays among antenna elements and the system's operating bandwidth. The two most common TTDL implementations are optical switchable delay lines (OSDLs) and ring resonator (RR)-based delay lines. OSDLs provide large bandwidth (~20 GHz) [22], low in-band ripples (~1 ps) [23], and a simplified architecture with reduced sensitivity to fabrication errors. However, their resolution is inherently limited by the discrete delays produced by the switching mechanism [22, 24]. RR-based delay lines offer continuous delay tuning and have been investigated for over two decades in off-resonance and at-resonance modes. Off-resonance designs provide broad bandwidth (~8 GHz) and low in-band ripples (~2 ps) but yield only short delays (20–40 ps), with cascading extending range at the expense of scalability [25]. At-resonance designs achieve much longer delays (>100 ps) within a compact footprint but are limited by the delay–bandwidth trade-off. Single rings exhibit a bell-shaped delay spectrum, and cascaded configurations can flatten the response and widen bandwidth but introduce significant ripples (~8 ps) and reduce flexibility [26]. Overcoming this trade-off to realize flat-top delay spectra with minimal ripples in compact at-resonance designs would enable squint-free beam steering, flexible bandwidth operation, improved spectral efficiency, and reduced interference in OBFNs.

High-performance TTDLs also require low propagation losses, low power consumption, and fast response. Si_3N_4 platform mitigates combines low loss with compact bends (~100 μm) [27], yet its small thermo-optic coefficient (2.4×10^{-5}/°C) and absence of free-carrier effects hinder power-efficient tuning. Low-loss phase change materials (PCMs) present a promising alternative, offering large refractive index changes via reversible amorphous–crystalline transitions, enabling reconfigurability and multi-level operation through partial phase tuning. While PCMs have been implemented in various active photonic devices [28, 29], their integration into TTDLs remains largely unexplored.

In this work, a novel reconfigurable TTDL with adjustable bandwidth and continuous delay tuning is proposed. Furthermore, an ultra-low power consumption is guaranteed by integrating the SiN platform with the low-loss PCM GeSe. The device comprises two cascaded coupled-resonator optical waveguides (CROWs), each in an all-pass configuration with only two racetrack ring resonators (RTRRs). As variable couplers, compact two- and three-waveguide directional couplers (DCs) with PCM layers on top are employed, instead of the larger Mach–Zehnder interferometer (MZI) couplers commonly used. The localized tuning enabled by the PCM allows independent control of the coupling coefficient and the round-trip phase in the rings, effectively breaking the delay–bandwidth limitation.

Figure 3.3.1 shows the top view of the proposed TTDL, which is composed of two cascaded CROWs. Each CROW operates in an all-pass configuration and incorporates two identical RTRRs, with the outer and inner resonators labeled as RTRR1 and RTRR2, respectively. In each CROW, coupling is implemented through a two-waveguide directional coupler (2WG-DC) and a three-waveguide directional coupler (3WG-DC), which are highlighted with dashed boxes in CROW2.

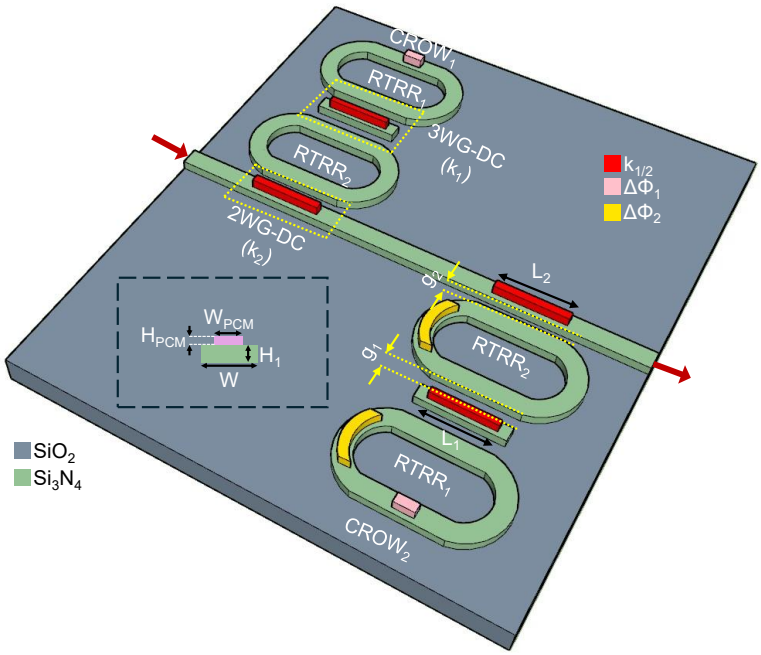

Figure 3.3.1 Schematic diagram of the proposed TTDL. The PCM tuners (GeSe) are denoted with three different colors to distinguish the couplers and two-phase shifters. The inset shows the cross-sectional view of the SiN waveguide with PCM on top.

The cross-section of the optical platform, based on silicon nitride is depicted in the inset of Figure 3.3.1.

Reconfigurability is achieved by integrating low-loss GeSe on top of the SiN waveguide. GeSe exhibits a refractive index contrast between its amorphous ($n_{PCM,a}$ = 2.4) and crystalline ($n_{PCM,c}$= 2.97) states, while maintaining extremely low optical losses in both phases due to its small extinction coefficient (6 × 10^{-6} a.u.) at 1550 nm [30].

The large optical contrast (Δn = 0.57) upon phase change of GeSe implies the possibility of increasing the number of PCM metastable states of partial crystallization by controlling the electrical pulses, this way allowing to widen the device tuning range. In each CROW, light couples from the bus waveguide into RTRR2 via the 2WG-DC, with GeSe deposited on top of the bus waveguide. The 3WG-DC is used to couple light between RTRR1 and RTRR2, with the GeSe layer positioned on the middle waveguide. In both couplers, the refractive index of the GeSe is modulated by electrical pulses to control the coupling strength in the RTRRs, thereby tuning the delay amplitude.

Additionally, the TTDL integrates GeSe-based phase shifters. Particularly, $\Delta\phi_1$ is placed on RTRR2 of CROW1 and CROW2, while $\Delta\phi_2$ is positioned on both RTRRs of CROW2. The proposed structure is modeled and optimized using the transfer matrix method (TMM), with its transmission coefficient described by [31]

$$T = T_{crow1} \cdot T_{crow2}, \qquad T_{crow1/2} = \frac{k_2 - \alpha_2 T_1 e^{i\phi_2}}{1 - k_2 \alpha_2 T_1 e^{i\phi_2}}, \qquad T_1 = \frac{k_1 - \xi \alpha_1 e^{i\phi_1}}{1 - k_1 \alpha_1 e^{i\phi_1}} \tag{5}$$

In the above equations, κ_1 and κ_2 denote the self-coupling coefficients of the two RTRRs in each CROW, as illustrated in Figure 3.3.1, while α_1 and α_2 represent their respective loss coefficients (see Appendix C for further explanations). The loss is assumed to be 0.5 dB/cm, which is five times higher than the nominal SiN waveguide loss, adopted here as a conservative estimation to account for potential additional losses arising from fabrication imperfections and other practical factors [28]. The parameter ξ represents the fraction of power coupled into the middle waveguide of the 3WG-DC, determined by the power conservation relationship $|\kappa'|^2 + |t_1|^2 = 1 - |C_1|^2 = \xi$, where t_1 and κ' are the cross- and self-coupling coefficients, respectively, and C_1 is the coupling coefficient to the middle waveguide [32].

For CROW1, the round-trip phase of RTRR1 is $\phi_1 = \phi$, while RTRR2 has $\phi_2 = \phi + \Delta\phi_1$ due to the presence of a phase shifter. In CROW2, both RTRRs incorporate phase shifters, with $\phi_1 = \phi + \Delta\phi_1 + \Delta\phi_2$ for RTRR1 and $\phi_2 = \phi + \Delta\phi_2$ for RTRR2. The maximum achievable phase shift in each phase shifter is limited by the refractive index contrast between the amorphous and crystalline states of the PCM. Consequently, the phase shifter lengths are designed to deliver the required maximum phase shift for obtaining the desired delay spectrum, as discussed later. In the above expressions, ϕ represents the round-trip phase without any phase shifter, which is related to the modal effective index (n_{eff}) as $\phi = (2\pi\, n_{eff}\, L_r)/\lambda$, where L_r denotes the RTRR perimeter. The smallest reported bending radius for SiN waveguides is approximately 100 μm, with bending losses below 0.01 dB/cm, achievable only with tight fabrication tolerances [27]. In this work, a slightly larger bending radius of 350 μm is adopted in the theoretical analysis to ease fabrication

constraints while maintaining negligible bending loss. Modal analysis of the proposed structure is performed using the full-vectorial FEM-based solver in COMSOL Multiphysics, with the cross-section shown in the inset of Figure 3.3.1. Details on FEM and COMSOL are available in Appendix A. The waveguide parameters are set to $W = 2.8$ μm, $H = 100$ nm, while the GeSe PCM layer is designed with a width $W_{PCM} = 500$ nm and a thickness $H_{PCM} = 10$ nm [33].

The design of the 2WG-DC and 3WG-DC is carried out using coupled mode theory (CMT), as reported in Appendix D, also considering Sellmeier relation to take into account the material wavelength dependency, with the modal profiles and coupling coefficients obtained from FEM simulations. For the 2WG-DC, the objective is to achieve complete power transfer to the cross-port (RTRR2) in the amorphous state of GeSe and to the bar-port (bus waveguide) in the crystalline state.

The inclusion of GeSe on the bus waveguide renders the coupler asymmetric. Under the amorphous state, the phase-matching width of the bus waveguide is calculated to be 1.01 μm. The gap between the bus waveguide and RTRR2 is then varied to determine the optimal coupling length. Figure 3.3.2(a) shows the 2WG-DC response in both GeSe states by varying the coupling length and gap. The coupler length is chosen such that it corresponds to one coupling length in the amorphous state and twice the coupling length in the crystalline state, ensuring complete power transfer to RTRR2 in the amorphous state and to the bus waveguide in the crystalline state. This yields optimal parameters of $L_2 = 350$ μm and $g_2 = 1.2$ μm. The coupled power to RTRR2 can be continuously tuned by controlling the GeSe refractive index via partial crystallization [34].

For the 3WG-DC, it is important to note that the power coupled to the middle waveguide does not contribute to the excitation of any RTRR. Therefore, the coupler length is optimized to minimize this coupling. The power coupled to each port is computed as a function of coupler length for various GeSe refractive indices using FEM and CMT. Figure 3.3.2(b) shows the 3WG-DC response in both GeSe states by varying the coupling length and gap.

For a coupler gap $g_1 = 800$ nm, the optimal length L_1 is found to be approximately 280 μm. At this length, the coupled powers to the middle waveguide ($|C_1|^2$) remains negligible over the entire n_{PCM} range, while the coupled power at the cross-port ($|t_1|^2$) and bar-port ($|\kappa_1|^2$) alternate, similar to the 2WG-DC case. Consequently, at $L_1 = 280$ μm, the 3WG-DC effectively behaves as a 2WG-DC.

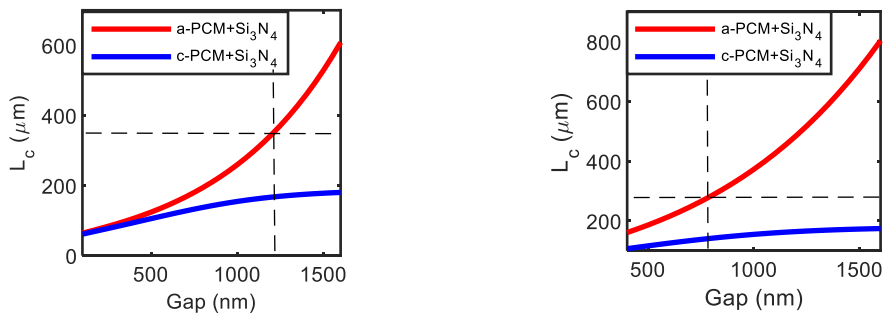

Figure 3.3.2 Coupling length as a function of gap between the waveguides for (a) two waveguide directional coupler and (b) three waveguide directional coupler [35]

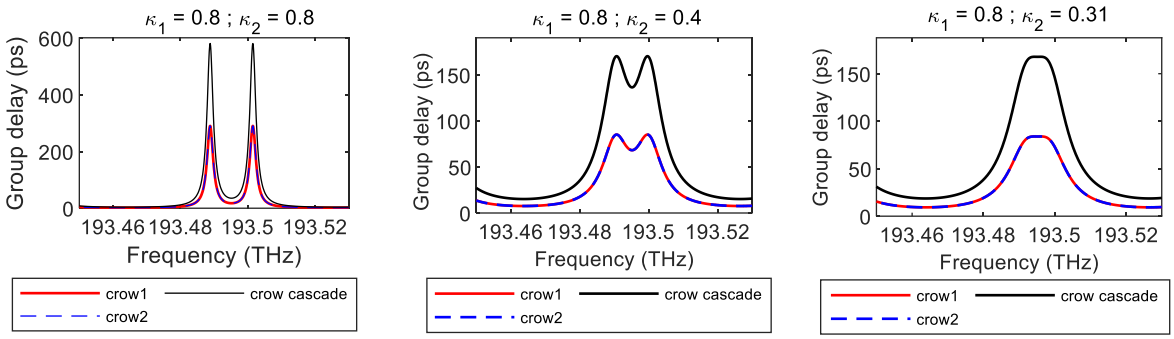

Figure 3.3.3 The group delay spectra for different values of self-coupling coefficient k_2 fixing k_1 = 0.8. (a) k_2 = 0.8 (b) k_2 = 0.4 (c) k_2 = 0.31 [35]

Since the RTRRs operate at resonance, the self-coupling coefficients are carefully optimized. Figure 3.3.3 shows the group delay spectrum for three different combinations of self-coupling coefficients, where the group delay τ is obtained deriving the phase response transfer function respect to the frequency (ω). Ripple amplitudes are found to be maximum for specific coupling coefficients in each CROW configuration and decrease as κ_2 is reduced for a fixed κ_1. For the optimal coupling coefficients, the flat-top group delay spectrum exhibits in-band ripples of approximately 1 ps.

In this approach, coupling coefficients and phase shifts are tuned independently, that would be challenging for metallic heaters due to significant thermal crosstalk. In contrast, localized refractive index changes in GeSe enable independent control of these parameters. Here, the coupling coefficient modifies the group delay response, while the phase shifter maintains a fixed resonance wavelength. Careful adjustment of both coupling coefficients produces a ripple-free flat-top delay profile, as represented in Figure 3.3.3. A 20 μm-long phase shifter is sufficient to induce a π phase shift, reducing of an order of magnitude the length compared to conventional metallic heaters.

The partial crystallization technique applied to the GeSe enables continuous tuning of both the coupling coefficient and the phase. Partial crystallization can be fulfilled by controlling the time duration above the crystallization temperature which can be accomplished either by controlling the pulse duration or pulse voltage [36]. Therefore, for a given length, the maximum phase shift is limited by the refractive index change due to the complete crystallization of GeSe. Continuous delay tuning at fixed bandwidth (and vice versa) is achieved by varying the coupling coefficient in conjunction with phase compensation, implemented using PCM-based phase shifters integrated into the racetrack RTRRs.

The resulting group delay spectra are presented in Figure 3.3.4, where the (a) illustrates delay tuning at a fixed signal bandwidth of 5 GHz, while the (b) shows bandwidth tuning for a fixed delay of 140 ps.

The results demonstrate that the delay can be varied over a range exceeding 100 ps while maintaining a constant 5 GHz bandwidth, and conversely, the bandwidth can be tuned from 4.3 GHz to 7 GHz while keeping the delay fixed.

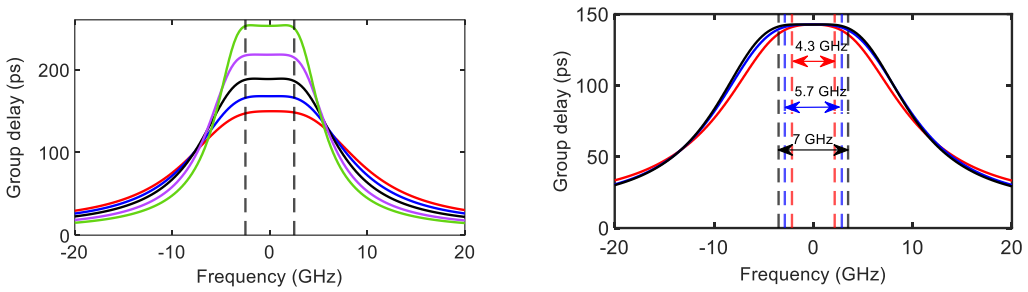

(a) (b)

Figure 3.3.4 (a) Group delay spectrum tuning it while the bandwidth is preserved at 5 GHz. (b) Group delay spectrum tuning the signal bandwidth from 4.3 GHz to 7 GHz for a fixed delay of 140 ps [35]

This represents a significant advance, as it clearly illustrates the possibility of overcoming the conventional constraint imposed by the delay–bandwidth product. The proposed architecture employs two cascaded coupled-resonator optical waveguides (CROWs), each comprising two silicon nitride racetrack resonators, which together form the fundamental delay unit, thereby ensuring compactness and efficiency. Continuous tuning of the coupling coefficient and phase is achieved through the integration of a low-loss phase-change material (GeSe). Once introduced in an optical beamforming network (OBFN), as the one sketched in Figure 3.3.5, this architecture enables simultaneous control of both signal bandwidth and continuous delay tuning [35]. In this configuration, the laser source serves as the optical carrier, which is modulated by the RF signal and subsequently filtered by a single-sideband filter (SSBF). The resulting signal is then directed to the key element of the OBFN system, the true time delay lines (TTDLs), which are composed of the basic delay unit (BDU) and a power splitter responsible for generating and controlling the relative delays in the microwave signal. The delayed optical signals are converted back into the RF domain through an array of photodiodes (PDs), after which they are delivered to the radiation stage of the system, namely the phased array antennas (PAAs).

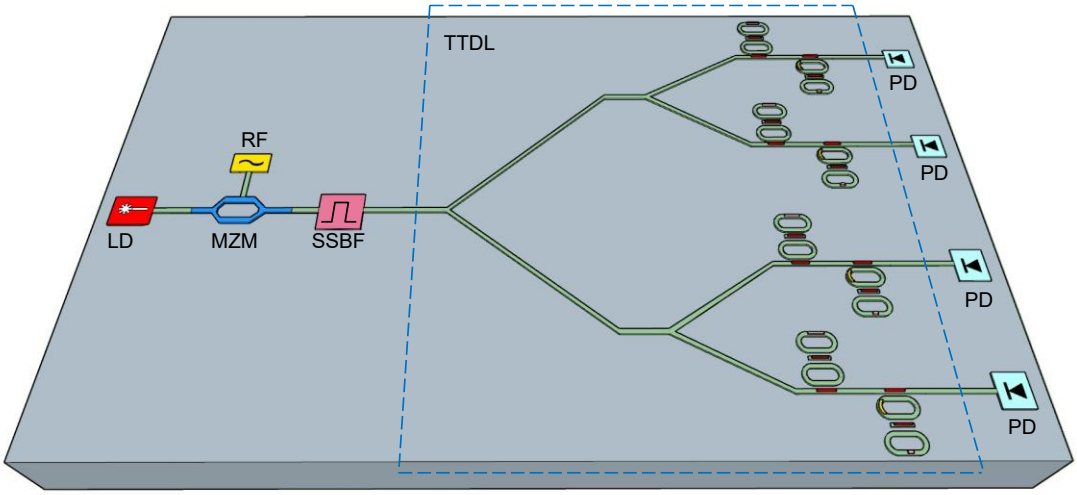

Figure 3.3.5 The schematic of the 1×4 OBFN having basic delay unit (BDU) formed with two cascaded CROW architecture. (LD: laser diode; MZM: Mach Zehnder Modulator; SSBF: Single Sideband Filter; TTDL: True Time Delay Line; PD: Photodetector)

Concerning the performance of the PCM tuners, electrical pulses are applied to the ITO electrode to modulate the refractive index of the GeSe phase-change material. Complete crystallization of GeSe requires maintaining the material above its crystallization temperature of 275 °C for a duration of approximately 100 ns, while partial crystallization can be achieved by carefully controlling either the pulse width or the applied voltage. The estimated total peak power consumption to drive the TTDL amounts to 6.34 mW, which is nearly two orders of magnitude lower than the 881.3 mW required by conventional metallic heaters. Moreover, the reconfiguration times are significantly improved, with rise and fall times of 1.39 μs and 5.9 μs, respectively, compared to values on the order of 100 μs typically observed for metallic heaters on SiN platforms [37].
Unlike traditional MZI-based couplers, the proposed scheme employs two- and three-waveguide directional couplers integrated with a low-loss phase-change material. The localized tuning effect of the PCM ensures compactness while enabling continuous time-delay adjustment. Phase shifters based on PCM are strategically positioned to control the optical phase, effectively breaking the delay–bandwidth trade-off. The design achieves a maximum tunable delay of 140 ps with a total peak power consumption of nearly two orders of magnitude lower than that of conventional metallic heaters. Importantly, the system bandwidth remains stable across variations in the PCM refractive index, making it compatible with partial-crystallization-based tuning techniques. Additionally, the non-volatile nature of the PCM allows the optical beamforming network to maintain the programmed delays without continuous power consumption. The proposed architecture supports bandwidth reconfigurability in the 4.3–7 GHz range with a delay ripple below 1 ps over a steering range of ±60°. These features demonstrate the strong potential of this approach for future wireless communication systems, where it could be employed to drive large phased array antenna (PAA) systems with continuous beam steering capability and dynamically adjustable wideband operation.

3.3.2 Beam steering network based on asymmetric power splitters

A two-dimensional optical phased array (2D OPA) generally comprises $N \times M$ radiating elements, with N elements distributed along the elevation axis and M elements along the azimuth axis. Conventional designs employ N tunable delay lines to dynamically steer the far-field radiation pattern by adjusting the relative phase among the elements, thereby directing the optical beam toward a desired angle (Figure 3.3.6(a)). Achieving a wide steering range requires delay lines with broad tunability, which in turn leads to complex architectures, challenging fabrication processes, and high power demands—factors that run counter to the cost-effectiveness requirements of the NewSpace economy. For SAR systems (see Appendix E) in EO applications, the typical specifications for optical delay lines (ODLs) include large bandwidth (≥ 1 GHz), wide and continuous delay tunability on the order of hundreds of picoseconds, fast reconfigurability, and low power consumption (< 10 W) [38].

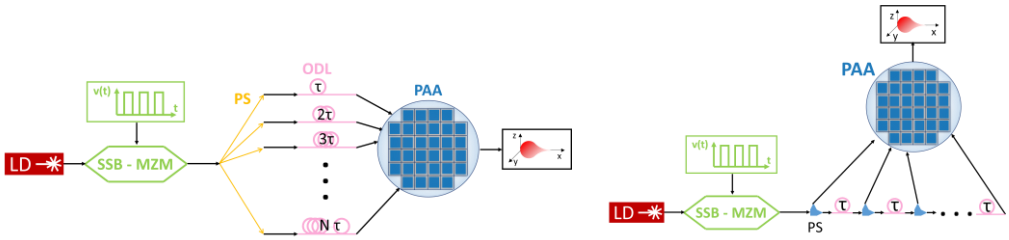

(a) (b)

Figure 3.3.6 (a) Traditional architecture of OBFN (b) Proposed OBFN architecture (LD: laser diode; SSB – MZM: single sideband Mach-Zehnder modulator; PS: phase shifter; ODL: optical delay lines; PAA: phased array antenna).

In this work, a novel beam steering architecture has been introduced, together with an OPA design, that drastically lowers power consumption through the use of innovative asymmetrical power splitters combined with fixed delay lines. As illustrated in Figure 3.3.6(b), each beam-steering branch integrates an identical delay line, connected to the next branch through an asymmetrical power splitter.

The principle underlying this scheme is that the delay difference between consecutive radiating elements must remain constant across all branches, so that each branch experiences the same incremental time delay, thereby enabling accurate radiation pattern steering. Although this configuration requires a larger number of delay lines ($N^2/2$) compared with conventional approaches (N), it simplifies both design and fabrication by eliminating the need for tunable delay lines, while also substantially reducing power consumption.

Within each tile, the beam steering network operates by generating a continuous-wave (CW) optical carrier from a tunable laser diode (LD), which is modulated at the target operating frequency using a single-sideband Mach–Zehnder modulator (SSB-MZM). Before optoelectronic conversion at the photodiodes that drive the antenna elements, the optical signal propagates through the ODLs, ensuring uniform time delays across all branches, and passes through 1×2 power splitters. The reference signal in the first branch reaches the first photodiode without delay, while signals in the subsequent branches are progressively delayed and split, thereby establishing the desired steering angle θ. The design of the PAA and beam steering network is driven by the requirement to achieve a target spatial resolution of 90 cm in both the azimuth and range directions in Stripmap mode.

This high-resolution is particularly valuable for EO applications such as snow and ice monitoring, high-precision altimetry, and oceanography, where capturing fine details and ensuring accuracy are essential. EO satellites carrying SAR payloads support multiple operating modes tailored to diverse scientific and operational objectives. In Stripmap mode, the radar continuously illuminates a narrow ground swath along the satellite's orbit, yielding imagery with high spatial resolution. In contrast, ScanSAR mode expands the coverage by rapidly switching the radar beam across several sub-swaths, thereby enlarging the observed area at the expense of spatial resolution. Spotlight mode achieves the highest resolution by maintaining the radar beam on a specific target for a longer dwell time, effectively extending the synthetic aperture while limiting scene size. In this study, the satellite is assumed to operate in both Stripmap and ScanSAR modes, striking a balance among spatial resolution, coverage, and revisit time—three key optimization drivers in EO missions. Achieving this level of spatial resolution would represent a substantial

improvement over existing state-of-the-art spaceborne SAR systems, which generally provide resolutions of only a few meters—for instance, COSMO-SkyMed (3–15 m), NovaSAR (6 m), and SAOCOM (10 m) in Stripmap mode [3-5].

In conventional monostatic SAR systems, the range resolution (δr) is governed by the transmitted pulse bandwidth (W), whereas the azimuth resolution (δh) depends exclusively on the antenna length (L), as described by the following expressions [39]:

$$\delta r = \frac{c}{2W} \tag{6}$$

$$\delta h = \frac{L}{2} \tag{7}$$

where c denotes the speed of light. In the Ka-band, the maximum available pulse bandwidth, constrained by ITU regulations, is approximately 500 MHz [40], which limits the achievable range resolution to about 30 cm. To attain an azimuth resolution finer than 90 cm, the corresponding pulse repetition frequency (PRF) has been estimated using the above equations to lie between 8.4 and 8.7 kHz. The PRF, defined as the interval between successive radar pulses, is directly related to the satellite's orbital velocity. A Ka-band has been selected to satisfy these requirements, providing benefits such as reduced antenna size and mass, along with the capability to operate satellites in closer proximity for interferometric SAR applications. Moreover, at these frequencies, radar pulses predominantly reflect from the target surface rather than its volume, thereby facilitating the generation of highly accurate digital elevation models.

The main lobe beamwidth along the azimuth direction ($\Delta\Psi_{az}$) has been determined via the Method of Moments (MoM) to be 0.27°, while the elevation beamwidth ($\Delta\Psi_{el}$) has been numerically evaluated as 1.13°, constrained by the maximum allowable PRF. The MoM, which reformulates surface integral equations into a solvable linear system, enables efficient and accurate numerical modelling [41]. With this approach, the designed phased array antenna (PAA) is predicted to provide an azimuth resolution of 89 cm.

In Stripmap mode, where pulses are transmitted at a fixed angle (typically broadside with respect to the flight direction), the swath width (x_a) depends on the satellite altitude (H), the elevation main lobe beamwidth ($\Delta\Psi_{el}$), and the incidence angle (φ), following the relationship

$$x_a = R\,\Delta\psi_{el} = \frac{H}{cos(\varphi)}\Delta\psi_{el} \tag{8}$$

where R is the slant range distance. Assuming a reference incidence angle φ = 30° and a beam steering range θ = ±15°, the calculated swath width amounts to 14.11 km, with variations between –1.16 km and +3.17 km depending on φ.

By applying Eqs. (6)–(8) as reported in [41], the target values for azimuth resolution, range resolution, and swath width have been derived from the orbital design parameters. Once these performance goals for the optical phased array (OPA) are defined, the antenna can be dimensioned in terms of radiating elements (N×M) through the MoM approach to satisfy mission requirements.

For validation, a complementary analysis performed with Ansys Systems Tool Kit (STK) software estimated the theoretical coverage and revisit times of the proposed satellite, assuming ScanSAR mode with three sub-swaths. The results indicate that the system achieves 50% global coverage in roughly 4.5 days, with an average revisit period of 8 days. These relatively modest figures stem from the limited swath width imposed by the stringent high-resolution requirement, suggesting that, in a realistic mission scenario, deployment of multiple satellites would be necessary to ensure improved coverage and shorter revisit times while maintaining the targeted resolution.

The OPA array size has been determined by modelling each radiating element as an isotropic source with an element spacing fixed at half the wavelength ($\lambda/2$ = 4.2 mm) to ensure constructive interference under uniform excitation. The final design comprises 90 × 376 elements, yielding the radiation patterns illustrated in Figure 3.3.7(a) and (b) for elevation and azimuth, respectively. Both beamwidths meet the specified requirements under this configuration. Furthermore, the elevation radiation diagrams shown in Figure 3.3.7(c)–(e) demonstrate the array's capability to steer the beam across the required range of –15° to +15°. To enable this steering, the true-time delay between adjacent elements must match the geometric path difference for ±15°. With an inter-element spacing of $\lambda/2$ = 4.2 mm, the necessary delay is $\Delta\tau = d/c \cdot sin\theta \approx 3.62$ ps.

Parametric simulations, conducted by varying the OPA central frequency, validate both the independence of θ from $\Delta\Psi_{el}$ and the squint-free operation of the beam-steering network.

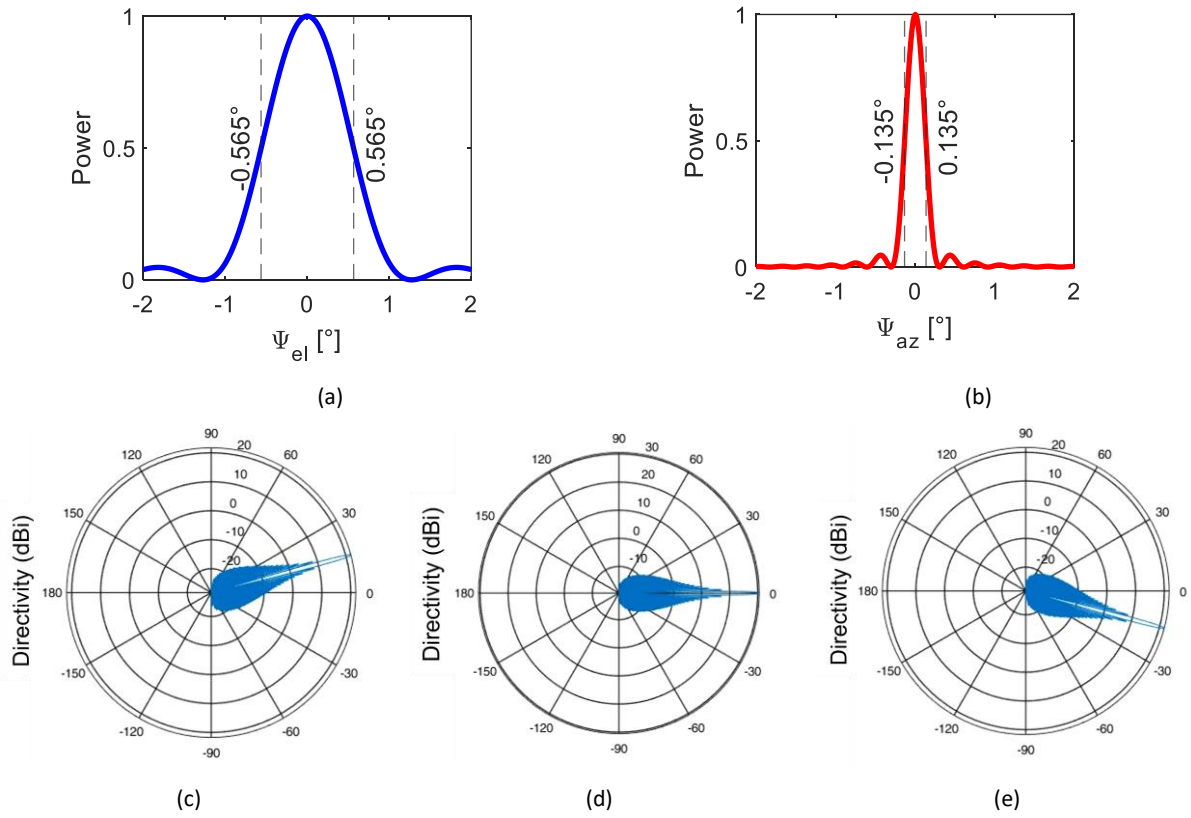

Figure 3.3.7 Radiation patterns along the (a) elevation and (b) azimuth directions. Radiation diagrams along the elevation direction for (c) -15°, (d) 0°, and (e) 15°

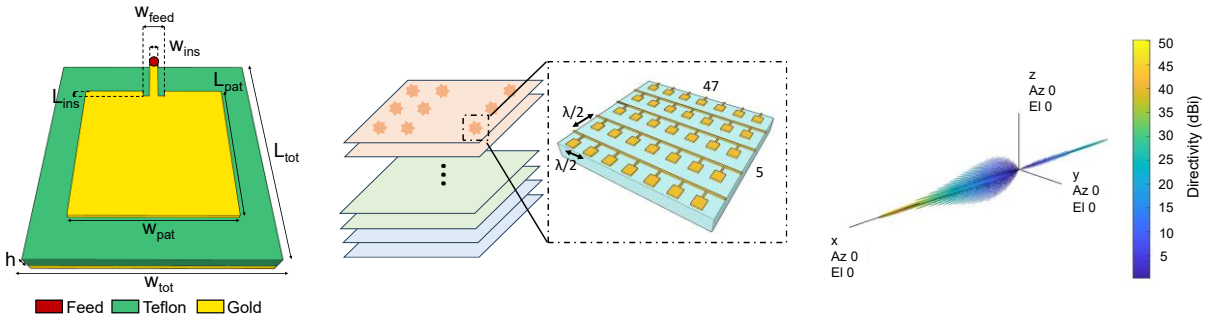

(a) (b) (c)

Figure 3.3.8 (a) Inset-fed microstrip patch antenna sketch; (b) Sketch of the PAA architecture; (c) PAA directivity (h: thickness; w_{tot}: total width; w_{pat}: patch width; w_{ins}: inset width; w_{feed}: feeding width; L_{ins}: inset length; L_{tot}: total length; L_{pat}: patch length)

Beam squint, a typical limitation in analog beam-steering architectures where phase shifts depend on frequency, can severely impact wideband communications. The proposed design successfully overcomes this limitation, delivering consistent performance across the entire operating frequency range.

Once the OPA dimensions were defined, the ideal isotropic element is replaced with a practical antenna. To identify the most suitable configuration for the intended application, several antenna topologies are compared, aiming to minimize footprint while maximizing directivity. The performance of simple configurations, including dipole, triangular bowtie, and rounded bowtie antennas, are rated exploiting the MoM, with the inset-fed microstrip patch antenna (see Figure 3.3.8(a)) emerging as the most effective solution. This antenna consists of a rectangular patch with a 50 Ω microstrip feed line recessed into the patch, fabricated on a 210 µm-thick Teflon substrate. The feed line width is w_{feed} = 240 µm.

To ensure proper operation in Ka-band, at f_0 = 35.75 GHz, the patch dimensions are set to w_{pat} = 3.8 mm and L_{pat} = 3.8 mm, while the inset dimensions are w_{ins} = 90 µm and L_{ins} = 559 µm. The ground plane dimensions are w_{tot} = L_{tot} = 8.4 mm. These values were derived following standard antenna theory equations [42]. The resulting OPA, illustrated in Figure 3.3.8(b), is composed of four identical panels, each containing two columns of 18 tiles arranged in 5×47 grids of antenna elements.

The complete OPA measures 6 m × 1.5 m, achieving a global directivity of 45 dB, as reported in Figure 3.3.8(c). This result is in excellent agreement with theoretical estimates based on antenna theory [39]. Although higher directivity could be achieved by increasing the substrate thickness, modifying the basic radiating elements or array geometry, or by employing alternative materials (e.g., comb structures), the choice is made to retain conventional materials and geometries. This decision significantly reduces manufacturing cost and complexity, aligning with the objectives of the NewSpace Economy.

The proposed beam steering network (Figure 3.3.9) consists of a laser diode (LD), a single-sideband Mach–Zehnder modulator (SSB-MZM), and a cascaded arrangement of asymmetrical 1×2 power splitters (PSs) and optical delay lines (ODLs). Beam steering is realized by tuning the laser wavelength. The RF input signal (RF_{in}) modulates the optical carrier through the SSB-MZM, and the resulting optical output is delivered to the array of 1×2 splitters and ODLs.

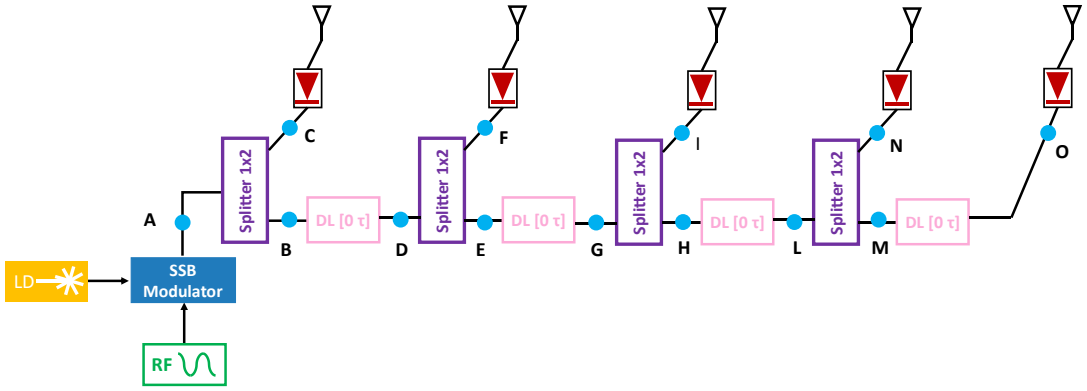

Figure 3.3.9 Proposed architecture (LD: laser diode; SSB: single side band; DL: delay line)

Each splitter is carefully engineered to provide the required splitting ratio between the output power reaching each photodiode and the one directed to the subsequent ODL stage, where a wavelength-dependent time delay Δt is introduced. The array of photodetectors converts the delayed optical signals back into RF signals that drive the antenna elements, thereby enabling beam steering by controlling the angle θ.

To ensure full compatibility with monolithic integration and chip-scale implementation, all components in the network are realized using waveguide-based technologies. Each building block of the system is carefully designed, starting with the SSB modulator, which operates at 35.75 GHz with a 500 MHz bandwidth in compliance with ITU requirements [43]. The SSB modulation scheme is selected over conventional amplitude modulation (AM) due to its superior spectral and power efficiency—key requirements for spaceborne systems.

Unlike AM, which requires twice the bandwidth and wastes power by distributing it across the carrier and both sidebands, SSB transmits only a single sideband, thereby conserving both bandwidth and power. Moreover, AM would demand ODLs capable of introducing identical delays to both sidebands, significantly complicating the architecture.

The implemented SSB modulator follows a Hartley configuration (see Figure 3.3.10), employing two quadrature RF sinusoidal signals that drive a Mach–Zehnder modulator (MZM). This approach effectively suppresses one sideband, enhancing system efficiency for the targeted application. The two sinusoidal signals, oscillating at 35.5 GHz and 36 GHz, are frequency mixed to generate a 35.75 GHz carrier with a 500 MHz bandwidth. The MZM is realized as a ring-assisted interferometric silicon modulator, offering a 3-dB bandwidth of 45 GHz, operation speed up to 200 Gbit/s, and an insertion loss (IL) of 9.5 dB in the C-band [44]. The continuous-wave (CW) laser beam is modulated by this MZM, while suppression of the unwanted sideband is achieved through a rectangular optical filter, consisting of a 5th-order silicon microring resonators, that provides an IL of 1.5 dB and an extinction ratio exceeding 60 dB [42]. Enhanced extinction ratios (ER) have been reported in literature using cascaded Mach–Zehnder interferometers [45] and coupled-ring optical waveguide (CROW) architectures [46, 47], which enable compact footprints and efficient wavelength tunability.

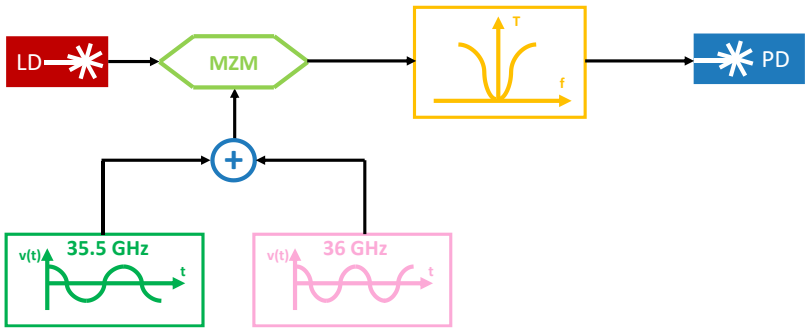

Figure 3.3.10 Single Sideband Modulator (LD: Laser Diode; PD: photodiode; MZM: Mach-Zehnder Modulator)

The modulated optical signal, once filtered, is converted into the electrical domain by means of a p-i-n germanium photodetector integrated within a silicon-on-insulator waveguide, exhibiting a responsivity of about 1 A/W at 1550 nm [48]. System-level simulations are carried out using the commercial software Optisystem, assuming a 5 kHz-linewidth external cavity laser diode with a wide tuning range of 200 nm at 1550 nm and an output power of 50 mW [49]. The temporal signal retrieved from the photodetector, along with its spectrum, is depicted in Figure 3.3.11(a) and (b), showing a sideband suppression ratio (SBSR) exceeding 70 dB and a simulated pulse width of approximately 6 ns. Even with a lower-order filter providing an ER of 40 dB, an SBSR above 50 dB can still be achieved without significantly compromising the operation of the beam steering network. In this case, the unwanted sideband remains sufficiently suppressed to prevent the introduction of spurious components, spectral distortion, and signal-to-noise ratio degradation.
Since the use of conventional 50:50 beam splitters leads to a significant reduction of the optical power reaching the final photodiode in the network, here it has been developed asymmetrical 1×2 beam splitters, ensuring uniform power distribution across all photodiodes.
The optical powers at different points of the i-th stage are denoted as P_i, P_{i+1}, and P_{Ph}, corresponding to the input power of the i-th splitter, the delayed optical power reaching the (i+1)-th splitter, and the power delivered to the i-th photodetector, respectively. For proper operation, each i-th splitter must be designed with a power ratio (PR) between P_{i+1} and P_{Ph} equal to $PR = 1/(N–i+1)$.

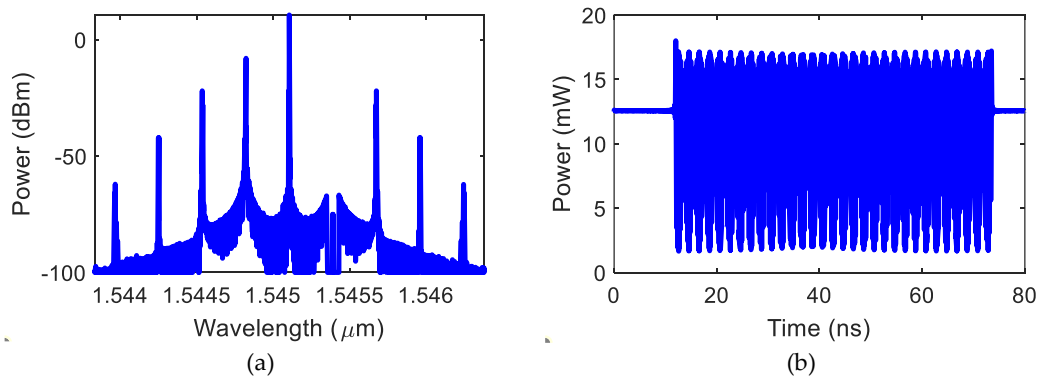

Figure 3.3.11 SSB Modulator output spectrum (point A in Fig. 4) in wavelength (a) and time (b) domain

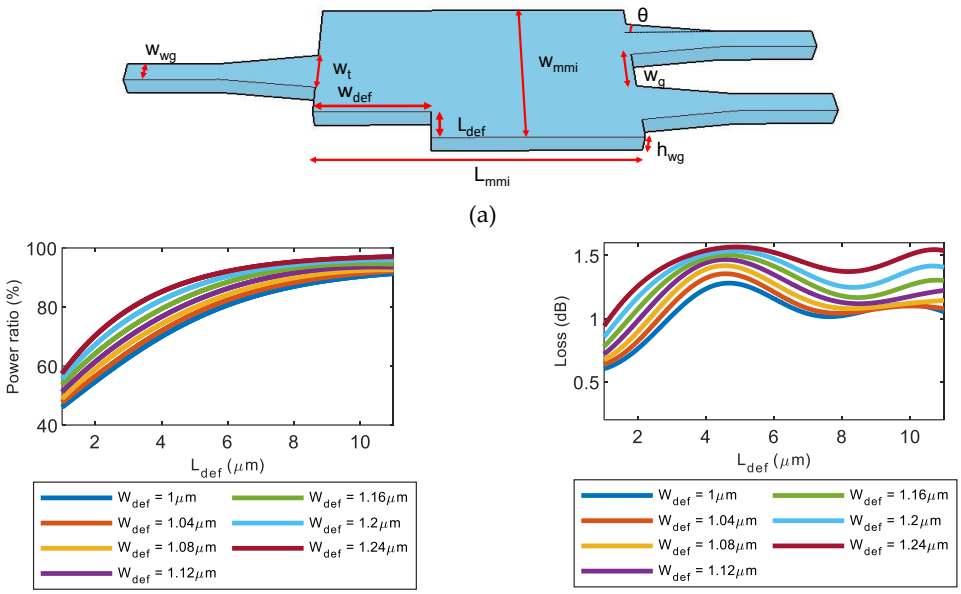

Figure 3.3.12 (a) Sketch of asymmetrical MMI with its design parameters. (b) MMI splitting power ratio (%) vs. defect length (L_{def}) by varying the defect width (w_{def}) (c) MMI Losses (dB) vs. defect length (L_{def}) by varying the defect width (w_{def}) (w_{wg}: waveguide width; w_t: width of taper; w_{mmi}: MMI width; θ: tapering angle; w_g: spacing between output waveguides; L_{mmi}: MMI length; h_{wg}: waveguide thickness; w_{def}: defect width; L_{def}: defect length)

Multimode interferometers (MMIs) allow the realization of such asymmetric *PRs* by tuning the device length, thereby achieving controlled power splitting while maintaining compactness and very low insertion losses.

To further extend the range of obtainable *PRs* without modifying the MMI length, a structural defect in the form of a hole is introduced into the silicon multimode waveguide [50], as illustrated in Figure 3.3.12(a). This defect induces a sharp refractive index discontinuity, thereby altering the interference conditions along the propagation path. By engineering the defect length L_{def} and width w_{def}, a broad set of splitting ratios can be achieved, as shown in Figure 3.3.17(b). However, the abrupt index variation also introduces non-negligible differences in branch losses, as reported in Figure 3.3.17(c). With appropriate design, splitting ratios between 55% and 95% are attainable, with a maximum insertion loss of 1.5 dB.

To precisely determine the geometrical parameters of this innovative asymmetrical power splitter, w_{wg} = 500 nm, h_{wg} = 220 nm, w_g = 0.60 μm, w_t = 1.20 μm, w_{mmi} = 3.60 μm, L_{mmi} = 11.50 μm, and γ = 1° [51], extensive parametric simulations based on the 3D Beam Propagation Method (BPM) were performed. A detailed explanation of this method is provided in Appendix B.

As arises from Figure 3.3.12(b) and (c), standard fabrication tolerances of ±10 nm result in variations of approximately 1% in the power splitting ratio and 0.05 dB in device losses. To assess the effect on the overall system output power, a worst-case simulation was carried out, showing a degradation of about 10% in the optical power at the first photodiode. Nevertheless, this reduction does not introduce any significant impact on the global performance of the system.

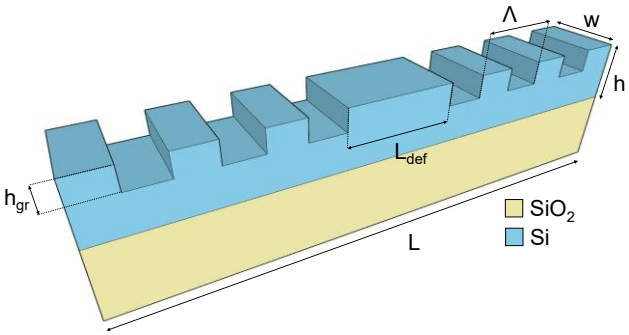

Figure 3.3.13 ODL structure (w: waveguide width; h: waveguide thickness; h_{gr}: grating depth; L_{def}: defect length; L: overall length; Λ: period)

To realize the necessary 3.62 ps delay, corresponding to a beam steering capability of ±15°, a one-dimensional silicon photonic crystal ODL is proposed. The device incorporates a top grating structure fabricated by modulating the thickness of the silicon core and introducing a central defect of length L_{def} within the grating. As illustrated in Figure 3.3.13, the waveguide follows a standard silicon-on-insulator (SOI) geometry, with a height (h) of 220 nm, a width (w) of 500 nm, and an etched grating depth (h_{gr}) of 30 nm.

The defect generates multiple resonant channels within the photonic bandgap of the grating, each characterized by distinct transmission levels [52].

The structural properties of the defect, particularly its length, strongly influence the transmission spectrum of the grating, thereby affecting parameters such as the number of transmission channels, the free spectral range, and the Q-factor. Specifically, L_{def} determines the central wavelength of the ODL according to the relation

$$\lambda_r = L_{def}\, n_{eff}\, \frac{4}{4m + 1} \tag{9}$$

here, m denotes an integer corresponding to the grating order, while the effective refractive index of the grating is given by $n_{eff} = DC \cdot n_{Si} + (1-DC) \cdot n_{air}$. This configuration introduces a phase shift of $\pi/2 + 2m\pi$, which guarantees constructive interference in accordance with antenna array theory. Furthermore, increasing the number of grating periods (N_p) narrows the Full-Width at Half-Maximum (FWHM) of the resonances, thereby enhancing the Q-factor. The electromagnetic behavior of the proposed waveguide is modelled through the transfer matrix method, while mode analysis is carried out using the Finite Element Method (FEM), whose details are reported in Appendix C and Appendix A, respectively. Different values of grating height (h_{gr}), L_{def}, and the overall grating length (L) are investigated to minimize insertion loss (IL) for a target time delay of 3.62 ps. To maintain a central wavelength (λ) of 1550 nm, the grating period (Λ) is fixed at 320 nm.

The variation of the time delay $\Delta\tau$ as a function of m, for h_{gr} of 30 nm and 40 nm, is presented in Figure 3.3.14(a) and (b), respectively. Adjusting m while holding λ and n_{eff} constant modifies L_{def} for different values of N_p. The defect length L_{def} directly impacts the number of resonant channels within the Photonic BandGap (PBG), which may be either even or odd.

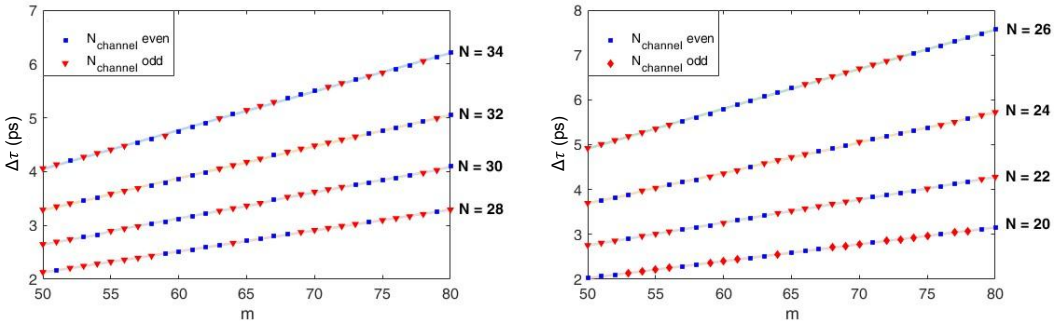

Figure 3.3.14 Delay values ($\Delta\tau$) vs. grating order (m) with different numbers of periods N_p for even and odd channels with a grating etching depth (h_{gr}) of 30 nm(a) and of 40 nm(b).

To enable beam steering in both positive and negative elevation directions, an odd number of channels is required, with the central delay peak serving as the reference. As depicted in Figure 3.3.14(a) and (b), multiple parameter configurations satisfy the required time delay of 3.62 ps. However, to ensure proper beating between the carrier and the signal at the photodiode, both must undergo identical delays. This is achieved by positioning the carrier and signal symmetrically with respect to the delay peak, as illustrated in Figure 3.3.15.

Such symmetric placement results in the signal experiencing a slightly smaller delay than the peak value, necessitating $\Delta\tau$ larger than 3.62 ps. Consequently, the configuration with h_{gr} = 40 nm is selected, as it not only satisfies this requirement but also provides a more compact structure compared to the 30 nm case due to the higher grating strength. Therefore, the final design parameters are m = 70, L_{def} = 45.12 µm, and N_p = 26, thereby ensuring an odd number of resonant channels within the PBG at the central wavelength.

The transmission and time-delay spectra are presented in Figure 3.3.16(a) and (b), respectively. As anticipated, introducing a long defect into the 1D-PhC generates multiple resonant channels within the photonic bandgap, extending from 1470 nm to 1630 nm. The resulting $\Delta\tau$ profile follows a Gaussian-like envelope, with a maximum delay of 7.3 ps and a minimum of 0.7 ps, both in agreement with ITU specifications. According to these standards, the optical delay must remain constant across the entire 500 MHz signal bandwidth. In this case, the delay variation across the bandwidth amounts to only 33 fs, which is negligible and fully compliant with the requirement.

Table 3.3.1 summarizes the insertion loss (IL), time delay (τ), and steering angle (θ) for each device channel.

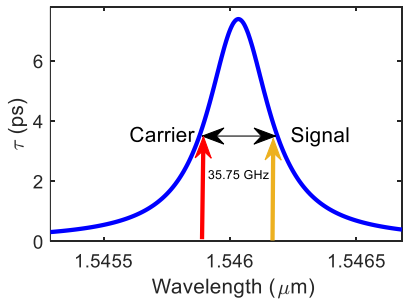

Figure 3.3.15 Time delay peak with Carrier (red arrow) and Signal (yellow arrow) experiencing the same delay.

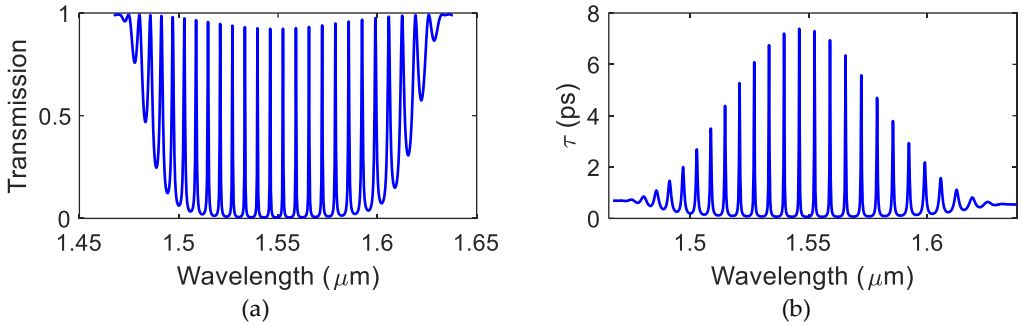

Figure 3.3.16 ODL transmission (a) and delay time (b) spectra.

A steering angle of $\theta = 15.72°$ corresponds to a time delay of 3.79 ps, associated with the maximum IL of 3.26 dB. While the proposed beam steering network does not permit exact broadside steering, it achieves a total steering range of 13.42°. However, due to the discrete nature of the ODL, continuous tuning of τ is not possible. Therefore, to realize steering angles beyond this discrete set, an auxiliary electronic control strategy would be required.

Table 3.3.1 Achievable system steering angles for different time delays

Channel no.	Λ [nm]	τ [ps]	IL [dB]	θ [°]
1	1545.891	3.793458	3.26	15.72
2	1552.350	3.761871	3.25	15.59
3	1558.867	3.724096	3.07	15.43
4	1565.439	3.661566	2.73	15.16
5	1572.061	3.542919	2.28	14.66
6	1578.719	3.251268	1.88	13.43
7	1585.426	2.999543	1.26	12.37
8	1592.148	2.534981	0.85	10.43
9	1598.874	2.004758	0.55	8.23
10	1605.585	1.502538	0.36	6.16
11	1612.265	1.097194	0.23	4.50
12	1619.149	0.813468	0.046	3.33
13	1625.134	0.632809	0.026	2.59
14	1631.585	0.562213	0.009	2.30

The behavior of the complete beam steering architecture (see Figure 3.3.9) is simulated using the commercial solver OptiSystem. This platform allows the network to be modelled by cascading the transfer functions of the designed building blocks.

Simulations are carried out for a target steering angle of $\theta = 15°$, which represents the worst-case condition in terms of power demand. At this angle, the output power detected at each hub, $P_{out\text{-}i}$ (with i = 1, …, 13), reaches its minimum value due to the maximum system insertion loss. The calculated $P_{out\text{-}i}$ values are reported in Table

3.3.2, accounting for all losses in the system, including those introduced by the SSB modulator, asymmetric beam splitters, ODL, and photodiodes.
The time-domain signals measured at the first and last photodiodes are shown in Figure 3.3.17(a) and (b). The signal detected at the last photodiode experiences a delay factor of $df = 5$ compared to the first, resulting in a total delay of $\Delta\tau_{tot} = df \cdot \Delta\tau$ = 18.59 ps.

Table 3.3.2 Optical power values of the photodiodes depicted in Figure 3.3.9

	P_{out} [dBm]	P_{out} [mW]		P_{out} [dBm]	P_{out} [mW]
A	10.81	12.04	B	9.11	8.14
C	3.06	2.04	D	8.32	6.78
E	5.86	3.86	F	1.09	1.29
G	5.07	3.21	H	2.42	1.74
I	-0.60	0.87	L	1.62	1.74
M	-1.68	0.68	N	-1.67	0.68
O	-2.47	0.57			

Since $P_{out13} = P_{ph5}$ is approximately 570 µW, the signal must be amplified through a transimpedance amplifier, a lobe-formation amplifier, and a high-power amplifier, providing an overall gain exceeding 60 dB.
The total power consumption of the proposed beam steering network is estimated at ~1 kW, which is substantially lower than the requirements of tunable architectures reported in literature, typically ranging from a few to several tens of kilowatts [3–5]. This corresponds to a drastic reduction in overall SAR system power consumption, thereby easing EPS constraints compared to conventional solutions.
A novel beam steering network architecture, designed to meet the stringent constraints of modern SAR payloads, has been developed and simulated.
This work covers the design of individual building blocks and the evaluation of overall system performance, specifically tailored to meet COSMO-SkyMed requirements while leveraging Ka-band advantages, thus advancing the feasibility of a fully optical SAR system. Additionally, the proposed architecture demonstrates the capability of achieving beam steering without tunable delay lines, thereby reducing fabrication costs, recursive design efforts, and power consumption.

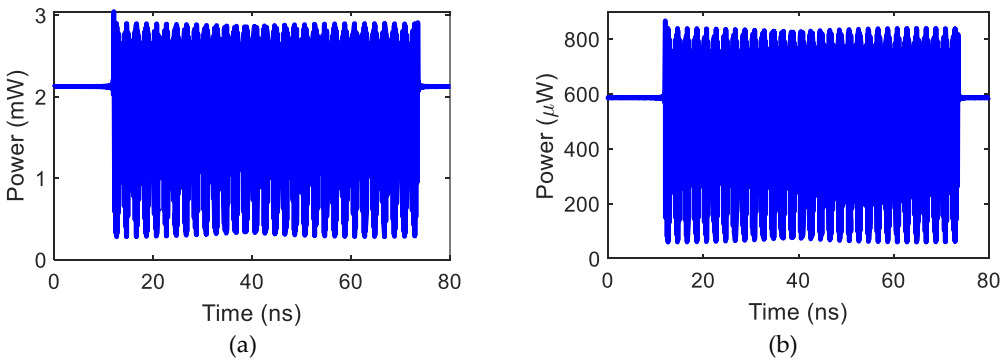

Figure 3.3.17 Output power at Point C (a) and O (b) of the architecture depicted in Figure 3.3.9.

The design features a PAA composed of inset-fed microstrip patch elements printed on a Teflon substrate, with a total footprint of 6×1.5 m^2 and a global directivity of 45 dB. The use of cost-effective materials like Teflon offers the potential for significant cost savings, particularly during experimental testing phases. A fully integrated silicon SSB modulator operating in the Ka-band with a 500 MHz bandwidth is demonstrated, achieving a first sideband suppression of approximately 70 dB through Hartley modulator architecture.
An innovative asymmetrical power splitter based on an MMI structure is introduced, achieving various splitting ratios (ranging from 55% to 95%) without altering the device length, solely by adjusting the defect size in the interferometric region. The splitter exhibits a maximum IL of 1.5 dB. Additionally, the defected 1D photonic crystal-based delay line, characterized by a Gaussian envelope within the photonic bandgap channels, provides a time delay range from 0.7 to 7.3 ps. This range translates into beam steering from 2° to approximately 16° by tuning the laser's central wavelength. The overall system power consumption, approximately 1 kW, significantly reduces the total SAR system power consumption and alleviates EPS power constraints compared to solutions reported in literature and currently on orbit. The proposed system can be integrated into satellite SAR payloads as a key building block, facilitating the transition to fully photonic solutions while preserving power. This integration would reduce payload SWaP, enhance performance, increase system flexibility, improve spectral management, and strengthen EMI resistance.

3.3.3 Reconfigurable Beamforming Metasurface for optical intersatellite links

The rapid rise of CubeSats has reduced both satellite manufacturing and launch costs, fundamentally transforming access to space and enabling widespread participation, particularly from private companies. This shift has altered the paradigm of satellite design, moving away from large, monolithic GEO platforms toward distributed constellations in LEO. LEO constellations provide multiple advantages, including significantly lower latency, enhanced resilience through redundancy, and improved Earth observation capabilities. However, managing such distributed networks requires seamless intersatellite communication to enable coordinated operation, data sharing, and real-time responsiveness.
Initially, RF links, particularly in the S-band, were employed for this purpose. Yet, as data demands continue to rise, the limited bandwidth and heavy spectrum regulations of RF systems are becoming increasingly restrictive. This has accelerated the transition toward Optical Inter-Satellite Links (OISLs), which offer orders-of-magnitude higher capacity while circumventing many of the limitations inherent to RF-based systems. OISLs rely on compact laser communication terminals (LCTs) that are energy-efficient and ideally suited for small satellite platforms. They enable high-speed and secure data transfer using tightly focused laser beams, which inherently reduce interference and avoid the frequency allocation challenges governed by ITU regulations [53].

In a typical OISL, optical signals generated by semiconductor lasers are collimated and steered using micro-optical systems, transmitted across free-space optical channels, and then converted back into electrical signals through photodetectors and associated optoelectronic circuitry [54]. At the heart of this process lies beamforming, a critical function that governs how optical signals are directed, aligned, and optimized for reliable communication. As data volumes and bandwidth demands continue to grow, beamforming technologies are being rapidly commercialized, each bringing unique trade-offs in terms of complexity, integration level, achievable bandwidth, cost, power consumption, and steering performance.

Unlike RF systems, which typically operate in the MHz–GHz range, optical systems exploit carrier frequencies in the hundreds of THz, allowing much broader modulation bandwidths and enabling data rates far beyond those achievable with RF. While RF and microwave systems are generally limited to 100 MHz–1 GHz, optical carriers can exploit approximately 1% of their frequency range, corresponding to hundreds of THz. The extremely short wavelength also results in very high antenna gains with reduced aperture size, which translates into lighter and more compact terminals [55].

A direct comparison between a 1550 nm optical link and a Ka-band RF link (32 GHz) illustrates these benefits. Using Shannon's channel capacity, optical systems provide approximately 2.25–2.51 times higher capacity than RF at a 500 km link distance. Even at lower transmit power (10 W for photonics versus 50 W for RF), optical links still outperform RF systems in terms of antenna gain and field intensity, particularly as the transmit antenna diameter increases [56]. These advantages, however, are counterbalanced by the extremely narrow beam divergence of optical systems. Although such tight beams reduce interference and improve security, they make the links highly sensitive to pointing errors, satellite motion, and potential obstructions. This limitation places strong requirements on Acquisition, Tracking, and Pointing (ATP) mechanisms. The ATP process involves pointing the transmitting terminal within the field of view of its peer, acquiring the incoming beam to establish initial alignment, and maintaining tracking throughout the communication session. These operations account for the longer link establishment times observed in optical systems compared with RF. In practice, the setup of an optical link often takes tens of seconds, which is not negligible when considered within the context of constellation-level network reconfiguration [56]. In-orbit experiments confirm this issue, indeed, the TerraSAR-X and NFIRE satellites successfully established an optical link of up to 5.6 Gbps over distances ranging from 1000 to 5100 km, but the full communication process required 41–52 seconds to complete, including beam acquisition and laser phase locking [57].

Beamforming plays a pivotal role in enabling high capacity intersatellite links, as it directly determines the ability to direct, align, and maintain narrow beams over long distances. With the growing demand for higher bandwidths and ever-increasing data volumes, the commercialization of beamforming antennas has become essential for the development of next-generation satellite communication infrastructures [36]. The main performance requirements for the inter-satellite link are a field of view (FoV) of approximately ±8°, a pointing accuracy and stability of about 8 μrad each, a repointing time shorter than 100 ms, and a low grating lobe level with peak values below –25 dB [58, 59]. These specifications ensure that the optical beam remains

properly aligned between satellites even under dynamic orbital conditions. Since both terminals are located in LEO, the propagation path lies entirely in vacuum, therefore, atmospheric impairments such as turbulence, scintillation, and scattering, which typically affect satellite-to-ground optical links, are absent. This simplifies the link budget and allows the beam-steering and acquisition subsystems to focus primarily on mechanical vibrations, attitude jitter, and relative motion compensation rather than atmospheric mitigation.

Several approaches have been explored to realize beamforming in space applications, with the most relevant falling into three categories: phased-array antennas (PAAs) [60, 61], optical beamforming systems [62, 63], and metasurfaces [64, 65]. PAAs excel in precision and FOV, optical systems in bandwidth and size reduction, and metasurfaces in flexibility and reconfigurability. For instance, phased-array antennas can achieve a wide field of view (FOV) of 80°×17° and a narrow beamwidth of 0.14°×0.14° [66], compared to active metasurfaces, which offer a FOV of 40° and a beamwidth of 2° [67]. Furthermore, metasurfaces tend to have higher design complexity and fabrication costs than PAAs and exhibit lower Side Mode Suppression Ratios (SMSR) [68]. Gradient-index dielectric flat lenses [63] can provide a FOV of ±60°×55°, a beamwidth of 13.6°, and an SMSR of 12.3 dB, though at the cost of limited integration and larger system size. Despite remarkable progress across all three approaches, several challenges must be overcome before these technologies can be fully integrated into commercial satellite networks. Intelligent metasurfaces are constrained by high complexity, shadowing effects, and fabrication costs, while phased-array antennas face limitations in power consumption and thermal management. Optical systems, though highly promising in terms of bandwidth and miniaturization, still lack the integration maturity required for cost-effective deployment.

To address these challenges, it is proposed a planar beamforming network that, for the first time, enables the full integration of all optical transceiver elements on a single chip. Unlike conventional metasurfaces, which operate as reflective or transmissive apertures, steering beams orthogonal to the metasurface plane, the presented solution generates and steers beams directly from a plane-wave signal injected along the cross-section. This structural simplification overcomes the fabrication complexities inherent to metasurfaces and provides a clear path toward cost-effective, scalable mass production.

Metasurfaces consist of arrays of subwavelength elements specifically designed to manipulate the amplitude, phase, and polarization of incident electromagnetic waves, thereby enabling compact and highly controlled wavefront shaping. The proposed structure is implemented as a one-dimensional optical metasurface that achieves dynamic beam control through localized reconfiguration of a phase-change material layer, actuated via an array of integrated microheaters. Electrical switching of the PCM between its crystalline and amorphous phases induces a modulation of material refractive index, allowing for precise, spatially resolved tuning of light–matter interactions.

In this design, the metasurface elements, called meta-atoms, are determined by electrodes that enable electrical control of the PCM status. Local transitions between crystalline and amorphous configurations result in controlled refractive index variations, effectively forming tunable meta-atoms. Through selective activation of

these regions, the device can reconfigure the phase profile across its surface, thereby converting an incident plane wave into either a focused or a directionally steerable optical beam. This approach allows programmable and reconfigurable beam shaping within an integrated and compact platform.

The structure of the device, shown in Figure 3.3.18(a), consists of a 2 μm-thick SiO_2 substrate, a 330 nm Si_3N_4 guiding layer, and a 30 nm film of crystalline antimony selenide (Sb_2Se_3) deposited on top. To mitigate thermal crosstalk and reduce parasitic optical absorption, a 200 nm SiO_2 buffer layer separates the PCM from the metallic heater. The selected thickness values are based on a standard silicon nitride photonic platform, onto which a layer of antimony selenide is deposited with a thickness sufficient to ensure effective confinement of the optical field within the structure. Sb_2Se_3, with refractive index n_{PCM} is chosen due to its large refractive index contrast between amorphous and crystalline states (Δn = 0.7650 at 1550 nm) while maintaining a negligible change in the extinction coefficient [69]. The material is initially deposited in its crystalline phase to minimize the energy and latency of tuning operations.

To define the geometry of the metasurface building blocks, or meta-atoms (see Figure 3.3.18(b)), parametric Finite Difference Time Domain (FDTD) simulations are conducted at the operating wavelength of 1550 nm, assuming the meta-atom in its fully amorphous state, to study the dependence of scattering parameters on the meta-atom dimensions. The design employs a fixed period of 500 nm to ensure fabrication feasibility avoiding thermal crosstalk between consecutive heaters. The results, presented in Figure 3.3.18(c) and (d), reveal that increasing both the length (L) and width (w) slightly reduces transmission but induces a pronounced variation in phase shift. A width of w = 250 nm is selected as the optimal trade-off, maintaining high transmission efficiency while enabling sufficient phase tunability and minimizing the risk of unintended PCM switching caused by thermal crosstalk due to too close electrodes.

Accurate beam shaping requires that each meta-atom be assigned a specific length (L) and refractive index (n) to generate the desired spatial phase profile. In this manner, the phase shift imparted by individual meta-atoms can be tuned from –60° to –150° while preserving high transmission efficiency (see Figure 3.3.19(a) and (d)). The phase shift results negative because the meta-atom acts as an obstacle (as a pole in the transfer function) to the plane-wave propagation, forcing the light to bend toward the surrounding regions of higher refractive index.

Starting from the beam shaping methodology described in [70], these parameters are varied along the y-direction of the metasurface to impose a phase distribution that focuses the beam at a target focal distance of f = 20 μm. The focal length has been chosen to preserve device compactness without increasing the number of meta-atoms. The relation governing this design is given by

$$\phi(y) = \frac{2\pi}{\lambda} n_{eff} \left(f - \sqrt{f^2 - y^2}\right) \tag{10}$$

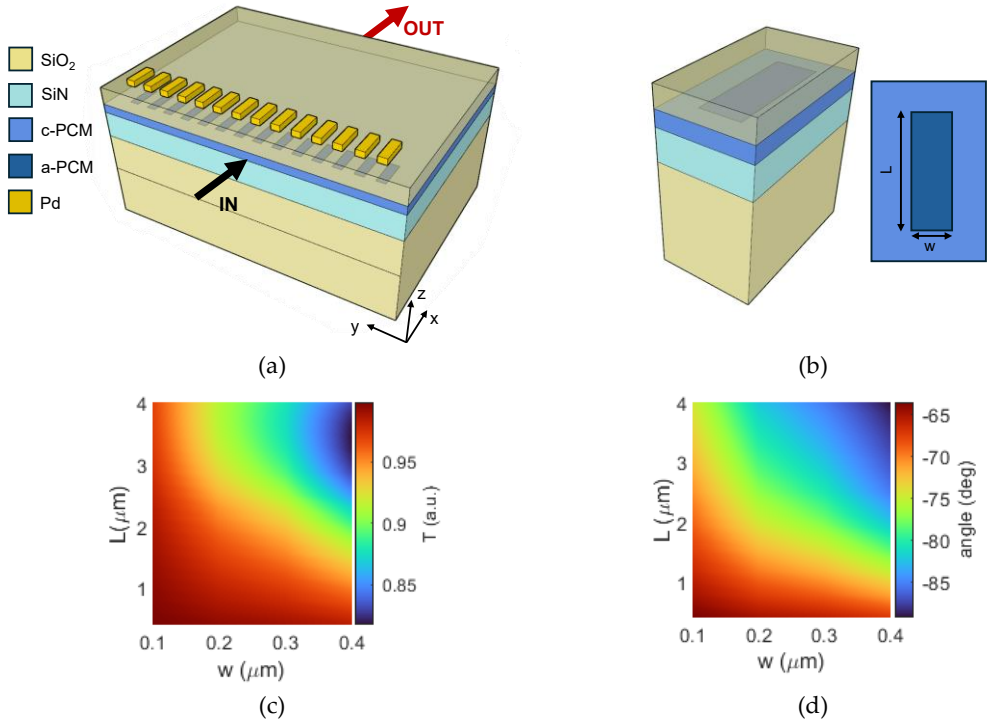

Figure 3.3.18 (a) Sketch of the proposed metasurface (b) Meta-atom structure and design parameters. Meta-atom transmission (c) and phase shift (d) by changing its width (w) and length (L)

Instead, to steer the beam toward the desired angle (θ), each meta-atom must impart a phase shift that is position-dependent along the y-direction and governed by the equation

$$\phi(y) = \frac{2\pi}{\lambda} n_{eff}\, sin(\theta)\, y\, sign(y) \tag{11}$$

The analysis results are presented in Figure 3.3.19(b) and (e), where the phase variation along the y-axis (blue curve) and the corresponding meta-atom lengths (red curve) are reported for both configurations, beam focusing and beam steering at 15°.

Since the lengths of the meta-atoms must remain within practical fabrication limits and cannot be tuned with sub-nanometer precision, the steering length profile does not perfectly reproduce the required phase gradient, in contrast to the focusing case. To achieve the target phase distribution, the design exploits the collective group effect of the metasurface. The simulated performance of the metasurface, obtained by using FDTD method, shows excellent agreement with the theoretical model, as illustrated in Figure 3.3.19(c) and (f). Moreover, it has been demonstrated the capability of steering the beam in a single direction, as illustrated in Figure 3.3.20(a) and (b), achieving a maximum steering angle of ±30° (Figure 3.3.20(c)), and a steering angle of approximately 4° (Figure 3.3.20(d)). These results confirm the versatility of the proposed structure for intersatellite links, enabling the simultaneous establishment of multiple connections if required, while exceeding the target steering angle of ±8° and maintaining sidelobe suppression. Further details on FDTD method are available on Appendix F.

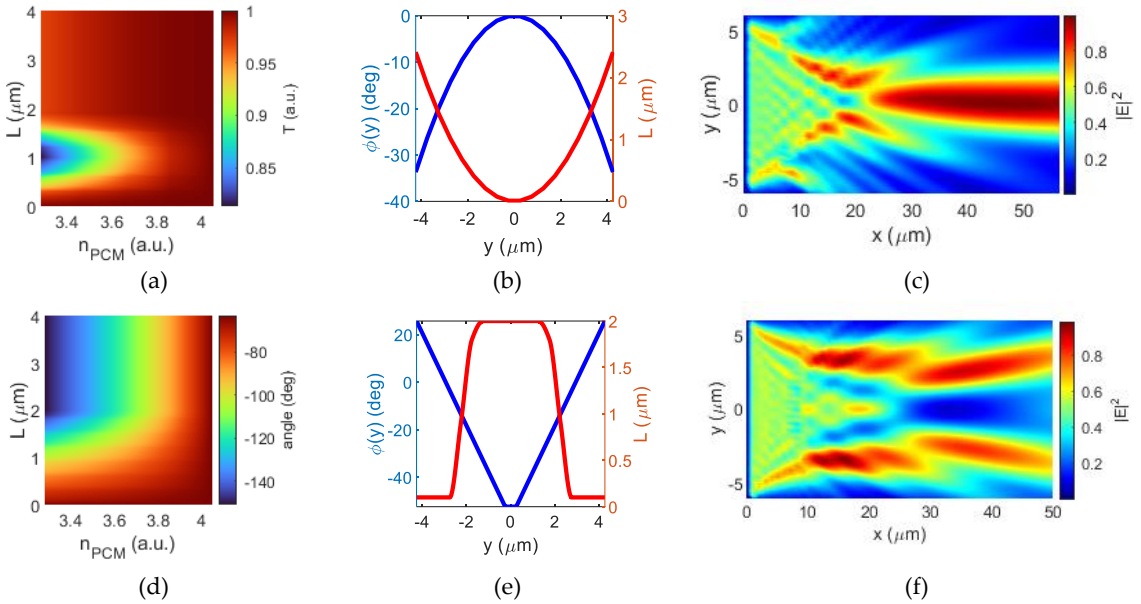

Figure 3.3.19 Meta-atom transmission (a) and phase shift (d) by changing PCM refractive index (n) and its length (L). Meta-atoms phase shift (Φ) and length (L) along the y direction for beam focusing (b) and 15 ° steering (e). Metasurface xy plane in focusing (c) and steering (f) beamforming configurations

Compared with similar configurations reported in the literature [71], the proposed design achieves a substantial reduction in both the total number of meta-atoms, limited to only 18, and their maximum length, confined to 2 μm, as a result of the partial crystallization process of the PCM. The introduction of effective-index modulation further enhances the device performance by simultaneously lowering the power consumption associated with beamforming enabling an exceptionally large steering angle of ±30° within an ultra-compact footprint of 50 × 12 μm².

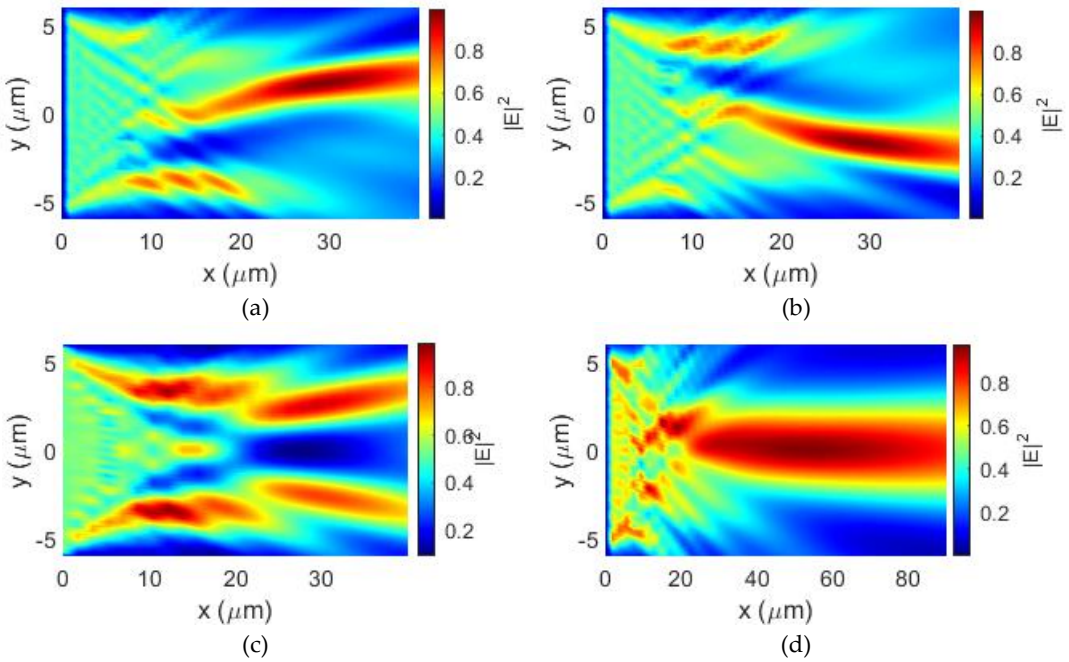

Figure 3.3.20 Electric field intensity propagation along the xy plane for a steering angle of 15° toward left (a) and right (b). Electric field intensity propagation along the xy plane for a steering angle of ±30° (c) and 4°(d)

This advancement broadens the range of potential applications to optical intersatellite links. In contrast with previously reported approaches, the proposed architecture satisfies the stringent performance requirements of intersatellite optical communication while providing a reconfigurable platform fully compliant with NewSpace constraints in terms of SWaP.

The phase transition of Sb_2Se_3 is triggered by applying electrical pulses through palladium electrodes, which raise the PCM temperature to the required levels via the Joule heating mechanism. Usually, amorphization is achieved with a single 130 ns, 8.8 V pulse requiring 105 nJ, whereas recrystallization demands higher energy—about 1.2 μJ—delivered as a sequence of pulses with 20 μs spacing and gradually increasing amplitude from 3.1 to 3.55 V over 1 s [72].

In this case, the phase transition of the Sb_2Se_3 layer is investigated through electro-thermal simulations carried out in COMSOL Multiphysics, employing the coupled AC/DC and heat transfer modules to capture the Joule heating mechanism induced by the driving electrodes. Palladium (Pd) electrodes are placed on top of each PCM meta-atom to control the refractive index of the meta-atoms through amorphization or partial crystallization of the Sb_2Se_3 film. The electrodes, with a width of 300 nm and a thickness of 50 nm, are separated by 200 nm from the PCM layer to ensure efficient heat transfer while preserving optical integrity. To approximate realistic conditions a convective boundary condition is applied to the top surface.

For the crystallization process, the PCM temperature had to achieve its crystallization threshold (≈425 °C), which can be done by carefully tuning the duration and amplitude of the applied pulses. Partial crystallization, essential for precise control of the modal effective index, can be realized by modulating the time spent above the crystallization temperature, enabling continuous tuning of the optical response of each meta-atom. For amorphization, the material should overcome its melting temperature (≈611 °C), followed by rapid quenching down to its glass transition temperature (≈200 °C) [73]. This ensured a fast transition into the amorphous state with excellent repeatability. The switch between the two temperatures should take place with a rate over 10^9 °C/s.

A set of electrical pulses is applied to the electrodes to determine the appropriate voltage and current required for complete amorphization, along with the corresponding power consumption and response time. Figure 3.3.21(a) shows the time-dependent temperature profile of Sb_2Se_3 PCM under a voltage pulse of 100 ns duration and 0.56 V peak amplitude applied to a 2 μm-long heater.

The temperature remains largely confined near the electrode during the trailing edge of the voltage pulse. Once the pulse end, as shown in Figure 3.3.21(b), the electrode temperature decreases and the heat diffuses across the cross-section, causing a delayed temperature rise within the PCM. At the end of the pulse, the temperature in the meta-atom reaches the melting point of 611 °C and then rapidly drops to the glass transition temperature of 200 °C within 160 ns. This corresponds to a cooling rate of $2.58 \cdot 10^9$ °C/s, which guarantees suitable annealing conditions for the PCM.

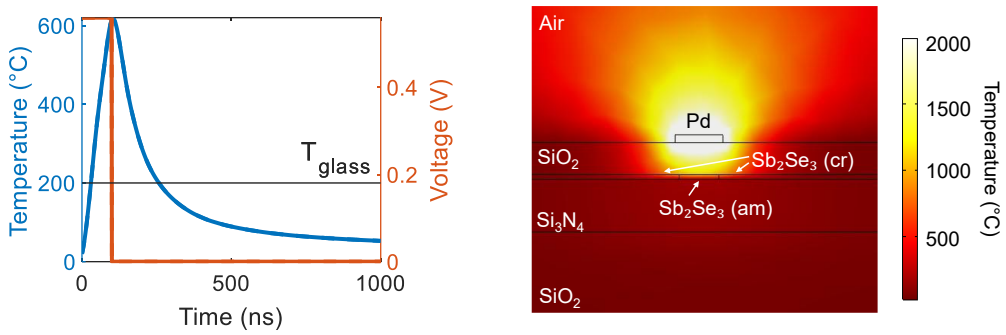

(a) (b)

Figure 3.3.21 (a) The time-dependent thermal response of a PCM meta-atom for a voltage pulse of 0.57V and duration of 100ns. (b) The temperature distribution at the end of the voltage pulse

The simulated results demonstrated great energy efficiency together with an ultrafast reconfiguration time which completely satisfies the Intersatellite link requirement of 100 ms. A single amorphization event required only 2.18 nJ, while the worst-case scenario—simultaneous switching of all 18 meta-atoms from crystalline to amorphous—resulted in a total power consumption of 0.35 W. These values compare very favorably with state-of-the-art thermo-optic tuning mechanisms, which typically demand power levels one to two orders of magnitude higher due to their reliance on continuous heating. Furthermore, the non-volatile nature of Sb_2Se_3 ensures that no static power is required to maintain the programmed optical state, representing a significant advantage in terms of energy savings. Additionally, intermediate refractive index states can be realized through partial crystallization, controlled by adjusting the number of applied pulses while keeping their width and amplitude fixed [72].

Given that the proposed structure is designed for free-space optical communications, its performance is evaluated at the interface between the integrated metasurface and the free-space optical channel. The analysis confirms that the beam remains collimated, although its intensity decreases by an order of magnitude of 8 after propagating in free space at 1 m from the interface.

The interface behavior and far-field distribution for the beam-focusing configuration and 15° one side beam steering are depicted in Figure 3.3.22(a) - (b) and Figure 3.3.22(c) - (d), respectively. The results show that the beam maintains both its shape and beamwidth, confirming stable propagation across the interface. Moreover, the far-field pattern exhibits no sidelobes, with a directivity of 22 dB, while the beam results less collimated (θ_{div} = 0.03 rad) compared to other optical solutions (θ_{div} = 2 μrad [74, 75]), thereby relaxing the requirements of the ATP processes in optical intersatellite links.

The integration of non-volatile phase-change materials substantially reduces power consumption, aligning with the Size, Weight, and Power (SWaP) requirements of NewSpace missions. Moreover, the design employs only 18 meta-atoms with a maximum length of 2 μm, further lowering the energy demands for beam formation and steering while enabling wide-angle control through the partial crystallization of Sb_2Se_3. Far-field simulations validate the metasurface performance, demonstrating that the beam remains well-collimated and preserves its profile after 1 m of free-space propagation, confirming its effectiveness for optical intersatellite links.

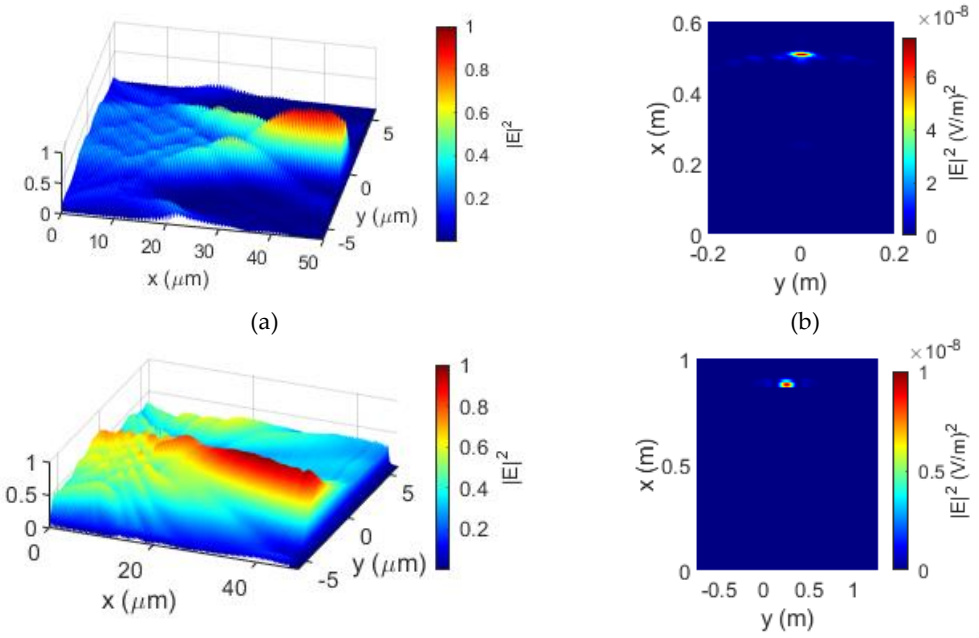

Figure 3.3.22 Electric field intensity at Interface between the chip and the free-space for focused beam (a) and -15° beam steering (c)(b) Farfield of collimated focused beam (b) and -15° beam steering (d).

The proposed planar beamforming metasurface introduces a fundamentally new approach to optical beam generation by employing in-plane injected plane waves. This architecture simplifies fabrication, enhances scalability, and ensures compatibility with standard photonic integration processes. The device achieves a wide field of view of ±30° with a 4° beamwidth, no sidelobes and a directivity of 22 dB, demonstrating excellent optical performance for compact free-space communication systems.

Simulation results confirm beam steering in a single direction with a maximum steering angle of ±30°, exceeding the ±8° range typically required for optical intersatellite links. The metasurface, composed of only 18 meta-atoms with a maximum length of 2 μm, integrates non-volatile Sb_2Se_3 phase-change materials to enable effective index modulation through partial crystallization. This mechanism allows wide-angle beam control with exceptional energy efficiency—requiring only 2.18 nJ per amorphization event and a maximum power of 0.35 W when all meta-atoms are simultaneously switched. These values outperform conventional thermo-optic tuning approaches by one to two orders of magnitude.

The non-volatile nature of the PCM ensures zero static power consumption, aligning perfectly with the stringent SWaP constraints of NewSpace platforms. Furthermore, the metasurface exhibits ultrafast reconfiguration times below 100 ms, fully satisfying intersatellite link requirements. Far-field simulations confirm that the emitted beam remains well-collimated (θ_{div} = 0.03 rad) and stable over 1 m of free-space propagation, with no detectable sidelobes. This behavior mitigates acquisition, tracking, and pointing constraints, confirming the proposed metasurface as a highly efficient, reconfigurable, and scalable platform for next-generation optical intersatellite communication systems.

3.4 Conclusions

This chapter has explored a variety of integrated photonic architectures for optical beamforming networks (OBFNs), each designed to address the growing demand for compact, low-power, and reconfigurable beam steering solutions in the context of the NewSpace economy. The approaches presented highlight how innovations in material platforms, device architectures, and system-level integration can overcome the limitations of conventional thermo-optic technologies while pushing the performance boundaries of photonic phased array antennas.

A first direction has focused on OBFN architectures exploiting phase-change materials (PCMs) to overcome the intrinsic delay–bandwidth trade-off. By employing two- and three-waveguide directional couplers with strategically placed PCM phase shifters, the proposed design achieves a maximum tunable delay of 140 ps while maintaining stable bandwidth performance across PCM refractive index variations. The system exhibits an extremely low total peak power consumption, nearly two orders of magnitude lower than conventional metallic heaters, thanks to the non-volatile nature of the tuning mechanism. Bandwidth reconfigurability from 4.3 to 7 GHz is demonstrated with a delay ripple below 1 ps, supporting continuous beam steering across a ±60° field of view. These results represent a major step forward for wideband, energy-efficient OBFNs capable of driving large phased array antenna systems for 5G communications.

A second one addressed the design and validation of building blocks tailored to spaceborne Synthetic Aperture Radar systems, specifically considering the COSMO-SkyMed requirements in the Ka-band. The architecture demonstrates beam steering without the need for tunable delay lines, thereby simplifying fabrication, lowering costs, and reducing power demands. Key performance results include a phased array antenna with a footprint of 6 × 1.5 m², global directivity of 45 dB, and total system power consumption of ~1 kW—significantly below comparable demonstrated solutions. Additional components include a fully integrated silicon SSB Hartley modulator with 500 MHz bandwidth and 70 dB sideband suppression, an MMI-based asymmetrical splitter with adjustable splitting ratios (55–95%) and low insertion loss (1.5 dB), and a defected 1D photonic crystal delay line offering a time delay of 0.7–7.3 ps, enabling beam steering between 2° and 16°. Collectively, these results demonstrate the feasibility of photonic integration for large-scale SAR payloads while preserving SWaP efficiency.

A comparative simulation was carried out to evaluate the asymmetric power splitter–based beam steering architecture against the TTDL (CROW)-based solution. In this analysis, the cascade of asymmetric power splitters and fixed optical delay lines was replaced by the 1x4 symmetric power splitter and TTDLs one, and the resulting optical power levels collected at each photodiode were examined. The results indicate a significant attenuation in the optical signal, mainly due to the intrinsic insertion losses of commercial integrated power splitters, typically on the order of 8 dB.

When compared to the static configuration, the TTDL-based approach exhibits higher power consumption, confirming that the use of fixed optical delays provides a more energy-efficient solution. Moreover, the microsecond-scale response time of the TTDL, resulting from PCM reconfiguration, is considerably slower than the nanosecond-scale response typically achievable with commercial tunable laser sources used in asymmetric power splitter architectures, highlighting a potential limitation of TTDL-based beam steering for high-speed communication applications.

Finally, a novel planar beamforming metasurface has been introduced, offering a simplified and scalable solution for free-space optical communication systems. The proposed device achieves a ±30° field of view with an 4° beamwidth and complete sidelobe suppression. Leveraging only 18 meta-atoms with maximum length of 2 μm, the structure enables highly compact and energy-efficient operation. The integration of non-volatile Sb_2Se_3 phase-change materials further reduces power consumption while enabling wide-angle beam control through partial crystallization. Simulations confirm that the beam remains well-collimated over propagation distances of 1 m, validating its potential for reliable long-range optical links.

Altogether, the experimental and numerical findings presented in this chapter highlight the transition of OBFN technologies from bulky, power-hungry electronic or thermo-optic systems toward compact, scalable, and energy-efficient photonic implementations. Key numerical benchmarks underscore the progress made in achieving reconfigurability, high selectivity, and SWaP compliance.
In conclusion, the work reported in this chapter demonstrates that integrated photonic OBFNs represent a pivotal enabler for next-generation satellite payloads, Synthetic Aperture Radar systems, and free-space optical communication links. Looking forward, the continued development of phase-change-material-based tuning, metasurface integration, and hybrid photonic-electronic platforms will further enhance speed, resolution, and energy efficiency, paving the way for fully reconfigurable and adaptive beamforming networks capable of meeting the stringent requirements of NewSpace missions.

References

[1] Juniper, "IoT–The internet of transformation 2020," Accessed August 12, 2025. [Online]. Available: https://www.juniperresearch.com/resources/free-research/iot-the-internet-of-transformation-2020/

[2] S.-H. Lim, J.-H. Han, S.-Y. Kim, N.-H. Myung, "Azimuth beam pattern synthesis for airborne SAR system optimization," *Progress in Electromagnetics Research*, vol. 106, pp. 295–309, 2010, doi: https://doi.org/10.2528/PIER10061901

[3] eoPortal, "COSMO-SkyMed," Accessed August 12, 2025. [Online]. Available: https://directory.eoportal.org/web/eoportal/satellite-missions/cmissions/cosmo-skymed

[4] eoPortal, "NovaSar-1," Accessed August 12, 2025. [Online]. Available: https://www.eoportal.org/satellite-missions/novasar-1#mission-capabilities

[5] eoPortal, "SAOCOM (SAR Observation & Communications Satellite)," August 12, 2025. [Online]. Available: https://www.eoportal.org/satellite-missions/saocom#performance-specifications
[6] D. Zhao, R. Lu, Y. Liu, G. Yu, Y. Liu, "A novel beam-steering method for spaceborne interferometric synthetic aperture radar altimeter," in *2018 China International SAR Symposium (CISS*), *Shanghai, China, 2018*, pp. 1-4, doi: https://doi.org/10.1016/10.1109/SARS.2018.8552019
[7] M. I. Abbasi, M. H. Dahri, M. H. Jamaluddin, N. Seman, M. R. Kamarudin, N. H. Sulaiman, "Millimeter wave beam steering reflectarray antenna based on mechanical rotation of array," *IEEE Access*, vol. 7, 2019, pp. 145685-145691, doi: https://doi.org/10.1109/ACCESS.2019.2945318
[8] Y. He, F. Yang, G. Han, Y. Li, "High-throughput SatCom-on-the-move antennas: technical overview and state-of-the-art," *Digital Communications and Networks*, vol. 10, no. 6, 2023, pp. 1760-1768, doi: https://doi.org/10.1016/j.dcan.2023.11.005
[9] A. Boriskin, R. Sauleau (Eds.) Aperture antennas for millimeter and sub-millimeter wave applications. Cham: Springer, 2017, ISBN: 978-3-319-62772-4, doi: https://doi.org/10.1007/978-3-319-62773-1
[10] H. Attia, O. Siddiqui, O. Ramahi, "Theoretical and experimental demonstration of beam steering of patch antenna with superstrate," in *2012 IEEE International Symposium on Antennas and Propagation, Chicago, IL, USA, 2012*, pp. 1-2, doi: https://doi.org/10.1109/APS.2012.6348772
[11] A. S. Hussaini, I. T. E. Elfergani, M. M. Abusitta, A. D. Adebola, R. A. Abd-Alhameed, T. Sadeghpour, J. Rodriguez, "Time modulated switching and reactive loading techniques applied to a circular array antenna using genetic algorithm optimisation," in *7th European Conference on Antennas and Propagation (EuCAP), Gothenburg, Sweden, 2013*, pp. 347-351
[12] K. M. Younus, A. A. Jasim, R. W. Clarke, "A beam steering system design based on phased array antennas," in *1st International Ninevah Conference on Engineering and Technology (INCET 2021), Ninevah, Iraq, 2021*, doi: https://dx.doi.org/10.1088/1757-899X/1152/1/012002
[13] G. Brunetti, N. Sasanelli, N. Saha, G. Campiti, F. Hassan, A. di Toma, M. N. Armenise, C. Ciminelli, "Integrated photonics for NewSpace," in *Berta, R., De Gloria, A. (eds) Applications in Electronics Pervading Industry, Environment and Society. ApplePies 2022*. Lecture Notes in Electrical Engineering, vol 1036. Springer, Cham., 2023, https://doi.org/10.1007/978-3-031-30333-3_39
[14] X. Luo, Engineering optics 2.0 - A revolution in optical theories, materials, devices and systems, 1st ed., Springer: Singapore, 2019, p. 647, ISBN: 978-981-13-5754-1, doi: https://doi.org/10.1007/978-981-13-5755-8
[15] Y. Zeng, S. Qu, J. Wu, "Polarization-division and spatial-division shared-aperture nanopatch antenna arrays for wide-angle optical beam scanning," *Optics Express*, vol. 28, no. 9, 2020, pp. 12805–12826, doi: https://doi.org/10.1364/OE.388951
[16] Y. Guo, Y. Guo, C. Li, H. Zhang, X. Zhou, L. Zhang, "Integrated optical phased arrays for beam forming and steering," *Applied Sciences*, vol. 11, no. 9, 2021, p. 4017, doi: https://doi.org/10.3390/app11094017
[17] S. Q. Li, X. Xu, R. Maruthiyodan Veetil, V. Valuckas, R. Paniagua-Domínguez, A. I. Kuznetsov, "Phase-only transmissive spatial light modulator based on tunable dielectric metasurface," Science, vol. 364, no. 6445, 2019, pp. 1087-1090, doi: https://doi.org/10.1126/science.aaw6747
[18] N. A. Tyler, D. Fowler, S. Malhouitre, S. Garcia, P. Grosse, W. Rabaud, B. Szelag, "SiN integrated optical phased arrays for two-dimensional beam steering at a single near-infrared wavelength," *Optics Express*, vol. 27, 2019, pp. 5851–5858, doi: https://doi.org/10.1364/OE.27.005851
[19] H. W. Rhee, J. B. You, H. Yoon, K. Han, M. Kim, B. G. Lee, S. C. Kim, H. H. Park, "32 Gbps data transmission with 2D beam-steering using a silicon optical phased array," *IEEE Photonics Technology Letters*, vol. 32, no. 13, pp. 803-806, 2020, doi: https://doi.org/10.1109/LPT.2020.2998162
[20] S. H. Kim, J. B. You, Y. G. Ha, G. Kang, D. S. Lee, H. Yoon, D. E. Yoo, D. W. Lee, K. Yu, C. H. Youn, H.-H. Park., "Thermo-optic control of the longitudinal radiation angle in a silicon-based optical phased array," *Optics Letters*, vol. 44, 2019, pp. 411–414, doi: https://doi.org/10.1364/OL.524469
[21] N.-N. Dao, N. H. Tu, T.-D. Hoang, T.-H. Nguyen, L. Nguyen, K. Lee, L. Park, W. Na, S. Cho, "A review on new technologies in 3GPP standards for 5G access and beyond," *Computer Networks*, vol. 245, p. 110370, 2024, doi: https://doi.org/10.1016/j.comnet.2024.110370.

[22] P. Martinez-Carrasco, T. H. Ho, D. Wessel, and J. Capmany, "Ultrabroadband high-resolution silicon RF-photonic beamformer," *Nature Communication*, vol. 15, no. 1, p. 1433, 2024, doi: 10.1038/s41467-024-45743-9.

[23] Z. Ni, L. Lu, Y. Liu, Y. Wang, J. Chen, and L. Zhou, "Silicon-Integrated 8-Channel 6-bit Tunable Optical True-Time Delay Lineswith High Switching Speed and Low Loss," in *2023 International Topical Meeting on Microwave Photonics (MWP), Nanjing, China, 2023*, pp. 1–5. doi: 10.1109/MWP58203.2023.10416568.

[24] D. Lin, S. Shi, P. Liu, W. Cheng, M. Lu, T. Lin, G. Hu, B. Yun, and Y. Cui "Low loss silicon nitride 1×4 microwave photonic beamforming chip," *Optics Express*, vol. 30, no. 17, pp. 30672–30683, 2022, doi: 10.1364/OE.469322.

[25] H. Sun, L. Lu, Y. Liu, Z. Ni, J. Chen, and L. Zhou, "Broadband 1×8 Optical Beamforming Network Based on Anti-resonant Microring Delay Lines," *Journal of Lightwave Technology*, vol. 40, no. 20, pp. 6919–6928, 2022, doi: 10.1109/JLT.2022.3175768.

[26] Y. Liu, A. Wichman, B. Isaac, J. Kalkavage, E. J. Adles, T. R. Clark, and J. Klamkin., "Tuning Optimization of Ring Resonator Delays for Integrated Optical Beam Forming Networks," *Journal of Lightwave Technology*, vol. 35, no. 22, pp. 4954–4960, 2017, doi: https://opg.optica.org/jlt/abstract.cfm?URI=jlt-35-22-4954.

[27] C. G. H. Roeloffzen, M. Hoekman, E. J. Klein; L. S. Wevers,. R. B. Timens, D. Marchenko, "Low-Loss Si3N4 TriPleX Optical Waveguides: Technology and Applications Overview," *IEEE Journal of Selected Topics in Quantum Electronics*, vol. 24, no. 4, pp. 1–21, 2018, doi: 10.1109/JSTQE.2018.2793945.

[28] D. Tripathi, H. S. Vyas, S. Kumar, S. S. Panda, and R. Hegde, "Recent developments in Chalcogenide phase change material-based nanophotonics," *Nanotechnology*, vol. 34, no. 50, p. 502001, 2023, doi: 10.1088/1361-6528/acf1a7.

[29] R. Chen, Z. Fang, F. Miller, H. Rarick, J. E. Fröch, and A. Majumdar, "Opportunities and Challenges for Large-Scale Phase-Change Material Integrated Electro-Photonics," *ACS Photonics*, vol. 9, no. 10, pp. 3181–3195, Oct. 2022, doi: 10.1021/acsphotonics.2c00976.

[30] H. Chen, H. Jia, J. Yang, Y. Tian, and T. Wang, "Ultra-compact switchable mode converter based on silicon and optical phase change material hybrid metastructure," *Optics Communications*, vol. 473, Oct. 2020, doi: 10.1016/j.optcom.2020.125889.

[31] Y. Zhang, Y. Wu, X. Zhang, H. Li, P. Yuan, "Series-coupled fiber double-ring in Mach–Zehnder interferometer for temperature sensing," in *Infrared Sensors, Devices, and Applications, San Diego, California*, *2015*, pp. 73–81, doi: https://doi.org/10.1117/12.2187175.

[32] R. Soref, "Mid-infrared 2×2 electro-optical switching by silicon and germanium three-waveguide and four-waveguide directional couplers using free-carrier injection," *Photonics Research,* vol. 2, no. 5, pp. 102–110, 2014, doi: 10.1364/PRJ.2.000102.

[33] Z. Fang, B. Mills, R. Chen, J. Zhang, P. Xu, J. Hu, A. Majumdar, "Arbitrary Programming of Racetrack Resonators Using Low-Loss Phase-Change Material Sb2Se3," *Nano Letters*, vol. 24, no. 1, pp. 97–103, Jan. 2024, doi: 10.1021/acs.nanolett.3c03353.

[34] A. Taute, S. Al-Jibouri, C. Laprais, S. Monfray, J. Lumeau, A. Moreau, X. Letartre, N. Baboux, G. Saint-Girons, L. Berguiga, and S. Cueff, "Programming multilevel crystallization states in phase-change-material thin films," *Optical Materials Express*, vol. 13, no. 11, pp. 3113–3120, 2023, doi: 10.1364/OME.499809.

[35] C. Ciminelli, N. Saha, G. Brunetti, A. di Toma, M. N. Armenise, "Reconfigurable Optical Beam Forming Network for Telecom Payloads," in *2024 24th International Conference on Transparent Optical Networks (ICTON), Bari, Italy, 2024*, pp. 1-4, doi: 10.1109/ICTON62926.2024.10647596.

[36] K. Luke, Y. Okawachi, M. R. E. Lamont, A. L. Gaeta, and M. Lipson, "Broadband mid-infrared frequency comb generation in a Si3N4 microresonator," *Optics Letters*, vol. 40, no. 21, pp. 4823–4826, 2015, doi: 10.1364/OL.40.004823.

[37] N. Saha, G. Brunetti, C. Ciminelli, "Highly Efficient Phase Change Material Assisted Reconfigurable Optical Delay Line Based on Cascaded Coupled-Resonator Optical Waveguides," *Journal of Lightwave Technology*, vol. 43, no. 17, pp. 8274-8285, 2025, doi: 10.1109/JLT.2025.3583068.

[38] T. Tatoli, D. Conteduca, F. Dell'Olio, C. Ciminelli, M. N. Armenise, "Graphene-based fine-tunable optical delay line for optical beamforming in phased-array antennas," *Applied Optics*, vol. 55, no. 16, pp. 4342-4349, 2016, doi: https://doi.org/10.1364/AO.55.004342.

[39] C. A. Balanis, "*Antenna theory: analysis and design,"* John wiley & sons, 2016. ISBN: 978-1-118-64206-1.

[40] International Telecommunication Union (ITU) Radiocommunication Sector "Recommendation ITU-R RS.1628, Feasibility of sharing in the band 35.5-36 GHZ between the Earth exploration-satellite service (active) and space research service (active), and other services allocated in this band (Question ITU-R 233/7)", ITU, Geneva, Switzerland, Tech. Rep. ITU-R RS.1628, 2003.

[41] W. Glisson, D. Kajfez, J. James, "Evaluation of modes in dielectric resonators using a surface integral equation formulation," *IEEE Transactions on Microwave Theory and Techniques*, vol. 31, no. 12, pp. 1023-1029, 1983, doi: https://doi.org/10.1109/TMTT.1983.1131656.

[42] X. Ge, X. Cai "High extinction ratio optical filters based on high-order silicon microring resonators," in *2018 Conference on Lasers and Electro-Optics Pacific Rim (CLEO-PR), Hong Kong, China, 2018*.

[43] M. D. Salvo, C. Germani, A. Torre, L. Borgarelli, "Ka-band applications for remote sensing from space," in *IEEE Gold 2010, Livorno, Italy, 2010*.

[44] M. S. Alam, X. Li, M. Jacques, Z. Xing, A. Samani, E. El-Fiky, P.-C. Ko, D. V. Plant, "Net 220 Gbps/λ IM/DD transmission in O-band and C-band with silicon photonic traveling-wave MZM," *Journal of Lightwave Technology*, vol. 39, no. 13, pp. 4270-4278, 2021 https://doi.org/10.1109/JLT.2021.3074096

[45] M. Piekarek, D. Bonneau, S. Miki, T. Yamashita, M. Fujiwara, M. Sasaki, H. Terai, M. G. Tanner, C. M. Natarajan, R. H. Hadfield, J. L. O'Brien, M. G. Thompson, "High-extinction ratio integrated photonic filters for silicon quantum photonics," *Optics Letters*, vol. 42, no. 4, pp. 815-818, 2017. https://doi.org/ 10.1364/OL.42.000815

[46] G. Brunetti, N. Sasanelli, M. N. Armenise, C. Ciminelli, "High performance and tunable optical pump-rejection filter for quantum photonic systems," *Optics & Laser Technology*, vol. 139, p. 106978, 2021, doi: https://doi.org/10.1016/j.optlastec.2021.106978

[47] R. R. Kumar, X. Wu, H. K. Tsang, "Compact high-extinction tunable CROW filters for integrated quantum photonic circuits," *Optics Letters*, vol. 45, no. 6, pp. 1289-1292, 2020, doi: https://doi.org/10.1364/OL.384187.

[48] L. Vivien, J. Osmond, J.-M. Fédéli, D. Marris-Morini, P. Crozat, J.-F. Damlencourt, E. Cassan, Y. Lecunff, S. Laval, "42 GHz pin Germanium photodetector integrated in a silicon on insulator waveguide," *Optics Express*, vol. 17, no. 8, pp. 6252-6257, 2009, doi: https://doi.org/10.1364/OE.17.006252

[49] S. Bennets, G. D. McDonald, K. S. Hardman, J. E. Debs, C. C. N. Kuhn, J. D. Close, N. P. Robins, "External cavity diode lasers with 5 kHz linewidth and 200 nm tuning range at 1.55 μm and methods for linewidth measurements," *Optics Express*, vol. 22, no. 9, pp. 10642-10654, 2014, doi: https://doi.org/10.1364/OE.22.010642

[50] Q. Deng, L. Liu, X. Li, Z. Zhou, "Arbitrary-ratio 1×2 power splitter based on asymmetric multimode interference," *Optics Letters*, vol. 39, no. 19, pp. 5590-5593, 2014, doi: https://doi.org/10.1364/OL.39.005590

[51] Z. Sheng, Z. Wang, C. Qiu, L. Li, A. Pang, A. Wu, X. Wang, S. Zou, F. Gan, "A compact and low-loss MMI coupler fabricated with CMOS technology," *IEEE Photonics Journal*, vol. 4, no. 6, pp. 2272-2277, 2012, doi: https://doi.org/10.1109/JPHOT.2012.2230320

[52] A. di Toma, G. Brunetti, P. Colapietro, C. Ciminelli, "High-resolved near-field sensing by means of dielectric grating with a box-like resonance shape," *IEEE Sensors Journal*, vol. 24, no. 5, pp. 6045-6053, 2024, doi: https://doi.org/10.1109/JSEN.2024.3349948.

[53] M. Motzigemba, H. Zech and P. Biller, "Optical Inter Satellite Links for Broadband Networks," in *9th Inter-national Conference on Recent Advances in Space Technologies (RAST), Istanbul, Turkey, 2019*, pp. 509-512. DOI: 10.1109/RAST.2019.8767795.

[54] B. Rödiger, C. Fuchs, J. R. Nonay, W. Jung and C. Schmidt, "Miniaturized Optical Intersatellite Communica-tion Terminal – CubeISL," in *IEEE International Conference on Communications Workshops (ICC Workshops), Montreal, QC, Canada, 2021*, pp. 1-5, DOI: 10.1109/ICCWorkshops50388.2021.9473747

[55] Y. Lee, and J. P. Choi, "Connectivity analysis of mega-constellation satellite networks with optical intersatellite links," *IEEE Transactions on Aerospace and Electronic Systems*, vol. 57, no. 6, pp. 4213-4226, 2021 doi: 10.1109/TAES.2021.3090914

[56] H. Yang, B. Guo, X. Xue, X. Deng, Y. Zhao, X. Cui, C. Pang, H. Ren, S. Huang, "Interruption tolerance strategy for LEO constellation with optical inter-satellite link," *IEEE Transactions on Network and Service Management*, vol. 20, no. 4, pp. 4815-4830, 2023 doi: 10.1109/TNSM.2023.3274638

[57] R. Lange, F. Heine, H. Kämpfner, R. Meyer, "High data rate optical inter-satellite links," In *European Conference on Optical Communication (ECOC 2009), Vienna, Austria, 2009*, vol. 10, No. 1.

[58] CSC Connectivity & Secure Communications, "MONSTER Motionless Optical Beam Steering for Optical Communication Terminals," Accessed May 27, 2025 [Online]. Available: https://connectivity.esa.int/projects/monster?utm_source=chatgpt.com

[59] P. B. Samal, D. N. Thalakotuna, K. P., Esselle, J. Kodithuwakkuge, E. Cetin, "Subarray Antenna Design for Inter-Satellite Communication Link at 60 GHz with Digital Beamforming," In *MILCOM 2024-2024 IEEE Military Communications Conference (MILCOM), Washington, DC, USA, 2024*, pp. 894-899, doi: 10.1109/MILCOM61039.2024.10773776.

[60] C. S. Im, B. Bhandari, K. P. Lee, S.M. Kim, M. Oh, and S. S. Lee, "Silicon nitride optical phased array based on a grating antenna enabling wavelength-tuned beam steering," *Optics Express*, vol. 28, no. 3, pp. 3270-3279, 2020. doi: https://doi.org/10.1364/OE.383304

[61] X. Guo, Z. Li, H. Chen, Y. Li, M. Ye, X. Zhang, and Y. Yu, "Two-dimensional silicon optical phased array with large field of view," *Optics Express*, vol. 30, no. 15, pp. 28049-28056, 2022. doi: https://doi.org/10.1364/OE.463043

[62] F. E. Helmy, I. I. Ibrahim, and A. M. Saleh, "Beam-steering of dielectric flat lens nanoantenna with elliptical patch based on antenna displacement for optical wireless applications," Scientific Reports, vol. 13, p. 16030, 2023. DOI: https://doi.org/10.1038/s41598-023-43149-z

[63] H. Li, C. Zhou, W. B. Lee, D.Y. Choi, and S.S. Lee, "Flat telescope based on an all-dielectric metasurface doublet enabling polarization-controllable enhanced beam steering,". *Nanophotonics*, vol. 11, no. 2, pp. 405-413, 2022. doi: https://doi.org/10.1515/nanoph-2021-0609

[64] J. Tao, Q. You, Z. Li, M. Luo, Z. Liu, Y. Qiu, Y Yang, Y. Zeng, Z. He, X. Xiao, G. Zheng, and S. Yu, "Mass-manufactured beam-steering metasurfaces for high-speed full-duplex optical wireless-broadcasting communications," *Advanced Materials*, vol. 34, no. 6, p. 2106080, 2022. DOI: https://doi.org/10.1002/adma.202106080

[65] A, Cala' Lesina, D. Goodwill, E. Bernier, L. Ramunno, and P. Berini, "On the performance of optical phased array technology for beam steering: effect of pixel limitations," *Optics Express*, vol. 28, no. 21, pp. 31637-31657, 2020. doi: https://doi.org/10.1364/OE.402894

[66] D. NO. Hutchison, J. Sun, J. K. Doylend, R. Kumar, J. Heck, W. Kim, C.T. Phare, A. Feshali, H. Rong, "High-resolution aliasing-free optical beam steering," *Optica*, vol. 38, pp. 887–890, 2016, doi: https://doi.org/10.1364/OPTICA.3.000887

[67] Y.-W. Huang, Ho. W. H. Lee, R. Sokhoyan, R. A. Pala, K. Thyagarajan, S. Han, D. P. Tsai, H. A. Atwater, "Gate-tunable conducting oxide metasurfaces," *Nano Letters*, vol. 16, no. 9, pp. 5319–5325, 2016, doi: https://doi.org/10.1021/acs.nanolett.6b00555.

[68] S. Lin, Y. Chen, Z. J. Wong, "High-performance optical beam steering with nanophotonics," *Nanophotonics*, vol.11, no. 11, pp. 2617-2638 2022, doi: https://doi.org/10.1515/nanoph-2021-0805.

[69] J. Liang, Z. Zhu, Y. Dong, L. Lei, Y. Li, M. Shen, and X.D. Xiang, "Simulation of Gap Structure Optical Waveguide with Phase Change Materials," In *2022 IEEE Asia Pacific Conference on Circuits and Systems (APCCAS), Shenzhen, China, 2022*, pp. 454-457. doi: 10.1109/APCCAS55924.2022.10090290

[70] S. Abdollah Ramezani, K. Arik, S. Farajollahi, A. Khavasi, Z. Kavehvash, "Beam manipulating by gate-tunable graphene-based metasurfaces," *Optics Letters*, vol. 40, no. 22, pp. 5383-5386, 2015. doi: https://doi.org/10.1364/OL.40.005383

[71] S. Zarei, "On-Chip Wavefront Shaping with Rewritable Phase-Change Metasurfaces," in *2024 International Semiconductor Conference (CAS), Sinaia, Romania, 2024*, pp. 87-90. doi: 10.1109/CAS62834.2024.1073676

[72] X. Yang, L. Lu, Y. Li, Y. Wu, Z. Li, J. Chen, L. Zhou, "Non-volatile optical switch element enabled by low-loss phase change material," *Advanced Functional Materials*, vol. 33, no. 42, p. 2304601, 2023, doi: https://doi.org/10.1002/adfm.202304601

[73] U. Wijesinghe, W. D. Tetlow, P. Maiello, N. Fleck, G. O'Dowd, N. S. Beattie, G. Longo, O. S. Hutter, "Crystalline Antimony Selenide Thin Films for Optoelectronics through Photonic

Curing," *Chemistry of Materials*, vol. 36, no. 12, pp. 6027-6037, 2024, doi: https://pubs.acs.org/doi/10.1021/acs.chemmater.4c00540.

[74] V. Sharma, N. Kumar, "Improved analysis of 2.5 Gbps-inter-satellite link (ISL) in inter-satellite optical-wireless communication (IsOWC) system," *Optics Communications*, vol. 286, pp. 99-102, 2013, doi: https://doi.org/10.1016/j.optcom.2012.08.055.

[75] N. Kaur, G. Soni, "Performance analysis of inter-satellite optical wireless communication (IsOWC) system at 980 nm and 1550 nm wavelengths," In *2014 International Conference on Contemporary Computing and Informatics (IC3I), Mysore, India, 2014*, pp. 1245-1250, doi: 10.1109/IC3I.2014.7019624.

Chapter 4

On-board data processing through Photonics

4.1 Introduction

Data Handling Systems (DHS) and On-Board Computers (OBCs) represent the core of modern spacecraft, integrating telecommand and telemetry modules, mass memories, data storage units, remote terminal units, and standardized communication buses. Indeed, these systems are always present in space projects and are driven by constantly evolving requirements across science, exploration, Earth observation, and telecommunications. Their development is tightly coupled with progress in software technologies, including validation and verification techniques.

In addition to the classical constraints of increasing processing power while minimizing mass, volume, and power budgets, new challenges arise from the definition of next-generation missions. These include the adoption of advanced communication standards, the development of new software architectures, and the application of industrialized procedures to enable rapid production, particularly relevant for satellite constellations. Earth observation missions are characterized by the need for high-throughput data links, expanded onboard storage capacity, and secure architectures protecting both payload data and spacecraft operations, while science missions demand greater modularity and support for multiple instruments [1]. The balance between mission lifetime, cost, and reliability is also shifting. Traditional long-life satellites still require fully space-qualified components, but for shorter missions even agencies such as NASA are increasingly adopting Commercial-Off-The-Shelf (COTS) components. For instance, NASA's Jet Propulsion Laboratory has demonstrated the use of 30 Krad COTS boards in experimental satellites, and the NASA NEPP program promotes the tailored use of EEE parts in small missions below 500 kilograms, and in many cases below 100 kilograms. This strategy is particularly attractive in the fast-growing market of telecom mega-constellations such as OneWeb [2].

In Europe, one of the most significant long-term R&D efforts is the development of radiation-hardened SPARC processors. Initiated in the 1990s with the ERC32 project [3], the European Space Agency launched the LEON program with the goal of providing higher performance, modularity, reliability, and standard interfaces for avionics systems. LEON2 was initially conceived as an Application-Specific Standard Product, exemplified by Atmel's AT697F processor in 2009, but it quickly evolved into a versatile platform for system-on-chip implementations [4]. The availability of radiation-hardened PLDs, particularly the ACTEL/Microsemi RTAX series, enabled the realization of efficient SoC architectures and first-silicon-good ASICs. Today, the LEON ecosystem, supported by ESA and Cobham-Gaisler, has matured into a portable and CAD-tool-independent solution spanning both ASICs and FPGAs. It has been successfully deployed in missions such as VENUS-Express, in large constellations like Iridium-Next, and in numerous bespoke SoC designs, ensuring continuity in hardware and software development across different mission contexts [1].

As spacecraft become increasingly complex, designers face the challenge of meeting ever more demanding functional requirements while reducing resources, time, and costs. This environment emphasizes the importance of first-time-right scalable designs that rely on reusable and validated building blocks. Microcontrollers and SoC-based architectures play a critical role in this process, as they offer flexibility, low cost, and the possibility of tailoring hardware and software solutions to the specific needs of each mission.

Parallel efforts are exploring the role of FPGAs and GPUs in space applications, particularly for image and video processing. However, there is rarely a universally optimal solution, since each application must balance trade-offs among performance, power, energy, size, reconfigurability, fault tolerance, and design complexity.

The broader trends in the semiconductor industry are also shaping space electronics. As Moore's Law slows down, the focus is shifting away from general-purpose processors and toward application-specific system-on-chip designs. These architectures consolidate multiple functions, enhance payload data processing, and enable advanced memory management supported by higher-level operating systems. The ongoing pursuit of new microprocessors in the space sector is therefore directed at achieving more functionality with fewer components, increasing processing power in payload controllers and mass memory systems, and enabling tighter integration between instrument control and data processing units. Given the limitations of current ASIC technologies, this progress depends on the adoption of deep submicron technologies, new architectures, higher-frequency single-core processors, and multi-core solutions optimized for space environments [1]. Specialized architectures, such as dedicated Artificial Intelligence (AI) accelerators, have been investigated but even these application-specific engines are reaching boundaries that cannot easily be overcome with electronics alone, making it necessary for processors to converge with complementary technologies to satisfy the short- and mid-term requirements of space missions.

Integrated photonics emerges as a promising candidate to extend these capabilities. By enabling the generation, processing, distribution, and detection of light signals directly on chip, photonics offers unique features unattainable in electronics, including ultrawide bandwidth, inherently low latency, reduced transmission losses, and natural parallelism through wavelength-division multiplexing. In direct analogy with the evolution of electronics, the concept of software-defined photonics has recently emerged, allowing the dynamic reconfiguration of hardware through the coordinated control of several actuators [5]. This paradigm grants unprecedented versatility in manipulating light paths and properties on-chip, thereby enabling a broad spectrum of architectures optimized for specific functionalities. Early demonstrations of moderate-scale photonic processors have already shown remarkable performance in microwave photonics, signal acceleration for machine learning inference, and advanced optical or quantum information processing [6-8]. Nonetheless, current implementations still lack the system-level complexity, scalability, and flexible programmability required for future large-scale applications. Limitations such as restricted optical port counts, reconfiguration speeds, signal degradation, and integration with software interfaces remain key bottlenecks. To overcome these challenges, the transition to large-scale photonic processors—incorporating tens of thousands of actuators, advanced calibration and control strategies, and software-defined architectures tailored to communications, networking, and computing domains—will be crucial. Such processors promise to combine the maturity of electronic platforms with the transformative advantages of photonics, opening a path toward disruptive improvements in bandwidth, energy efficiency, and scalability for next generation spaceborne and terrestrial systems.

4.2 Photonic Processors

Programmable photonic integrated circuits (PICs) rely on multiple functional layers to provide reconfigurable and scalable processing capabilities. At the core lies a programmable mesh of photonic gates interconnected with control electronics, optical fibers, and high-speed modulators and detectors that enable transduction between the optical and microwave domains. The photonic chip is integrated within a package that also hosts the required analog and digital driver electronics, designed in compliance with stringent thermal, mechanical, hermeticity, and electromagnetic compatibility (EMC) constraints. On top of the hardware stack, software algorithms and programming layers provide user access to the photonic functionalities, thus bridging device-level operation with system-level applications (see Figure 4.2.1).

All elements of the processor are connected to a two-dimensional reconfigurable waveguide mesh, which allows the creation of specific processing engines and the dynamic interconnection of both internal and external modules required for different functions. A critical aspect of these platforms is the mitigation of optical-to-RF conversion losses, which arise mainly from the limited efficiency of modulators, photodetectors, and propagation paths. To compensate for these

losses, arrays of optical amplifiers, preferably semiconductor optical amplifiers (SOAs) implemented in InP, may be required. Optimizing their allocation within or outside the mesh is still an open research problem, and hybrid integration strategies involving dedicated amplification layers are being actively investigated [9].

The versatility of a programmable mesh depends strongly on the number of tunable basic units (TBUs). A larger number of TBUs increases functionality and flexibility but introduces significant practical challenges. Accumulated propagation losses, imperfect splitting ratios, limited phase control accuracy, parasitic reflections, imbalance losses, fabrication-induced gradients, and temporal drifts all degrade system performance. Moreover, there exists a fundamental trade-off between miniaturization and accumulated losses. The minimum delay is determined by the basic unit length (BUL) and the waveguide group index. For low-index-contrast platforms, the BUL is constrained by the tuning mechanism length and the 3 dB coupling length, implying that shorter BULs require the signal to pass through a larger number of TBUs to achieve a desired delay, thereby increasing cumulative losses [9-10].

The tuning mechanism further determines the ultimate length, power consumption, and crosstalk of each TBU. Thermal tuning, although widely used, imposes limits on scalability due to high energy consumption ($P_\pi \cdot$ TBU). Alternative mechanisms based on MEMS, piezoelectric, or electromechanical actuation represent promising solutions to reduce power consumption, minimize crosstalk, and allow denser integration by reducing the spacing between interferometer arms. These approaches could greatly enhance scalability and operational efficiency [10].

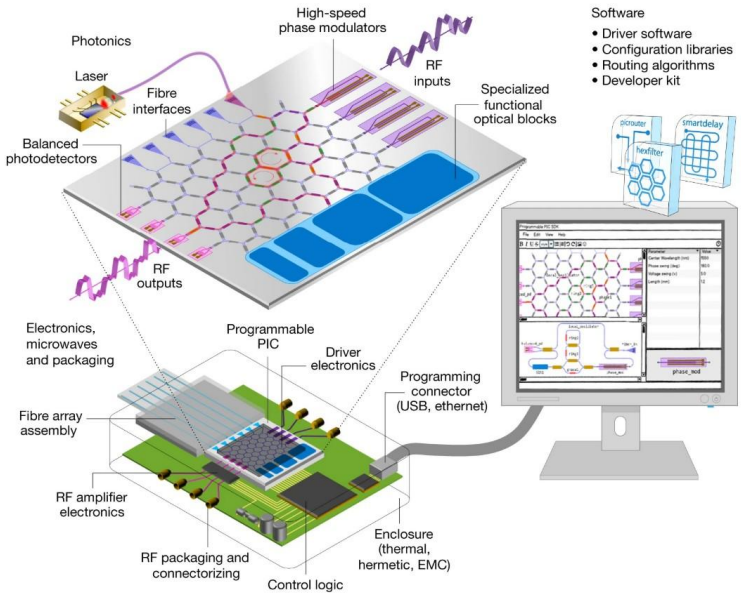

Figure 4.2.1 Programmable photonic integrated circuits are made of a programmable mesh of photonic gates connected by optical fibres to high-speed modulators and detectors packaged together with analogue and digital driver electronics. The chip is controlled by software algorithms [10].

Another practical issue lies in real-time control of the TBU bias points within the mesh. Machine learning techniques have been proposed as a solution to enable automated mesh initialization, self-configuration, and continuous monitoring of processed signals by analyzing output port behavior. Such approaches may significantly improve stability and adaptability in large-scale meshes.

From a theoretical perspective, two major challenges remain. The first is the development of scalable analysis methods capable of rendering arbitrary input-output transfer functions independently of the number of cells in the waveguide mesh. The second is the synthesis of multiport feedback circuits and recirculating interferometers through direct implementation within the mesh, without relying exclusively on circuit emulation. Future research should thus aim to exploit the intrinsic capabilities of two-dimensional meshes for direct implementation of complex transformations [11].

The best performance recorded so far regards a reconfigurable photonic processor integrated on a silicon-on-insulator platform, featuring a mesh of 72 programmable unit cells (PUCs) arranged in a flattened hexagonal topology. Each PUC is a Mach–Zehnder interferometer with thermo-optic phase shifters, enabling independent control of coupling and phase. The chip incorporates 40 output ports, integrated high-performance filters, on-chip photodetectors, and a monitoring array for closed-loop feedback.

Electrical control is provided through a programmable current source, while software layers ensure temperature stabilization, component actuation, and application-level automation. Characterization across multiple wafers shows insertion losses of ~0.48 dB/PUC, phase tuning efficiency of 1.3 mW/π, propagation losses of 1.5–2.5 dB/cm, and fiber-to-chip coupling losses of 1.5–3 dB per facet. The system demonstrates reconfiguration times of 15–90 ms and operation in the 15–45 GHz band, with scalability toward higher frequencies by reducing the BUL. Power consumption per phase shifter is in the 1–2 mW/π range, suggesting that a processor with over one thousand PUCs could operate at ~2 W [12].

Despite these advances, several limitations remain. Performance is constrained by propagation and scattering losses, tuning efficiency, and the relatively slow thermo-optic actuation. The fiber–chip coupling losses and accumulated insertion losses pose significant barriers to scaling toward larger meshes. Furthermore, while the architecture provides remarkable flexibility, its energy efficiency and speed may not meet the stringent requirements of emerging high-performance applications.

In this context, the comparison between Field-Programmable Photonic Gate Arrays (FPPGAs) and Application-Specific Photonic Integrated Circuits (ASPICs) becomes central. A tunable ASPIC is a device engineered to perform a dedicated function, either with a fixed configuration or with limited tunability to adapt its behavior to user requirements [13]. Tuning is typically achieved through thermo-optic or electro-optic mechanisms. The thermo-optic effect exploits temperature-induced refractive index variations, offering relatively low power consumption and microsecond-scale reconfiguration speeds. The electro-optic effect, instead, relies on refractive index changes induced by an external

electric field, enabling nanosecond response times but at the expense of higher losses and a reduced wavelength tuning range [14, 15].
Although both ASPICs and Programmable Photonic Integrated Circuits (PPICs) have been intensively investigated, their roles are inherently complementary. PPICs provide maximum flexibility, since a single mesh-based platform can be reconfigured to implement multiple functionalities, reducing engineering costs and accelerating prototyping. However, this versatility comes with penalties, higher propagation losses, larger power consumption, and fabrication complexity due to the stringent reproducibility required for large 2D meshes. ASPICs, by contrast, sacrifice reconfigurability in favour of highly optimized performance. Tailored design enables circuits with significantly lower insertion losses, reduced power consumption, and improved reproducibility, making them better suited for applications where efficiency and reliability are paramount.
The choice between PPICs and ASPICs will depend on the application domain. Much like in electronics, programmable processors are ideal for early-stage exploration and multi-functional platforms, while ASPICs remain the only viable option when stringent requirements on loss, energy efficiency, and large-scale deployment must be satisfied. Their successful development would mark a significant leap beyond the limitations of electronic-only processors, establishing photonic integration as a cornerstone for next-generation spaceborne and terrestrial systems.

4.3 Photonic FFT processor for SAR on-board processing

In the space domain, Synthetic Aperture Radar (SAR) systems stand to benefit significantly from photonic integration, as it enables high performance and novel functionalities while ensuring far greater compactness and reduced mass compared to conventional SAR platforms (for instance, Cosmo-SkyMed has a mass on the order of several tons). Detailed information on conventional SAR system are provided in Appendix E. High-resolution imaging, which is critical for Earth Observation (EO), relies on continuous advancements in SAR payloads. Photonic technologies have been proposed to enhance multiple stages of SAR chain, such as chirped waveform generation [16], optical beamforming [17], and photonic filters [18] of radar echoes. These implementations have demonstrated not only remarkable improvements in SAR performance but also significant reductions in SWaP consumption. Looking ahead, in support of the emerging NewSpace economy, a transformative step could involve replacing the electronic A/D converter with a photonic processor, enabling fully optical, on-board data processing and paving the way toward an all-optical SAR system.
Nowadays, pre-processing is performed in the electronic domain, and the collected information must be stored in memory systems until the satellite establishes a link with a ground station to which the SAR data acquired up to that point can be transmitted. However, as spatial resolution increases and transmission channels become increasingly congested, it is no longer feasible to downlink all the acquired data. Doing so would saturate the available

bandwidth, waste a significant amount of power, and ultimately be inefficient, especially since a large portion of the data does not contain useful information. Therefore, it becomes essential to develop systems capable of discarding redundant or irrelevant data and performing a selection process prior to transmission, ensuring that only the most relevant information is sent to the ground.

SAR imaging relies heavily on Fast Fourier Transform (FFT)-based algorithms to compress and process echo data directly on-board. The FFT is an efficient algorithm for computing the discrete Fourier transform (DFT) of a set of N time samples, where N is an integer power of two, and is expressed as

$$\boldsymbol{X_k} = \sum_{n=0}^{N-1} \boldsymbol{x_n e^{-\frac{j2\pi}{N} \cdot k \cdot n}} = \sum_{n=0}^{N-1} \boldsymbol{x_n w_N}^{k \cdot n}, \qquad \boldsymbol{k} = \boldsymbol{0, \ldots, N-1} \tag{12}$$

where w_N is the weight coefficient, x_n represents the vector of N time samples, and X_k is the resulting vector of N frequency-domain samples. Constructing the weight matrix $W_{N\times N}$ by multiplying w_N for each n, k = 0, …, N−1, and then multiplying it by the input vector of time samples yields the FFT.

Among the most widely adopted approaches are the Range-Doppler (RD) and ωk algorithms, which sequentially process range and azimuth data by exploiting the approximate separability of the two dimensions. The RD algorithm performs FFT of both the range reference function and the range echo data, applies compensation and compression, and subsequently returns to the spatial domain through an inverse FFT (IFFT). After transposition, the same procedure is applied to azimuth data to obtain the final image [19]. The ωk algorithm, instead, operates in the wavenumber domain, which facilitates real-time processing, improves error correction for motion-induced instabilities, and enables the handling of wide apertures and large squint angles [20].

In current SAR payloads, FFT operations are performed electronically using large-scale FPGAs, dedicated ASICs, or Monolithic Microwave Integrated Circuits (MMICs). After A/D conversion, these systems employ filtering, decimation, and parallel processing through multiple DSPs. However, this approach remains computationally and energetically expensive, for instance, compressing 256k pulses at a 1 kHz frequency requires at least three DSPs and 2.8 ms of processing [20]. GPUs can improve computational efficiency, but electronic architectures inherently suffer from limitations related to power dissipation, parasitic interconnection, and latency, constraining their scalability for future high-resolution missions.

Photonic implementations of FFT have been widely explored as an alternative to electronic architectures, driven by the need to overcome limitations in power dissipation, delay, and scalability. The basic rationale lies in the natural ability of optical systems to perform linear operations such as additions, subtractions, and phase shifts through interference, as well as the intrinsic parallelism of wave propagation, which allows multiple operations to be executed simultaneously at the speed of light. The earliest attempts to realize optical FFT relied on free-space optical systems [21, 22]. Lenses were used to map signals into the frequency

domain through diffraction, where spectral filtering could be applied, and then reconverted to the spatial domain using a second lens [23]. While these approaches elegantly exploited the Fourier-transform property of lenses, they were inherently bulky, lacked integration, and were highly susceptible to environmental perturbations such as misalignment and external noise. Later free-space diffractive networks improved flexibility by shaping complex diffraction patterns for computation, but they remained unsuitable for spaceborne systems due to their volume, weight, and difficulty in reconfiguration [24].

Alternative solutions employed dispersive devices, such as optical fibers or fiber loops combined with time lenses, to exploit group velocity dispersion for implementing Fourier transforms in the temporal domain [25]. These systems demonstrated low-latency operation and even real-time short-time Fourier transform processing. However, they required long optical paths, operated within limited signal bandwidths, and introduced bulky setups that restricted their applicability in compact platforms.

With the advent of integrated photonics, more scalable approaches have been investigated. Cascaded interferometric structures, in particular Mach-Zehnder Interferometers (MZIs), became the cornerstone of integrated optical FFT processors. MZIs can be arranged to implement the Cooley–Tukey butterfly cell, where phase rotations are obtained by short differential waveguides and delays are introduced through longer path differences [26]. This scheme significantly reduces the number of interferometers required compared to early architectures, scaling as $\frac{1}{2}N\log_2(N)$ instead of $\frac{1}{2}N(N-1)$ [27]. Furthermore, integrated photonic platforms such as silicon photonics or indium phosphide allow dense integration of MZIs with precise phase control, paving the way toward compact and robust FFT processors.

Nevertheless, integrated MZI-based architectures also face non-negligible challenges. As the number of samples increases, the total footprint grows due to the spirals needed for long delays, and the cumulative insertion losses become substantial, particularly at waveguide crossings. Additional constraints arise from the need for heaters or electro-optic phase shifters to calibrate phase errors and fabrication tolerances, which lead to increased power consumption and reduced stability. Some approaches mitigate these issues by incorporating phase-change materials to enable reconfigurable and non-volatile phase control, though these technologies are still in development [24, 28, 29].

4.4 Proposed Integrated Photonic FFT Processor

The novel architecture proposed here addresses the main limitations of existing approaches such as the bulkiness and susceptibility to external noise in free-space optical FFTs, the limited scalability, large footprint, and high power consumption of cascaded MZI-based FFTs, the scalability issues, footprint, insertion losses, and calibration requirements of butterfly-pattern optical FFTs, and the power dissipation, latency, and limited processing speed of

conventional electronic FFT processors, while preserving the processing requirements of SAR systems.

It is proposed a flexible and reconfigurable $LiNbO_3$-based architecture capable of performing fully optical, real-time extrapolation and processing of each echo's spectral component. The system is implemented using a demultiplexer (De-MUX), an array of tunable phase shifters, and a multiplexer (MUX) operating in the Ka-band (see Figure 4.4.1(a)). The selection of the Ka-band (40 GHz), rather than the C-band (5.405 GHz) used in the Copernicus mission, is motivated by its potential to enable a full optical SAR through the integration of components already demonstrated in the photonic domain, such as linearly chirped waveform generators (LCWGs) [16], beamforming networks [17], and tunable delay lines [30]. Furthermore, the Ka-band offers additional advantages, including reduced antenna size and weight, a shorter baseline between satellites in interferometric SAR (InSAR) missions, and the capability to generate digital elevation model (DEM) images that more closely represent physical reality. This is because, at Ka-band frequencies, radar pulses are reflected primarily from the surface of objects, rather than penetrating into their volume [30].

In the proposed integrated photonic architecture, the system receives echoes at the SAR carrier frequency f_c. The signal is up-converted to optical frequencies by means of a single-sideband (SSB) modulator, generating SAR echo beats with the laser frequency f_0 . The resulting signal at f_0 -f_c is sampled at frequency f_s using an electro-optical Mach–Zehnder modulator (EO-MZM). To separate the 256 wavelength channels (corresponding to 8-bit sampled wavelengths) generated by the EO-MZM, an arrayed waveguide grating (AWG), acting as a demultiplexer, is employed. The separated wavelengths are then weighted according to the first column of the weight matrix $W_{N\times N}$ using 2^8 electro-optical (EO) phase shifters, each driven by properly estimated voltages. A second AWG, symmetric to the first, recombines the weighted wavelength channels, yielding the first FFT spectral component of the received echo.

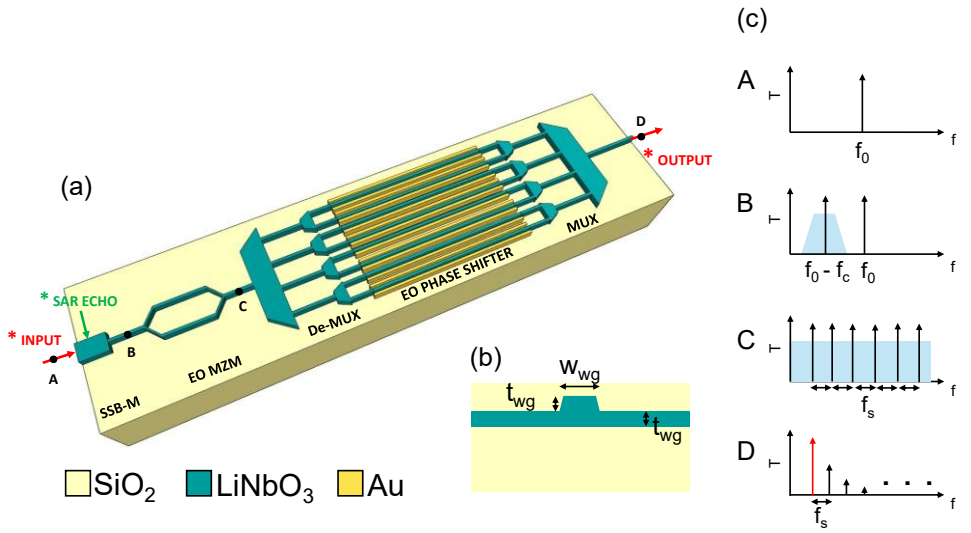

Figure 4.4.1 (a) Sketch of the designed OFFT architecture (SSB-M: Single-Side Band Modulator, EO MZM: Electro-Optical Mach-Zehnder Modulator, De-MUX: demultiplexer, EO PHASE SHIFTER, MUX: multiplexer) (b) Cross-section of the chosen technological platform. (c) Extracted spectra at different points in the device [31]

By subsequently reconfiguring the array of EO phase shifters, the second FFT spectral component can be obtained, and this process can be repeated until the entire spectrum is reconstructed by summing all the components. The overall structure is illustrated in Figure 4.4.1(a) while the signal manipulation is highlighted in Figure 4.4.1(c).

The system specifications, the carrier frequency (f_c = 40 GHz), the sampling frequency (f_s = 300 MHz), and the number of time samples (N = 2^8), have been defined with reference to the Copernicus Sentinel-1 requirements [32]. Copernicus Sentinel-1 is a constellation of two satellites, Sentinel-1A and Sentinel-1B, operating in the same orbital plane with a 180° phasing, together forming the European Radar Observatory. The mission provides a continuous and independent C-band SAR mapping capability with improved revisit frequency, coverage, timeliness, and reliability, enabling long time-series applications [33]. Transitioning from the C-band to higher frequencies, such as the Ka-band, reduces SAR antenna SWaP, enhances spatial resolution, and ensures compatibility with the photonic SAR building blocks discussed previously. The laser central frequency (f_0 =1550 nm) is selected for compatibility with commercially available laser sources, instead.

To ensure low propagation losses while maintaining high tuning efficiency, lithium niobate is selected as the technological platform, offering losses as low as 2.8 dB/m at 1550 nm [34]. In recent years, thin-film lithium niobate (TFLN) has emerged as a promising material platform for high-performance photonic integrated devices. Its advantages include high-speed operation, compactness, modest driving voltages, low optical losses, strong material anisotropy, and a large Pockels coefficient. These properties have made $LiNbO_3$ widely adopted for optical delay lines, polarization control devices, and EO modulators [35-37]. The strong anisotropy of the material allows selective control of the electric field polarization, ensuring high response speed, sensitivity, and on/off ratio. The cross-section of the lithium niobate waveguide employed in this architecture is shown in Figure 4.4.1(b). It consists of a rib waveguide of width w_{wg} and thickness t_{wg}, fully embedded in SiO_2 [35]. A thickness t_{wg} = 180 nm is chosen to simultaneously achieve low propagation losses, fast temporal response, and a pronounced EO effect under applied electric fields. Thin-film $LiNbO_3$ on insulator (LNOI) devices further enhance the refractive index contrast by depositing a thin LN layer, only a few hundred nanometers thick, onto a SiO_2 substrate. Several bonding techniques have been developed for integrating TFLN with silicon at room temperature, including modified surface-activated bonding and ion-implantation combined with wafer bonding [31]. These approaches preserve the performance of bulk LN while enabling higher index contrast, thereby supporting dense integration, scalability of optical functionalities, tighter waveguide confinement, and reduced bend radii, perfectly suited for the intended application.

Each building block composing the FFT processor has been carefully designed to fulfil the design constraints, starting from the MUX-DeMUX.

After sampling and upconversion, SAR echo signals must be properly spaced to ensure accurate FFT processing. To achieve the target wavelength spacing of 2.4 pm and a total of 256 samples, it has been designed a two-stage cascaded

demultiplexer (De-MUX). The first stage consists of a 1×4 (1×2^2) AWG, while the second stage is composed of four parallel 1×64 (1×2^6) AWGs, yielding 256 distinct samples (see Figure 4.4.3(a)). In this configuration, the first AWG (AWG1), centered at 1549.6928 nm, separates the 2^8 input samples spaced by 300 MHz (corresponding to 256 wavelengths spaced 2.4 pm apart) into four macro-output channels with 153.6 pm spacing (64 × 2.4 pm). Each of these outputs is then routed to the second-stage AWGs, centered at 1549.624 nm, 1549.6156 nm, 1549.7692 nm, and 1549.9228 nm, respectively. These AWGs further divide the macro-channels into 64 single-mode outputs, thus providing the required 256 samples, which are then ready for weighting by phase shifters.

A crucial parameter for FFT processing is the insertion loss non-uniformity (ILu), since all channels must exhibit identical attenuation. Otherwise, uneven channel amplitudes would introduce undesired pre-weighting before the phase shifters, compromising FFT accuracy. ILu depends on AWG design parameters (waveguide pitch, star coupler radii, grating order, etc.), material properties, and channel spacing [38]. However, reducing ILu typically increases overall insertion loss (IL) and device footprint [39], making a careful trade-off necessary. For the design, an ILu of approximately 1 dB and a maximum crosstalk of –25 dB are targeted. The AWGs were optimized using recursive Beam Propagation Method (BPM) simulations to minimize ILu and maximize extinction ratio. Further explanations about the method are provided in Appendix B. Optical performance is strongly influenced by structural parameters such as waveguide spacing, taper geometry (width and length), and the number of arrayed waveguides. ILu, defined as the difference between the insertion loss of central and edge channels, can be expressed as [38]

$$IL_u \approx 13.65\left(\frac{(N_{ch}-1)\omega_e R_o m n_g \Delta\lambda}{R_i \lambda_o n_c D_o}\right)^2 \tag{13}$$

where N_{ch} is the number of channels, ω_e the effective mode field width, R_o the grating circle radius, m the grating order, n_g the group index, $\Delta\lambda$ the channel spacing, R_i the Rowland circle radius, λ_0 the central wavelength, n_c the core refractive index, and D_o the output waveguide pitch (see Figure 4.4.2).

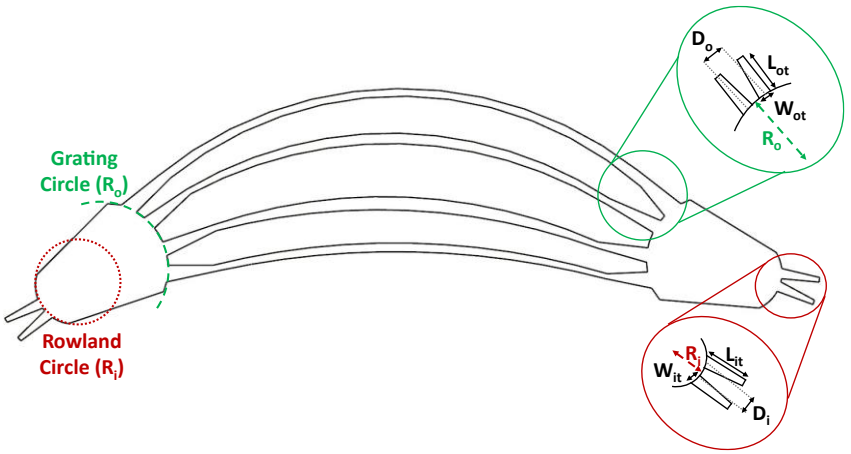

Figure 4.4.2 AWG structure representation with highlighted design parameters [31].

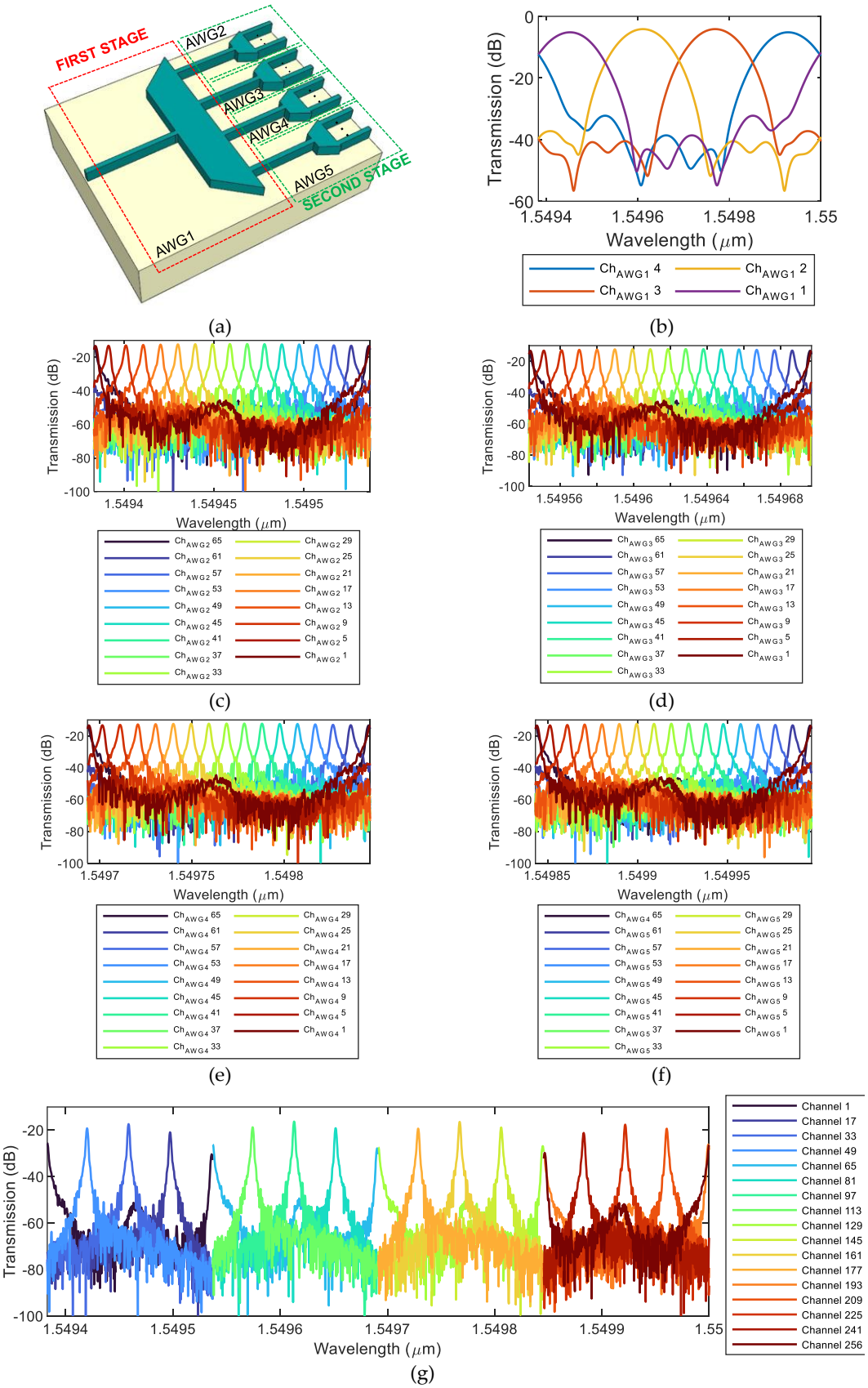

Figure 4.4.3 (a) De-MUX architecture. The red dotted box contains the first stage (1x4 AWG), in the green dotted box is represented the second stage consisting of four parallel 1x64 AWGs. (b) First stage transmission spectrum (AWG1) (c-f) Second stage transmission spectra (AWGi, i = 2…5). (g) Overall De-MUX output spectrum obtained cascading first and second stage [31].

In this framework, N_{ch} and $\Delta\lambda$ were fixed by the application requirements, while ω_e is determined via simulation, and m set by the AWG phase-matching condition. The tunable parameters are D_o and the R_o/R_i ratio. Additional optimization included adjusting the star coupler input (W_{it}) and output (W_{ot}) taper waveguide widths to improve diffraction efficiency, which is generally higher at central channels than at edges and thus a key contributor to ILu [38]. Increasing W_{it} and/or W_{ot} reduces ILu, though it requires tapered transitions to maintain mode matching, introducing further constraints on taper length. Finally, increasing the number of arrayed waveguides M significantly improves diffraction efficiency and reduces ILu, since more arrayed waveguides capture and guide diffracted light.

Based on the AWG design equations [40] and Eq. (12), recursive BPM simulations have been carried out. The transmission spectra of the optimized AWGs are shown in Figure 4.4.3(b–f), with the corresponding geometrical parameters summarized in Table 4.4.1. Both input and output waveguide widths are set to 5 μm to reduce crosstalk. In wider waveguides, the optical mode is more confined within the central region, while the modal tails are suppressed, thereby minimizing power leakage and inter-channel crosstalk. Figure 4.4.3(b) reports the spectrum of AWG1, which exhibits a minimum insertion loss (IL) of 4.15 dB, an insertion loss non-uniformity (ILu) of 1.12 dB, and a minimum crosstalk level of –28.36 dB. It is also evident that the free spectral range (FSR) of AWG1 exceeds the operational wavelength window, as spectral replicas appear only at the edges of the considered range. Figure 4.4.3(c–f) show the spectra of AWG2–AWG5, which achieve maximum IL, ILu, and crosstalk values of 12.11 dB, 1.3 dB, and –25 dB, respectively. When cascading the two AWG stages (see Figure 4.4.3(g)), the overall system performance results in a maximum insertion loss of 16 dB and a total crosstalk of –25.54 dB. Owing to the very low ILu, the output spectrum of the cascaded De-MUX shows only minor amplitude modulation, ensuring negligible impact on the sample weighting required for FFT computation. The modular two-stage configuration is adopted to achieve the extremely narrow channel spacing of $\Delta\lambda$ = 2.4 pm. In this scheme, a broadband device (AWG1) is used as the first stage, followed by narrower-band devices (AWGi, i = 2, …, 5) in the secondary stage. Realizing such fine wavelength resolution with a single AWG would be highly challenging, as it would require an impractically large footprint and a prohibitive number of arrayed waveguides. In fact, the realization of dense AWG channel spacings remains an open technical challenge [41]. Both the cascading of multiple AWGs and the reduction of $\Delta\lambda$ in a single device—increasing its resolution—lead to a significant enlargement of the device footprint and constrain the overall usable wafer area [41].

Table 4.4.1 AWGs geometrical parameters.

	D_i (μm)	D_o (μm)	W_{it} (μm)	W_{ot} (μm)	L_{it} (μm)	L_{ot} (μm)	R_i/R_o	M
AWG1	7	7	6	6	20	20	1.5	12
AWG2	12.3	10	10.3	5	50	10	1.5	192
AWG3	12.3	10	10.3	5	50	10	1.5	192
AWG4	12.3	10	10.3	5	50	10	1.5	192
AWG5	12.3	10	10.3	5	50	10	1.5	192

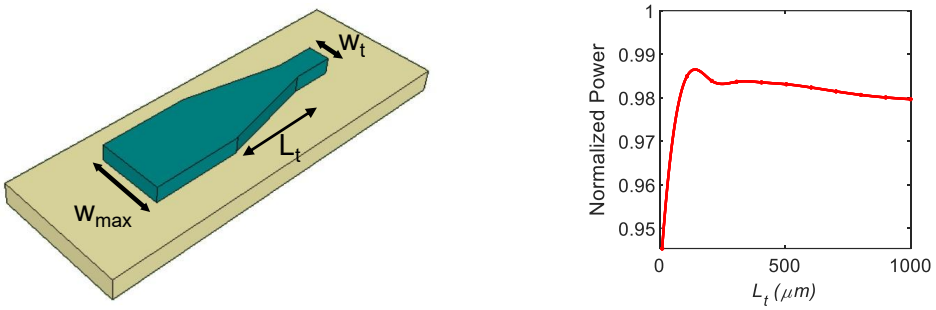

(a) (b)

Figure 4.4.4 SSC design (a) Sketch of the SSC. (b) Normalized power behavior vs device length. (W_{max}: AWG waveguide width, L_t: taper length, w_t: EO waveguide width) [31].

As regard the phase shifters, a waveguide width of 2 μm is selected in order to guarantee single-mode operation while achieving suitable driving voltage, response time, and loss levels, in line with experimental demonstrations reported in literature [42]. The transition from the 5 μm-wide AWG waveguides to the 2 μm-wide EO tuning section requires the use of tapered Spot Size Converters (SSCs), which can be seamlessly integrated with Lithium Niobate on Insulator (LNOI) modulators (see Figure 4.4.4(a)). To optimize the taper design, Beam Propagation Method (BPM) parametric simulations have been carried out to determine the SSC length that maximizes transmission while maintaining a Gaussian field profile and assuming a single-mode waveguide of width w_{max} as the source. The calculations are performed considering the fundamental transverse electric (TE) mode [43].

Figure 4.4.4(b) shows the normalized output power as a function of SSC length. To isolate the effect of taper propagation, without accounting for other potential sources of loss, the output power is normalized with respect to the SSC input power. The optimized design achieved a maximum normalized output power of 0.988 at an SSC length of L_t = 140 μm. For longer tapers, the output power gradually decreases due to accumulated propagation losses. To rate this solution, the end-surface coupling efficiency, abrupt loss, and transmission efficiency are compared to the state-of-the-art solutions reported in literature. This results surpass previously reported values, which reached 0.975 (0.963) for TE (TM) polarization at a wavelength of 1550 nm [44]. Although the introduction of a converter inevitably increases losses, careful taper design allows these to be minimized. Particularly, the total loss penalty was limited to only 1.2%.

To perform the FFT, the critical elements are the phase shifters, which introduce tunable delays to appropriately weight the wavelength samples and thereby extract the FFT spectral components. The weighting matrix $W_{256\times256}$ is defined by the relation $w_N = e^{-j2\pi/N}$.

An electro-optical tuning approach has been adopted, as it combines fast temporal response with a wide dynamic range, exploiting the large electro-optic coefficient of x-cut $LiNbO_3$ (r_{zz} = 31.2 pm/V [45]) while preserving a low driving voltage. The x-cut configuration has been selected rather than the z-cut one to employ the TE mode, commonly used in telecommunications, for RF signal coupling, ensuring that the strongest electro-optical tensor component (r_{zz}) is always exploited [46]. In addition, x-cut $LiNbO_3$ exhibits lower absorption losses and allows for a thinner buffer layer,

further reducing the driving voltage [47]. The phase shifter structure is illustrated in Figure 4.4.5(a), showing the crystal orientation, electrode positioning, applied voltages, and the relevant geometric parameters.

To achieve significant refractive index modulation with minimal propagation losses, a gap g = 2 μm has been selected. Optimization of the lateral geometric parameter g/Γ is essential for minimizing the figure of merit ($FoM = V_\pi \cdot L$), where V_π, L, and Γ represent the half-wave voltage, device length, and overlap parameter, respectively [45]. The tuner length has been set to L = 4.1 mm, ensuring a full 2π phase shift on each path when no external driving voltage is applied.

To guarantee velocity matching between the RF and optical modes, FEM simulations were carried out, demonstrating that matching is achieved at a frequency of 350 MHz (see Figure 4.4.5(b–c)). Specifically, Figure 4.4.5(b) shows the RF field distribution at 350 MHz for the maximum applied voltage (n_{rf} = 1.8491), while Figure 4.4.5(c) depicts the optical mode distribution (n_{eff} =1.849 at 1550 nm).

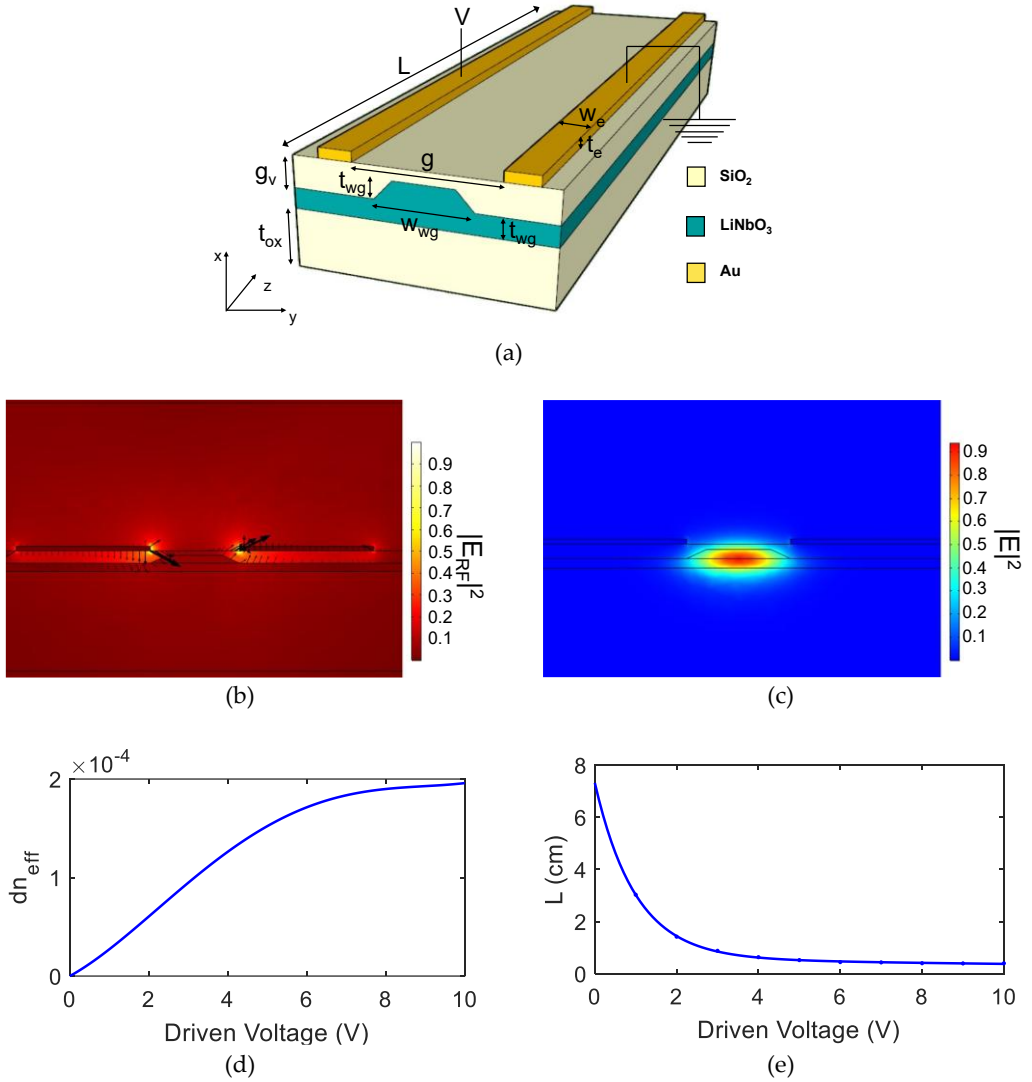

Figure 4.4.5 EO tuners design (a) Sketch of the tuner. (b) Normalized RF field line distribution at maximum voltage (c) Normalized electric field TE mode distribution (@ 1550 nm) (d) Effective refractive index change δn_{eff} and (e) Modulator length L as a function of the driving voltage to achieve a π-shift (V_π) [31]

The EO phase shifters have been designed such that the phase shift satisfies the condition $e^{-j\frac{2\pi}{\lambda}n_{eff}L} = w_N^{kn}$, k = 0, …, N-1. The required change in the real part of the effective refractive index, Δn_{eff} , must range between 1.44 × 10^{-6} to 3.6905 · 10^{-4} to generate the corresponding weighting coefficients. Using Ansys Lumerical Charge, which solves Poisson's equation for the electrostatic potential, together with the Finite Element EigenMode (FEEM) solver, the minimum and maximum voltages required to obtain these coefficients have been determined. As shown in Figure 4.4.5(d), the applied voltage must range from approximately 0.10 V to 7.07 V. Furthermore, Figure 4.4.5(e) illustrates the relationship between device length *L* and V_π, where V_π is the half-wave voltage associated with a π-phase shift, used to evaluate the EO modulator *FoM*. The resulting *FoM* reaches a maximum of 3.1 V · cm, which is competitive with state-of-the-art $LiNbO_3$ modulators (2.2 V · cm [48]).
The designed values of the modulator geometrical parameters are reported in Table 4.4.2. The rib waveguide width (w_{wg}) has been set to 2 μm to guarantee single-mode propagation, while a sidewall slant of 25°, consistent with fabrication constraints, has been assumed [49]. The waveguide thickness (t_{wg}) has been fixed at 180 nm to maintain the low propagation losses characteristic of TFLN (2.8 dB/m at 1550 nm [50]). The buffer layer thickness (g_v), electrode width (w_e) and thickness (t_e), as well as the electrode separation (g), have been optimized through recursive simulations to achieve the required effective index variation of the optical mode.
Two-dimensional finite element method (FEM) multiphysics simulations are employed to estimate the overlap coefficient *Γ*, defined as $\Gamma=\frac{\mathfrak{E}}{V}\iint E\,|A|^2 dA$, where *E* is the electric field generated by the electrodes (Figure 4.4.5(b)), and *A* represents the normalized distribution of the optical mode (Figure 4.4.5(c)). The simulations yielded an overlap coefficient Γ = 1. Further information on FEM Multiphysics simulations is introduced in Appendix A.
In the traveling-wave model of the phase shifter, since the electrode length is comparable to the RF wavelength, the required modulation voltage scales inversely with the device length, as does the bandwidth (*BW*), provided that electrode resistance is negligible. The figure of merit used to estimate the temporal tuning response is *V*/*BW*, expressed as

$$\left(\frac{V}{BW}\right) = \frac{\pi}{2c}\frac{\left(n_{rf}\left[1-{}^{n_{eff}}/_{n_{rf}}\right]\right)}{n_e^3\, r_{33}}\, p\lambda\, \frac{g}{\Gamma} \tag{14}$$

where n_{eff} and n_{rf} denote the optical and microwave effective refractive indices, respectively, p is the phase-matching parameter, n_e is the extraordinary refractive index of $LiNbO_3$, and r_{33} its electro-optic tensor coefficient. By substituting the previously calculated parameters, the modulation time response (*1*/*BW*) is found to range from 13.81 ps (for 7.07 V) to 0.97 ns (for 0.101 V).

Table 4.4.2 Geometrical modulator parameters

w_{wg} (μm)	t_{wg} (nm)	g (μm)	t_{ox} (μm)	g_v (nm)	w_e (μm)	t_e (nm)	L (mm)
2	180	2	20	100	3	100	4.1

Based on the fabrication technologies reported in literature [35, 51-52], the dimensions of each device in the system have been selected accordingly. Indeed, the design of the arrayed waveguide gratings (AWGs), electro-optical phase shifters, and spot size converters are compliant to current technological constraints reported on thin film lithium niobate (TFLN) platform.

The FFT of the input signal has been evaluated by cascading the previously dimensioned functional building blocks and multiplying their corresponding transfer functions, while also accounting for component losses. In the signal path, each received waveform is first upconverted by the SSB modulator and then sampled through the EO-MZM. The resulting wavelength samples are separated by the de-MUX, individually weighted according to the coefficient matrix via EO phase shifters, and subsequently recombined by the MUX to reconstruct the complete FFT spectrum, shown in Figure 4.4.6. The analysis reveals overall system losses of approximately 12 dB at the carrier, accompanied by strong suppression of higher-order harmonics, which are significantly attenuated compared to the carrier. Importantly, because the insertion-loss non-uniformity (ILu) of the MUX/de-MUX stages has been kept minimal, the wavelength samples are not subject to amplitude modulation, thus preventing spurious harmonic generation. As a result, the obtained FFT spectrum appears nearly flat, following the spectral profile imposed by the cascaded AWGs, consistent with Figure 4.4.3(g).

The system's overall performance is summarized in Table 4.4.3. Each building block demonstrates results that are in line with, or comparable to, the current state of the art. Furthermore, the proposed integrated system meets the SAR FFT design requirements in terms of sampling and carrier frequency, number of bits while offering the additional advantage of sub-nanosecond real-time response.

Looking ahead, future developments may include the realization of both the SSB and MZM modulators in $LiNbO_3$, enabling the monolithic integration of the OFFT onto a single chip. Another promising direction involves the implementation of photonic memories based on phase-change materials (PCMs), which could store FFT samples representing the signal spectrum [53].

Table 4.4.3 OFFT designed performance.

Sample Spacing	Maximum Voltage	Tuners Lenght	BIT	$(\Delta n)_{MAX}$	Time response	IL_{max}
300 MHz (2.4 pm)	7.1 V	4.1 mm	8	$3.6905 \cdot 10^{-4}$	0.98 ns	12 dB

This paper presents a photonic approach to the design of an innovative reconfigurable all-optical SAR payload, aligned with the objectives of the NewSpace Economy. To achieve payload miniaturization while maintaining high performance, it has been developed a novel photonic tunable architecture for on-board data processing in the Ka-band.

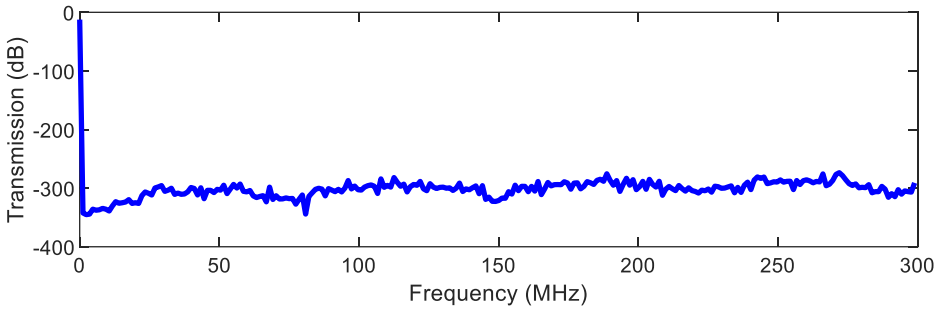

Figure 4.4.6 8-bit photonic FFT spectrum of a DC signal [31].

4.5 Conclusions

The proposed structure enables a straightforward implementation of the Optical Fast Fourier Transform (OFFT) within a compact and integrated design, thereby overcoming the intrinsic limitations of conventional solutions based on cascaded MZI networks, dispersive elements, or spectrometer architectures. By reducing the number of required components and allowing the direct real-time computation of FFT samples, this approach represents a significant advancement over existing methods. In particular, the 2^N frequency-domain samples are generated through 2^N tunable and reconfigurable waveguides, replacing the much larger $2^{N\times N}$ matrix typical of electronic DSP-based approaches.

Compared to conventional RF electronic solutions, which rely on parallel Digital Signal Processors (DSPs) and analog-to-digital conversion, the proposed photonic structure offers distinct advantages in terms of processing speed, reconfigurability, and efficiency. While electronics are constrained by sampling rates and conversion stages, photonic processing is limited only by photon propagation time, in the order of nanoseconds across the photonic chip, thereby enabling true real-time computation. This architecture therefore meets the stringent requirements of Copernicus, supporting 256 channels spaced 300 MHz apart in the Ka-band. Leveraging the low propagation losses of TFLN, it is possible to achieve a maximum insertion loss of 12 dB, a driving voltage of up to 7 V, a maximum time delay of 0.98 ns, and a phase shifter length of 4.1 mm, paving the way toward the realization of fully optical SAR payloads.

By adopting such an architecture, it becomes possible to implement fully integrated photonic processing of SAR echoes directly on board Copernicus Sentinel-1 and future missions. Photonics provides clear advantages over electronics in terms of speed, latency, SWaP, and resilience to electromagnetic interference (EMI). A fully photonic processor would further allow real-time on-board data evaluation, thus eliminating the need to transmit massive volumes of raw data to ground stations, saving both bandwidth and transmission power. Looking forward, this capability could support the development of distributed SAR constellations, where compact and lightweight payloads are essential for deployment on CubeSats.

Finally, the modularity of the deMUX/MUX stages, combined with the adopted sampling technique and the tunability of the phase shifters, ensures wide operational flexibility. The system can be adapted to different bandwidths and carrier frequencies and scaled according to the number of bits required for

processing, offering a versatile and future-proof platform for next-generation photonic SAR payloads.

References

[1]. G. Furano, A. Menicucci, A. "Roadmap for on-board processing and data handling systems in space," in *Dependable Multicore Architectures at Nanoscale* (). Cham: Springer International Publishing, 2017, pp. 253-281.

[2]. G. Brunetti, G. Campiti, M. Tagliente, C. Ciminelli, "Cots devices for space missions in leo," *IEEE Access*, vol. 12, pp. 76478-76514, 2024, doi: 10.1109/ACCESS.2024.3405373.

[3]. J. Gaisler, "Concurrent error-detection and modular fault-tolerance in a 32-bit processing core for embedded space flight applications," in *Proceedings of IEEE 24th International Symposium on Fault-Tolerant Computing, Austin, TX, USA, 1994*, doi: 10.1109/FTCS.1994.315650

[4]. ESA, "LEON: the space chip that Europe built", Accessed September 04, 2025. [Online]. Available: https://www.esa.int/Enabling_Support/Space_Engineering_Technology/LEON_the_space_chip_that_Europe_built

[5]. D. Pérez, I. Gasulla, L. Crudgington, D. J. Thomson, A. Z. Khokhar, K. Li, W. Cao, G. Z. Mashanovich, J. Capmany, "Multipurpose silicon photonics signal processor core," *Nature communications*, vol. 8, no. 1, p. 636, 2017, doi: https://doi.org/10.1038/s41467-017-01529-w.

[6]. A. Annoni, E. Guglielmi, M. Carminati, G. Ferrari, M. Sampietro, D. Miller, A. Melloni, F. Morichetti, "Unscrambling light—automatically undoing strong mixing between modes," *Light: Science & Applications*, vol. 6, no. 12, pp. e17110-e17110, 2017, doi: https://doi.org/10.1038/lsa.2017.110.

[7]. A. Ribeiro, A. Ruocco, L. Vanacker, W. Bogaerts, "Demonstration of a 4× 4-port universal linear circuit," *Optica*, vol. 3, no. 12, pp. 1348-1357, doi: https://doi.org/10.1364/OPTICA.3.001348.

[8]. N. C. Harris, G. R. Steinbrecher, M. Prabhu, Y. Lahini, J. Mower, D. Bunandar, C. Chen, F. N. C. Wong, T. Baehr-Jones, M. Hochberg, S. Lloyd, D. Englund, "Quantum transport simulations in a programmable nanophotonic processor," *Nature Photonics*, vol. 11, no. 7, pp. 447-452, 2017, doi: https://doi.org/10.1038/nphoton.2017.95.

[9]. D. Pérez, I. Gasulla, J. Capmany, "Programmable multifunctional integrated nanophotonics," *Nanophotonics*, vol. 7, no. 8, pp. 1351-1371, 2018, doi: https://doi.org/10.1515/nanoph-2018-0051.

[10]. W. Bogaerts, D. Pérez, J. Capmany, D. Miller, J. Poon, D. Englund, F. Morrichetti, A. Melloni, "Programmable photonic circuits," *Nature*, vol. 586, no. 7828, pp. 207-216, 2020, doi: https://doi.org/10.1038/s41586-020-2764-0.

[11]. D. Pérez-López, L. Torrijos-Morán, "Large-scale photonic processors and their applications," *npj Nanophotonics*, vol. 2, no. 1, p. 32, doi: https://doi.org/10.1038/s44310-025-00075-4

[12]. D. Pérez-López, A. Gutierrez, D. Sánchez, A. López-Hernández, M. Gutierrez, E. Sánchez-Gomáriz, J. Fernández, A. Cruz, A. Quirós, Z. Xie, J. Benitez, N. Bekesi, A. Santomé, D. Pérez-Galacho, P. DasMahapatra, A. Macho, J. Capmany, "General-purpose programmable photonic processor for advanced radiofrequency applications," *Nature Communications*, vol. 15, no. 1, p. 1563, doi: https://doi.org/10.1038/s41467-024-45888-7.

[13]. J. Capmany, and D. Pérez, *Programmable integrated photonics*, Oxford, United Kindom, Oxford University Press, 2020.

[14]. A. di Toma, G. Brunetti, N. Saha, C. Ciminelli, "Fully reconfigurable photonic filter for flexible payloads," *Applied Sciences*, vol. 14, no. 2, p. 488, 2024, doi: https://doi.org/10.3390/app14020488.

[15]. C. Ciminelli, F. Dell'Olio, G. Brunetti; D. Conteduca; M. N. Armenise, "New microwave photonic filter based on a ring resonator including a photonic crystal structure," in *19th International Conference on Transparent Optical Networks (ICTON),Girona, Spain, 2017*, pp. 1-4, doi*: 10.1109/ICTON.2017.8024931*.

[16]. G. Brunetti, M. N. Armenise, C. Ciminelli, "Chip-scaled Ka-band photonic linearly chirped microwave waveform generator," *Frontiers in Physics*, vol. 10, p. 785650, 2022, doi: https://doi.org/10.3389/fphy.2022.785650.

[17]. C. Ciminelli, N. Saha, G. Brunetti, A. di Toma, M. N. Armenise, "Reconfigurable Optical Beam Forming Network for Telecom Payloads," in *2024 24th International Conference on Transparent Optical Networks (ICTON), Bari, Italy, July 14-18, 2024*, pp. 1-4, doi: 10.1109/ICTON62926.2024.10647596.

[18]. A. di Toma, G. Brunetti, N. Saha, C. Ciminelli, "Fully reconfigurable photonic filter for flexible payloads," *Applied Sciences*, vol. 14, no. 2, p. 488, 2024, doi: https://doi.org/10.3390/app14020488.

[19]. D. Romano, V. Mele, M. Lapegna, "The challenge of onboard SAR processing: A GPU opportunity," in *Computational Science ICCS 2020: 20th International Conference, Amsterdam, The Netherlands, 2020*, pp. 46-59, doi: https://doi.org/10.1007/978-3-030-50420-5_4.

[20]. X. Jing, Y. Guo, "Design of spotlight SAR imaging system based on multicore DSP," in *6th Asia-Pacific Conference on Synthetic Aperture Radar (APSAR), Xiamen, China, 2019*, pp. 1-4, doi: 10.1109/APSAR46974.2019.9048326.

[21]. M. N. Armenise, E. Pansini, A. Fioretti, "A novel guided-wave correlator for real-time synthetic aperture radar data processing," *Integrated Optical Circuit Engineering VI*, vol. 993, pp. 225-233, 1988, doi: https://doi.org/10.1117/12.960093.

[22]. M. N. Armenise, V. M. Passaro, "Novel guided-wave electro-optic processor for synthetic aperture radar imaging," *Optical Engineering*, vol. 33, no.6, pp. 1854-1862, 1994, doi: https://doi.org/10.1117/12.170732.

[23]. R. G. Rozier, F. E. Kiamilev, A. V. Krishnamoorthy, "Design of a parallel photonic FFT processor," in *Proceedings of Massively Parallel Processing Using Optical Interconnections*, *Maui, HI, USA, 1996*, pp. 36-43, doi: 10.1109/MPPOI.1996.559034.

[24]. J. K. Ong, C. C. Ooi, T. Y. Ang, S. T. Lim, and C. E. Png, "Photonic convolutional neural networks using integrated diffractive optics," *IEEE Journal of selected topics in quantum electronics*, vol. 26, no. 5, pp. 1-8, 2020, doi: 10.1109/JSTQE.2020.2982990.

[25]. J. Li, S. Fu, X. Xie, M. Xiang, Y. Dai, F. Yin, Y. Qin, "Low-latency short-time Fourier Transform of microwave photonics processing," *Journal of Lightwave Technology*, vol. 41, no. 19, pp. 6149- 6156, 2023, doi: 10.1109/JLT.2023.3279261.

[26]. D. M. Kita, C. Ríos, and J. Hu, "Performance Optimization Strategies for Nanophotonic Digital Fourier Transform Spectrometers," in Fourier Transform Spectroscopy (FTS), San Jose, U. S. A., 2019, pp. FTu4B-5.

[27]. D. Hillerkuss, M. Winter, M. Teschke, A. Marculescu, J. Li, G. Sigurdsson, K. Worms, S. Ben Ezra, N. Narkiss, W. Freudeand, and J. Leuthold, "Simple all-optical FFT scheme enabling Tbit/s real-time signal processing," Optics Express, vol. 18, no. 9, pp. 9324-9340, 2010.

[28]. J. K. George, H. Nejadriahi, and V. J. Sorger, "Towards on-chip optical ffts for convolutional neural networks," in 2017 IEEE Inter. Conf. on Rebooting Comp. (ICRC), Washington, DC, USA, 2017, pp. 1-4).

[29]. M. Ahmed, Y. Al-Hadeethi, A. Bakry, H. Dalir, and V. J. Sorger, "Integrated photonic FFT for photonic tensor operations towards efficient and high-speed neural networks," Nanophotonics, vol. 9, no. 13, pp. 4097-4108, 2020, doi: https://doi.org/10.1515/nanoph-2020-0055.

[30]. T. Tatoli, D. Conteduca, F. Dell'Olio, C. Ciminelli, M. N. Armenise, "Graphene-based fine-tunable optical delay line for optical beamforming in phased-array antennas," Applied Optics, vol. 55, no. 16, pp. 4342-4349, 2016, doi: https://doi.org/10.1364/AO.55.004342.

[31]. A. di Toma, G. Brunetti, M. N. Armenise, C. Ciminelli, "LiNbO_3-Based Photonic FFT Processor: An Enabling Technology for SAR On-Board Processing," *Journal of Lightwave Technology*, vol. 43, no. 2, pp. 912-921, 2025, doi: 10.1109/JLT.2024.3453670.

[32]. eoPortal, "COSMO-SkyMed," Accessed September 08, 2025. [Online]. Available: https://directory.eoportal.org/web/eoportal/satellite-missions/cmissions/cosmo-skymed

[33]. D. Geudtner, R. Torres, "Sentinel-1 System Overview and Performance," in *2012 IEEE International Geoscience and Remote Sensing Symposium, Munich, Germany, 2012*, pp. 1719-1721, doi: 10.1109/IGARSS.2012.6351191.

[34]. M. Zhang, C. Wang, R. Cheng, A. Shams-Ansari, M. Lončar, "Monolithic ultra-high-Q lithium niobate microring resonator," *Optica*, vol. 4, no. 12, pp. 1536-1537, 2017, doi: https://doi.org/10.1364/OPTICA.4.001536.

[35]. W. Ke, Y. Lin, M. He, M. Xu, J. Zhang, Z. Lin, S. Yu, and X. Cai, "Digitally tunable optical delay line based on thin-film lithium niobate featuring high switching speed and low optical

loss," *Photonics Research*, vol. 10, no. 11, pp. 2575-2583, 2022, doi: https://doi.org/10.1364/PRJ.471534

[36]. Z. Lin, Y. Lin, H. Li, M. Xu, M. He, W. Ke, H. Tan, Y. Han, Z. Li, D. Wang, X. S. Yao, S. Fu, S. Yu and X. Cai, "High-performance polarization management devices based on thin-film lithium niobate," *Light: Science & Applications*, vol. 11, no. 1, pp. 93, 2022, doi: https://doi.org/10.1038/s41377-022-00779-8.

[37]. M. Li, J. Ling, Y. He, U. A. Javid, S. Xue, and Q. Lin, "Lithium niobate photonic-crystal electro-optic modulator," *Nature Communications*, vol. 11, no. 1, pp. 4123, 2020, doi: https://doi.org/10.1038/s41467-020-17950-7.

[38]. Y. Zheng, X. Wu, L. Jiang, Y. Wu, J. A. Duan, "Design of 4-channel AWG multiplexer/demultiplexer for CWDM system," *Optik*, vol. 201, pp. 163513, 2020, doi: https://doi.org/10.1016/j.ijleo.2019.163513.

[39]. Y. Zheng, Y. Wu, H. Sun, H. He, and Z. Liu, "Optical performances analysis and structure parameters optimization design of dense arrayed waveguide grating," *Results in Optics*, vol. 2, pp. 100049, 2021, doi: https://doi.org/10.1016/j.rio.2020.100049.

[40]. M. Amersfoort, "Arrayed waveguide grating," C2V, Enschede, Netherlands, Application note A1998003, 1998.

[41]. N. Jovanovic, P. Gatkine, N. Anugu, R. Amezcua-Correa, R.B. Thakur, C. Beichman, C. F. Bender, J.-P. Berger, A. Bigioli, J. Bland-Hawthorn, "2023 Astrophotonics Roadmap: pathways to realizing multi-functional integrated astrophotonic instruments," *Journal of Physics: Photonics*, vol. 5, no. 4, pp. 042501, 2023, doi: 10.1088/2515-7647/ace869.

[42]. J.-X. Zhou, R.-H. Gao, J. Lin, M. Wang, W. Chu, W.-B. Li, D.-F. Yin, L. Deng, Z.-W. Fang, J.-H. Zhang, "Electro-optically switchable optical true delay lines of meter-scale lengths fabricated on lithium niobate on insulator using photolithography assisted chemo-mechanical etching," *Chinese Physics Letters*, vol. 37, no. 8, pp. 084201, 2020, doi: 10.1088/0256-307X/37/8/084201.

[43]. G. Brunetti, R. Heuvink, E. Schreuder, M. N. Armenise, C. Ciminelli, "Silicon Nitride Spot Size Converter with Very Low-Loss over the C-Band," *IEEE Photonics Technology Letters*, vol. 35, no. 22, pp. 1215- 1218, 2023, doi: 10.1109/LPT.2023.3311914.

[44]. Y. Liu, W. Chen, Y. Zhang, K. Cao, Y. Liu, M. Li, N. Zhu, "High-efficiency spot-size converter for thin-film lithium niobate modulators," *in 2022 Appl. Opt. and Phot. China: Optoele. and Nanophot. (AOPC 2022), online, 2023*, pp. 134-139.

[45]. H. Han, and B. Xiang, "Integrated electro-optic modulators in x-cut lithium niobate thin film," *Optik*, vol. 212, pp. 164691, 2020, doi: https://doi.org/10.1016/j.ijleo.2020.164691.

[46]. D. Janner, D. Tulli, M. García-Granda, M. Belmonte, and V. Pruneri, "Micro-structured integrated electro-optic LiNbO3 modulators," *Laser & Photonics Reviews*, vol. 3, no. 3, pp. 301-313, 2009, doi: https://doi.org/10.1002/lpor.200810073.

[47]. T. Gorman, and S. Haxha, "Full-Wave Comparison of Z-cut and X-cut Lithium Niobate (LiNbO3) Electrooptic Modulators Using Finite Element Method," in *World Cong. on Eng., London, UK, 2007*, pp. 459-464.

[48]. Rahim, A. Hermans, B. Wohlfeil, D. Petousi, B. Kuyken, D. Van Thourhout, and R. Baets, "Taking silicon photonics modulators to a higher performance level: state-of-the-art and a review of new technologies," *Advanced Photonics*, vol. 3, no. 2, pp. 024003-024003, 2021, doi: https://doi.org/10.1117/1.AP.3.2.024003.

[49]. J. Mercante, S. Shi, P. Yao, L. Xie, R. M. Weikle, D. W. Prather, "Thin film lithium niobate electro-optic modulator with terahertz operating bandwidth," *Optics Express*, vol. 26, no. 11, pp. 14810-14816, 2018, doi: https://doi.org/10.1364/OE.26.014810.

[50]. D. Zhu, L. Shao, M. Yu, R. Cheng, B. Desiatov, C. J. Xin, and M. Lončar, "Integrated photonics on thin-film lithium niobate," *Advances in Optics and Photonics*, vol. 13, no. 2, pp. 242-352, 2021, doi: https://doi.org/10.1364/AOP.411024.

[51]. J. Li, L. Wang, K. Li, Z. Li, C. Zhang, "Thin-Film Lithium Niobate (TFLN)-Based Multimode Interference Power Splitter for Multi-Band Operation," *Optics Communications*, vol. 132169, 2025, doi: https://doi.org/10.1016/j.optcom.2025.132169.

[52]. Y. Li, T. Lan, D. Yang, J. Bao, M. Xiang, F. Yang, Z. Wang, "High-performance Mach–Zehnder modulator based on thin-film lithium niobate with low voltage-length product," *ACS omega*, vol. 8, no. 10, pp. 9644-9651, 2023, doi: https://doi.org/10.1021/acsomega.3c00310.

[53]. W. Zhou, N. Farmakidis, J. Feldmann, X., Li, J. Tan, Y. He, C. D. Wright, W. H. P. Pernice, and H. Bhaskaran, "Phase-change materials for energy-efficient photonic memory and computing," *MRS Bulletin*, vol. 47, no. 5, pp. 502-510, 2022, doi: https://doi.org/10.1557/s43577-022-00358-7

Chapter 5

A full photonic SAR system

5.1 Introduction

The first civilian satellite mission carrying a Synthetic Aperture Radar (SAR) system was SeaSat, launched by NASA in 1978 with the primary objective of monitoring ocean dynamics. This pioneering mission highlighted the potential of SAR as a powerful remote sensing technology, capable of providing valuable data regardless of cloud coverage or solar illumination. In the early 1990s, SAR Interferometry (InSAR) emerged as a transformative technique, enabling the reconstruction of Earth's topography with unprecedented accuracy. Its ability to generate wide-area, high-resolution images (≤10 m) without requiring ground-based instruments significantly expanded the range of scientific and operational applications, from geophysics to natural disaster monitoring. Unlike optical payloads, SAR systems maintain the unique capability of imaging both day and night and under all weather conditions [1]. These advantages stimulated the development of increasingly sophisticated SAR configurations and architectures, extending their application across Earth Observation (EO) missions, planetary exploration, and security. Detailed information on SAR system, its building blocks, and its formulation are available in Appendix E.

In recent years, the proliferation of nanosatellites has triggered a seven-fold increase in EO missions, spurring a strong demand for SAR payload miniaturization [2]. However, system downsizing is generally achieved at the expense of performance metrics, such as spatial resolution, ground coverage, duty cycle, revisit time, and mission lifespan, owing to the intrinsic limits of electronic miniaturization. To address these constraints, the concept of monolithic SAR platforms has progressively evolved toward distributed constellations, such as COSMO-SkyMed or Capella SAR, in which multiple smaller satellites share the imaging workload. While this distributed paradigm alleviates single-platform limitations, it introduces new challenges, including stringent requirements on constellation control, inter-

satellite synchronization, coherent data acquisition, and processing to preserve imaging quality [3].

The demand for compact and efficient SAR payloads has directed increasing attention toward photonics, a technology with inherent advantages of miniaturization, robustness, and multifunctionality. Photonics has already established itself as a key enabling technology in diverse fields such as telecommunications, aerospace and defence, and life sciences. In the space sector, it has become a strategic area of research and development for the global aerospace market [4]. Photonics offers numerous advantages over conventional electronic solutions, including immunity to electromagnetic interference (EMI), low power consumption, high tolerance to vibration and radiation, and a reduced footprint. These features are particularly critical in satellite environments, where SWaP constraints dictate mission feasibility. For these reasons, research efforts dedicated to the integration of photonic subsystems into EO and telecommunications satellites are rapidly accelerating [5].

Recent demonstrations have confirmed that Photonic Integrated Circuits can yield reductions of more than 50% in mass and power consumption, enable up to 100-fold size reduction, and provide enhanced bandwidth and data rates. Additional benefits include cost-free redundancy, aperture independence, transparency to modulation format, versatility, and scalability [6]. In telecommunications payloads, the deployment of PICs has already proven capable of improving SNR performance, reducing propagation losses, lowering energy requirements, and delivering GHz-precision RF signal processing. Moreover, photonic implementations allow ultrafast and wideband data transfer, overtaking the capabilities of their electronic counterparts. Motivated by the remarkable improvements observed in inter- and intra-satellite communications, photonic technologies are now being extended into SAR subsystems, where they promise to overcome fundamental bottlenecks of electronic solutions and unlock new architectural possibilities.

A generic SAR payload architecture and its primary building blocks are illustrated in Figure 5.2.1. The transmission chain comprises a sequence of a microwave chirp generator, an in-phase/quadrature (I/Q) modulator, a frequency up-converter, amplifiers, a beamforming network, and Phased-Array Antennas (PAAs). The receive chain mirrors the transmission structure, except that the chirp generator is replaced by an analog-to-digital converter (ADC) to enable on-board pre-processing [7]. Specifically, the chirp generator produces a broadband linearly chirped microwave signal, which is subsequently modulated by the I/Q modulator and frequency up-converted. To avoid nonlinearities or saturation in electronic components, the signal is amplitude-limited and amplified before feeding the antenna array. Hundreds of transmit/receive (T/R) front-ends drive the PAAs, amplifying the RF signals and imparting phase shifts as determined by the beamforming network. During reception, incoming echoes are directionally weighted through the beamforming network, amplified, and down-converted to an intermediate frequency. The signal then undergoes I/Q demodulation, baseband filtering, and analog-to-digital conversion, preparing it for further electronic processing [8].

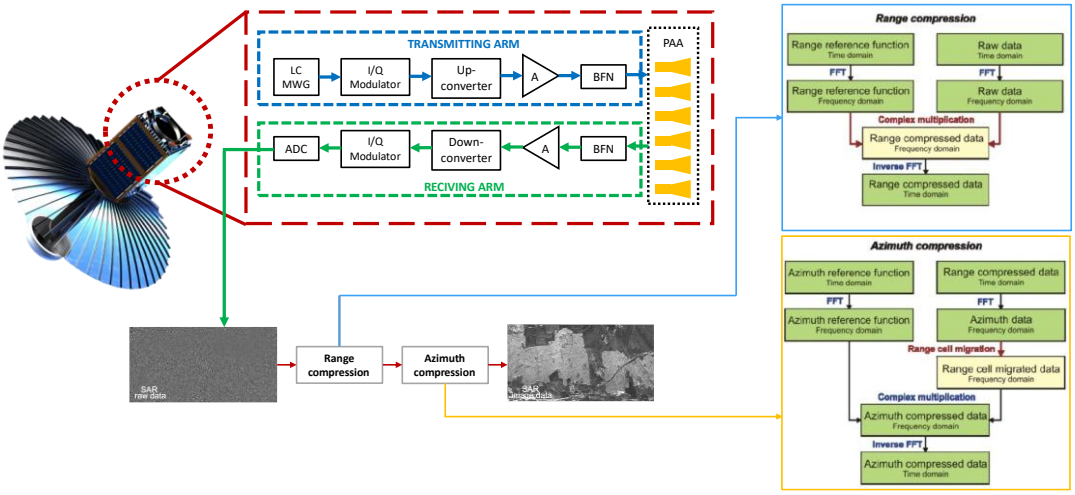

Figure 5.1.1 Building block scheme of SAR payload.

Despite its maturity, this conventional SAR architecture is fundamentally constrained by electronics, particularly in terms of processing speed, scalability, and power consumption. These limitations underscore the relevance of photonic solutions, which can replace or complement several of the above functional blocks, paving the way toward next-generation SAR payloads that meet the growing performance demands of NewSpace applications. Among the most promising ones are the transmitter section, where photonics enables the generation of highly stable and broadband chirped waveforms, the beamforming networks, which benefit from reconfigurability and low-loss true-time delay implementations, and the data processing units, where photonic FFT processors can offer real-time capability alleviating bottlenecks of conventional electronics.

The adoption of PIC-based subsystems is therefore not only an incremental improvement but a paradigm shift toward more efficient, compact, and versatile SAR payloads [9, 10].

In the specific case of chirped waveform generation, three primary approaches have been explored in the photonic domain: spectral shaping and frequency-to-time (SS-FTT) mapping, frequency and bandwidth multiplication, and Fourier-domain mode-locking of an optoelectronic oscillator (OEO) [11]. Among these, the SS-FTT mapping approach has been most extensively investigated, exploiting dispersion to convert the optical spectrum into a time-domain waveform. However, its effectiveness is constrained by the limited temporal width of the generated chirped waveform, which restricts the achievable time-bandwidth product (TBWP) and thus the radar's range resolution [12]. The second approach, based on frequency multiplication and bandwidth expansion through external modulation, enables the generation of chirped microwave waveforms with significantly larger TBWPs. This technique has been successfully applied in microwave photonic radars, demonstrating high-resolution imaging capabilities with compact system footprints [13]. The third and most promising approach leverages Fourier-domain mode-locked OEOs, which combine very large TBWP with remarkably low phase noise. This architecture stands out as an enabling solution for future high-performance photonic radars, given its ability to generate stable chirped signals at high frequencies with superior spectral purity [14].

The performance of the SAR system critically depends on the Phased-Array Antennas (PAAs), which must transmit and receive signals without beam squint while maintaining a broad steering angle. Photonic beamforming networks based on phase shifters, as demonstrated in [15], have shown the capability of providing more than 360° of phase tuning, with amplitude fluctuations as low as 2.5 dB, minimal signal distortion, steering errors around 3°, and sub-5 ns switching times. Despite these achievements, phase-shifter-based beam steering inherently suffers from frequency-dependent squinting, which makes it unsuitable for wideband SAR signals [16]. A widely recognized alternative is the adoption of true-time-delay (TTD) beamforming, which introduces progressive delays that are independent of frequency, thereby enabling inherently broadband operation. However, implementing TTD at millimeter-wave frequencies requires cascading multiple delay units, which increases both system footprint and insertion losses [17]. Consequently, novel photonic TTD solutions—based on dispersive media, microresonators, or integrated waveguide delays—are being actively investigated to overcome these limitations.

Another area of opportunity for photonic SAR development lies in data processing. By implementing an all-optical processing chain, radar echoes could be processed directly in the analog domain, thereby eliminating the need for bulky and power-hungry electronic A/D converters. In this framework, the recovery of the SAR image of the observed scene requires a two-dimensional fast Fourier transform (FFT). Several strategies have been proposed to directly realize it photonically. Free-space optical processors [18, 19], relying on components such as metalenses or mirror-based interferometric structures, implement the Fourier transform spatially but face limitations in terms of scaling, mechanical stability, and integration potential. Alternatively, integrated photonic approaches [20, 21]—typically based on cascaded Mach–Zehnder Interferometers—realize the Cooley–Tukey butterfly operations in the time domain. In these architectures, 2×2 MZIs perform addition and subtraction operations, while small path-length differences in selected branches implement the required phase shift. Despite their promise, both approaches suffer from limitations, free-space solutions are bulky and sensitive to misalignment, while integrated MZI-based FFT processors are hindered by high insertion losses, substantial power consumption, and scalability issues when the number of FFT samples increases.

Novel strategies to improve these building blocks are proposed, addressing limitations encountered in prior demonstrations while maintaining compatibility with real mission requirements. The design and performance assessment of these photonic building blocks have been carried out with the aim of meeting stringent SAR operational constraints, considering both the specifications reported in the literature and those demonstrated by existing payloads currently in orbit, such as COSMO-SkyMed and NovaSAR-S.

5.2 Linearly chirped waveform generator

Since microwave pulse compression is a fundamental requirement in the SAR payload transmission chain to ensure both high range resolution and wide swath coverage, it becomes essential to employ a linearly chirped microwave (LCMW)

waveform generator capable of delivering a TBWP on the order of 10^2 – 10^3. Achieving such performance is critical for modern spaceborne SAR systems, as the TBWP directly impacts the achievable resolution and imaging capabilities.

Among the various LCMWG architectures proposed in literature, one of the most promising designs is based on the combination of a frequency-tunable optoelectronic oscillator (OEO) and a recirculating phase modulation loop (RPML) [22], as illustrated in Figure 5.2.1. This hybrid architecture leverages the complementary benefits of both subsystems, enabling the generation of chirped signals with exceptionally high spectral purity, wide operational bandwidth, and compact physical footprint, key features for satellite payload integration under strict SWaP constraints.

The operating principle can be described as follows. The output of a tunable laser source is equally divided into two optical paths, one directed to the OEO and the other to the RPML. In the OEO branch, the optical signal is converted into a microwave tone with high spectral purity and frequency tunability, serving as a stable reference. Simultaneously, in the RPML branch, the optical signal is first intensity-modulated to produce a chirp-free optical pulse. This pulse then enters the recirculating loop, where it undergoes repeated phase modulation driven by a parabolic waveform. Each circulation within the loop progressively increases the chirp rate of the optical pulse, thereby enabling the generation of a highly linear chirped optical waveform. Finally, the outputs from the OEO and the RPML are coherently combined on a high-speed photodiode, where optical beating produces the desired LCMW waveform in the electrical domain [23].

The resulting signal exhibits both the large bandwidth associated with the RPML and the low phase noise ensured by the OEO. This dual-path strategy allows for scalable and tunable chirped waveform generation, well-suited for advanced SAR payloads requiring precise pulse compression with minimal distortion. A Mach–Zehnder Modulator (MZM), driven by a square-wave signal whose falling edge duration defines the target chirp, is used to generate the intensity-modulated version of the split optical signal that serves as the input to the RPML.

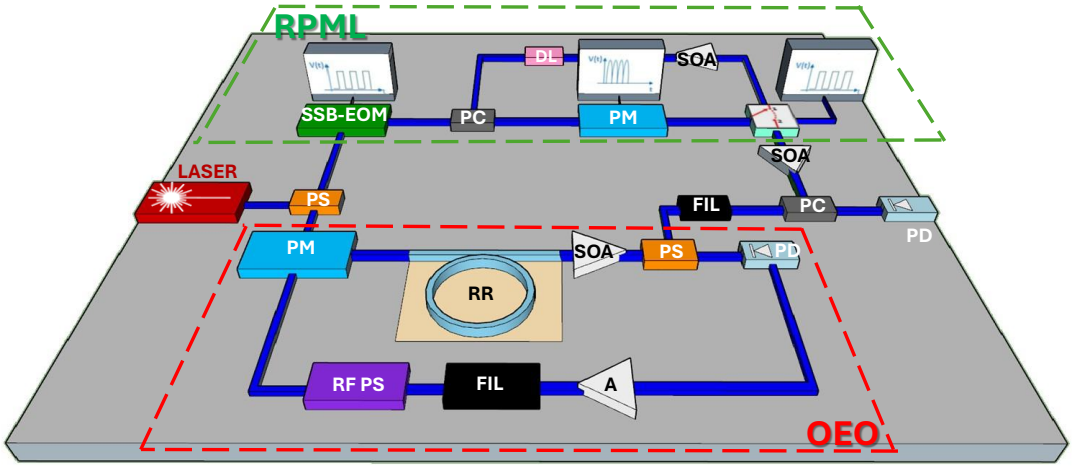

Figure 5.2.1 Sketch of LCMWG architecture (LD: Laser Diode, PS: Power Splitter. OEO: Opto-electronic oscillator – PM: Phase Modulator, RR: Ring Resonator, SOA: Semiconductor Optical Amplifier, PD: Photodiode, A: RF Amplifier, FIL: RF Filter, PS: RF Phase Shifter. RPML: Recirculating Phase Modulation Loop, PC: Power Combiner, DL: Delay Line)

Within the loop, a travelling-wave phase modulator, excited by a carefully engineered parabolic waveform, imprints the necessary frequency modulation onto the chirp-free pulse. The signal is subsequently amplified through a Semiconductor Optical Amplifier (SOA) and delayed using an optical delay line, before being recirculated. After performing N_r round trips, the modulated pulse is routed out of the loop once it surpasses the switch reference signal, which operates as a comparator. The number of round trips, the driving voltage, and the parabolic modulation profile must be precisely optimized to achieve a broad TBWP, while simultaneously minimizing excess delay and limiting power consumption.

On the OEO side, the optical signal derived from the power splitter undergoes phase modulation, filtering, and delay through a Fabry–Perot cavity, which in this study is implemented using a photonic crystal ring resonator. The output is then amplified by a SOA, after which the optical power is split, one branch is directed out of the loop, while the other is converted into an RF current by a high-speed photodiode (PD). This detected current is amplified, filtered, and phase-shifted in the microwave domain before driving the phase modulator at the loop input, thus establishing a positive feedback mechanism. The inclusion of the SOA compensates for round-trip losses, guaranteeing self-sustained oscillation and long-term stability.

The central element of the OEO is the high-Q ring resonator, which simultaneously provides selective filtering and delay. Achieving a very high Q-factor is critical, as it ensures both strong spectral purity and minimal phase noise. In this framework, a photonic crystal ring resonator has been chosen, since it has been demonstrated that incorporating photonic crystal structures into ring resonators yields Q-factors up to three orders of magnitude higher than those of conventional straight waveguides with similar geometries, thanks to the slow-light effect [24].

By combining the RPML and OEO sections, a compact and integrable LCMW generator has been designed, intended as a fundamental building block for photonic SAR payloads. The architecture has been dimensioned to provide a TBWP on the order of 10^2 – 10^3, thereby enabling high range resolution and ensuring a large RF spurious suppression ratio (RFSSR), while preserving output signal integrity. The RPML parameters, including the number of round trips (N_r) and the parabolic waveform with M segmented components used to drive the phase modulator, have been engineered to fulfil these requirements. To further enhance the RFSSR and improve signal purity, a Si_3N_4 photonic crystal ring resonator has been adopted in the OEO section, achieving an ultra-high Q-factor of 2×10^{10}, an extinction ratio of 8 dB, and a calculated phase noise of –100 dBc/Hz.

Under optimal conditions—central frequency of 40 GHz, V_{pp} = 1.1 V, M = 40, and N_r = 18 —the system can produce an exceptional TBWP of approximately 1078, with an ultra-large pulse compression ratio (PCR) of 814 and an RFSRR of about 11 dB.

Figure 5.2.2(a) and (b) are obtained by using the system-level simulator Optisystem. The autocorrelation function of the LCMW shows an ultra-large PCR of 814 and PSR = 6.79 dB. The TBWPs results compliant with the predicted ones according to [25]

$$TBWP = \frac{2\,M\,N\,V_{pp}}{V_\pi} \tag{15}$$

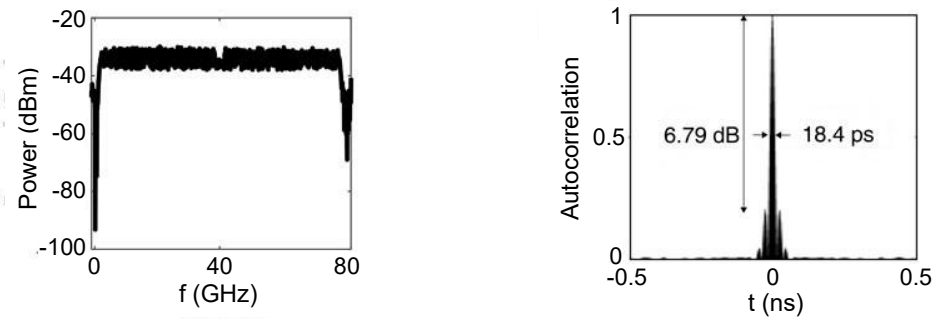

(a) (b)

Figure 5.2.2 LCMW generator (a) output spectrum and (b) autocorrelation function [25]

The overall generator has been conceived as compatible with heterogeneous integration on a silicon substrate in a system-in-package configuration, thereby overcoming the traditional limitations of bulky, discrete-component designs in terms of footprint, scalability, and integration [25]. The demonstrated performance highlights the potential of the proposed LCMW generator to serve as a next-generation enabling technology for advanced spaceborne SAR systems, combining compactness with high precision and spectral purity.

5.3 Beamforming network

Conventional SAR systems are inherently constrained by a trade-off between swath width and spatial resolution, as both parameters are fundamentally limited by antenna aperture dimensions. This restriction forces system designers to compromise between coverage and resolution, thus narrowing the achievable performance space [26]. To overcome these bottlenecks, novel SAR architectures have been explored, where the receiving antenna is subdivided into multiple sub-apertures, each connected to independent receiver channels. This partitioning strategy enables the adoption of beamforming networks, which can dynamically tailor the array response and provide a flexible path to bypassing the limitations of conventional monolithic antenna designs.

If N denotes the number of radiating elements along the elevation dimension, the classical beamforming network topology incorporates N tunable optical delay lines. These delay lines adjust the propagating beams phase shifts to steer the synthesized one toward a desired direction. For SAR payloads, the requirements placed on such delay lines are particularly stringent, they must provide wideband operation (BW ≥ 1 GHz), continuously tunable delays extending into the hundreds of picoseconds, rapid reconfigurability on the sub-nanosecond scale, and minimal power consumption [27]. Recent research has demonstrated a range of viable implementations, including delay lines based on extended optical paths [28], nonlinear optical effects [29], and slow-light effects in engineered photonic structures [27].

Here, to overcome the problem related to tunable delay lines, each beam steering branch integrates an identical delay line, which is connected to the next through an innovative asymmetrical PS. This approach is based on the principle that the delay

between consecutive radiating elements must remain consistent across all branches, with each branch experiencing the same time delay to enable radiation spectrum steering. Although this architecture requires more delay lines ($N^2/2$) compared to the typical topology (N), it simplifies both design and fabrication by removing the need for tunable delay lines, thereby also reducing power consumption.

The proposed beam steering network, illustrated in Figure 5.3.1, consists of a laser diode (LD), a single-sideband Mach–Zehnder modulator (SSB-MZM), and a cascaded arrangement of asymmetric 1×2 power splitters (PSs) and optical delay lines (ODLs). The steering functionality is realized by tuning the emission wavelength of the laser source. The input RF signal (RF_{in}) is applied to the SSB-MZM, generating an optical sideband-modulated signal that is subsequently injected into the splitter–delay line array. Each 1×2 splitter is carefully engineered to provide the desired power division ratio, thereby ensuring proper amplitude distribution across the network.

For every stage, one branch of the splitter output is directed to a photodiode (PD), while the other branch propagates into the following ODL stage. The ODLs impose wavelength-dependent time delays, enabling fine control of the relative phase among the radiating elements. The resulting RF signals recovered by the PD array are then used to drive the antenna elements, where the optical delay mechanism provides beam steering control over the angular parameter θ.

To support compact and scalable integration, all functional components—including the LD, MZM, splitters, and ODLs—are designed in a waveguide-based platform, fully compatible with CMOS integration processes. This chip-scale implementation not only minimizes footprint and insertion losses but also improves system stability and paves the way toward large-scale, low-power photonic beamforming networks for next-generation Synthetic Aperture Radar (SAR) payloads.

For the beamforming network design, the COSMO-SkyMed mission has been adopted as a benchmark scenario. Specifically, an orbital altitude of 619.6 km, a velocity of 7.45 km/s, and an incidence angle of 30° are considered, typical values for EO spacecraft [30]. Unlike the L-band central frequency of COSMO-SkyMed (f_0 = 9.6 GHz), this study shifts operation to the Ka-band (f_0 = 35.75 GHz). The Ka-band provides several advantages such as reduced antenna size and weight, decreased baseline lengths for InSAR constellations, and improved DEM fidelity since radar reflections at these frequencies originate at the surface of targets rather than within their volume [26].

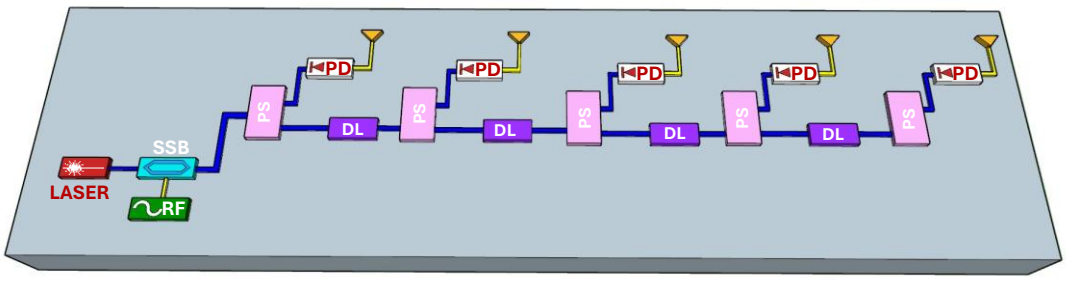

Figure 5.3.1 Proposed optical beamforming network architecture (SSB: single sideband modulator, PS: power splitter DL: optical delay lines, PD: photo diode).

The PAA and beamforming network specifications are derived from a stringent target spatial resolution of 90 cm in both azimuth and range for stripmap operation. This represents a substantial improvement compared to state-of-the-art spaceborne SAR systems, where stripmap resolutions are typically several meters. In accordance with ITU spectrum allocations, the available Ka-band bandwidth is about 500 MHz [31], corresponding to a theoretical range resolution of 30 cm. This bandwidth is therefore selected for the PAA design, enabling the system to exploit the maximum performance achievable within regulatory constraints.

From the azimuth resolution requirement (≤ 90 cm), the maximum (T_{max}) and minimum (T_{min}) inter-pulse repetition intervals were calculated using standard SAR equations, yielding 119 μs and 115 μs, respectively. Electromagnetic simulations using the Method of Moments (MoM) provided a main lobe azimuth beamwidth ($\Delta\Psi_{az}$) of 0.27°, while numerical simulations estimated an elevation beamwidth ($\Delta\Psi_{el}$) of 1.13°, satisfying the temporal constraints imposed by T_{min}. The resulting design achieves an azimuth resolution of 89 cm. In stripmap mode, the swath width depends on orbital altitude, elevation beamwidth, and incidence angle, with corrections for steering angle uncertainty. This analysis gives a swath width of 14.11 km, with variations from –1.16 km to +3.17 km.

Each radiating element was modelled as an ideal isotropic antenna, with element spacing set to $\lambda/2$ (4.2 mm at Ka-band) to ensure constructive interference. Based on the resolution and coverage requirements, the antenna array was dimensioned as a 90 × 376 element structure. The Synthetic Aperture Antenna (SAA) was partitioned into four modular panels, each comprising two columns of 18 tiles. Each tile contained 5 elements in elevation and 47 in azimuth (see Figure 5.3.2), resulting in an overall aperture size of 6 m × 1.5 m and a total directivity of 45 dB [32].

Radiation patterns in both azimuth and elevation confirmed that the designed beamwidths ($\Delta\Psi_{az}$ and $\Delta\Psi_{el}$) and the required steering range (θ) of ±15° were successfully achieved. Meeting this steering requirement necessitated per-element delay adjustments of 3.62 ps.

To realize these delays, a 1D photonic crystal-based optical delay line was designed. The proposed component is a top-grating waveguide incorporating a central defect, implemented as a longer grating tooth. This defect introduces resonant transmission channels within the photonic bandgap, with properties (free spectral range, Q-factor, and channel number) tunable via defect geometry.

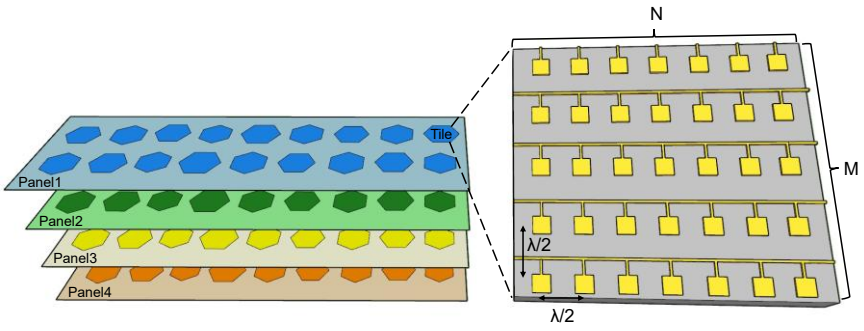

Figure 5.3.2 PAA architecture composed of 4 panels arranged in 9x2 tiles, each made of MxN (5x47) antennas spaced $\lambda/2$.

For example, a grating structure with 30 nm modulation depth, 32 defects, and a defect length L_{def} = 44.07 μm on a standard SOI platform (h =220 nm, w = 500 nm) provides insertion losses below 3 dB and a tunable delay range of 3.62 ps. To operate at the telecom wavelength of 1550 nm, the grating period has been set at 320 nm. Device behaviour is verified using the transfer matrix method (see Appendix C) and further analyzed via FEM modal simulations on COMSOL Multiphysics (see Appendix A).

A second fundamental device, the 1×2 asymmetric power splitter, has been implemented using an SOI-based multimode interferometer structure. The splitting ratio is tunable by engineering defects size within the SOI structure, enabling splitting ratios between 55% and 95%, with maximum insertion losses of 1.5 dB. Simulations have been performed using 3D-BPM simulator Rsoft, accounting for vertical field confinement to accurately estimate losses (see Appendix B)

In the optical beam steering network presented in this work, four asymmetric power splitters are employed, each engineered to achieve the specific splitting ratios required to balance the optical power delivered to the individual photodiodes, thereby eliminating the need for additional tunable delay elements for compensation. For every multimode interferometer device, the target splitting ratio, along with the corresponding defect length (L_{def}) and defect width (w_{def}) necessary for its implementation, has been identified, together with the expected insertion losses, that are reported in Table 5.3.1.

Figure 5.3.3 reports the BPM simulation results of MMI1 that perfectly matches the intended splitting ratio. The overall simulated results reproduce the anticipated interference patterns and optical field distribution, confirming the behavior of the devices. The strong agreement between the simulations and the theoretical design demonstrates that the MMIs can reliably deliver the intended asymmetric power division with high precision, ensuring the correct functionality and overall stability of the proposed photonic beam steering architecture.

Table 5.3.1 Asymmetrical Power Splitter design parameters and performance

MMI	Splitting ratio	L_{def} [μm]	w_{def} [μm]	Loss [dB]
1	0.8 (4/5)	4.6	1.59	2.4235
2	0.75 (3/4)	1.8	1.44	1.6804
3	0.667 (1/3)	1.4	1.5	1.5718
4	0.5 (1/2)	1	1	0.6589

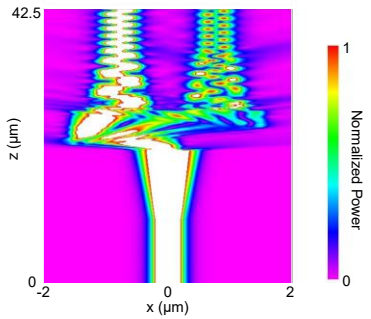

Figure 5.3.3 BPM simulation of the asymmetrical power splitter MMI1

Considering a representative steering case of ~12.5°, the beamforming network performance have been simulated in OptiSystem. Results indicate that the output power is highly sensitive to insertion losses in the delay line (> 3 dB) and asymmetric splitter losses. In the simulated chain, the final photodiode output was delayed by a cumulative τ_{tot} = 18.95 ps relative to the input, yielding a power of ~30 nW at the last detector. To achieve practical output levels, amplification is required, combining a transimpedance amplifier, a lobe-forming amplifier, and a high-power RF amplifier with a total gain exceeding 60 dB.

The SAA, when integrated with its photonic beamforming network, provides distributed amplification, agile beam steering, and low-noise reception of radar echoes. Together with waveform generation, frequency upconversion, super-heterodyne reception, and high-speed ADCs, the active antenna forms one of the most critical payload building blocks. The overall power consumption of the designed beamforming network has been estimated at approximately 1 kW, which is competitive for spaceborne active phased-array SAR payloads in Ka-band operation.

5.4 Photonic FFT processor

Finally, in compliance with the need for on-board data screening, a photonic processor capable of performing the FFT, fundamental for SAR data compression, has been developed. Indeed, considering the advantages of optical processing—such as reduced requirements in terms of SWaP, cost-effectiveness, broader bandwidth, the ability to manage large data volumes, and the ongoing progress in photonic technologies for space applications—there is growing interest in novel architectures for direct onboard processing of SAR data. This paradigm aims to significantly reduce the amount of raw data transmitted to ground stations. To this end, the conventional A/D converter in the SAR receiving chain can be replaced with a photonic system capable of real-time onboard data processing, making use of an integrated photonic Fast Fourier Transform (FFT) processor. Such an approach aligns closely with the objectives of the NewSpace framework.

The architecture proposed here, aims to overcome the primary limitations of existing FFT implementations. Specifically, free-space optical FFTs, while functional, are bulky and sensitive to external perturbations, cascaded Mach-Zehnder interferometer-based FFTs suffer instead from scalability issues, large footprint, and elevated power consumption, butterfly-pattern optical FFTs are affected by footprint, losses, and calibration complexity, and purely electronic FFT processors face inherent challenges in terms of power dissipation, latency, and limited processing speed. In contrast, the solution introduced here ensures compatibility with the stringent performance requirements of SAR systems.

The proposed photonic FFT processor relies on a flexible and reconfigurable $LiNbO_3$-based architecture capable of full photonic, real-time decomposition and processing of each echo's spectral component. The system comprises a demultiplexer, an array of tunable phase shifters, and a multiplexer, designed to operate in the Ka-band. Incoming SAR echoes at the carrier frequency f_c (within the Ka-band) are first converted to the optical domain through an electro-optical

modulator, where they interact with a continuous-wave laser at frequency f_0. The resulting beat signal at ($f_0 - f_c$) is then sampled at a frequency f_s using an electro-optical Mach-Zehnder modulator. For an 8-bit FFT, 2^8 samples, uniformly distributed across wavelength channels, are demultiplexed by an arrayed waveguide grating. Each sample is subsequently weighted according to the FFT kernel through a bank of electro-optical phase shifters, where the applied voltage induces the required phase shift. Finally, a symmetric AWG recombines the weighted outputs, yielding the FFT spectral component of the received echo. By dynamically adjusting the phase shifts in the EO-tunable waveguide array, successive FFT components can be generated, enabling the full spectral reconstruction of the SAR signal. The proposed configuration is illustrated in Figure 5.4.1, which also reports signals at different points of the system.

The FFT itself is an optimized algorithm for computing the discrete Fourier transform (DFT) over N input time-domain samples, with N restricted to integer powers of two. The DFT is expressed as $X_k = \sum_{n=0}^{N-1} x_n e^{-\frac{j2\pi}{N} \cdot k \cdot n} = \sum_{n=0}^{N-1} x_n w_N^{k \cdot n}$, $k = 0,\ldots N\text{-}1$, where $w_N = e^{-j2\pi/N}$ denotes the weight factor, x_n the input vector of time samples, and X_k the output frequency-domain vector. Constructing the FFT involves multiplying the weight matrix $w_{N\times N}$ with the input vector, yielding the spectral coefficients X_k.

The design specifications have been derived from the requirements of the Copernicus Sentinel-1 mission [33]. In particular, a carrier frequency f_c = 40 GHz, a sampling frequency f_s = 300 MHz, and $N = 2^{10}$ samples are selected. Functional validation of the FFT was performed by cascading the constituent building blocks dimensioned to account for realistic insertion losses. The total system loss was estimated at ~12 dB on the carrier frequency, while higher-order harmonics were strongly suppressed, as expected from the continuous-signal assumption. Moreover, thanks to the minimal non-uniformity in the insertion loss of AWGs, no spurious harmonics or artificial spectral components were observed, preserving the FFT's integrity. This approach was demonstrated to meet all operational constraints associated with Copernicus-I [33].

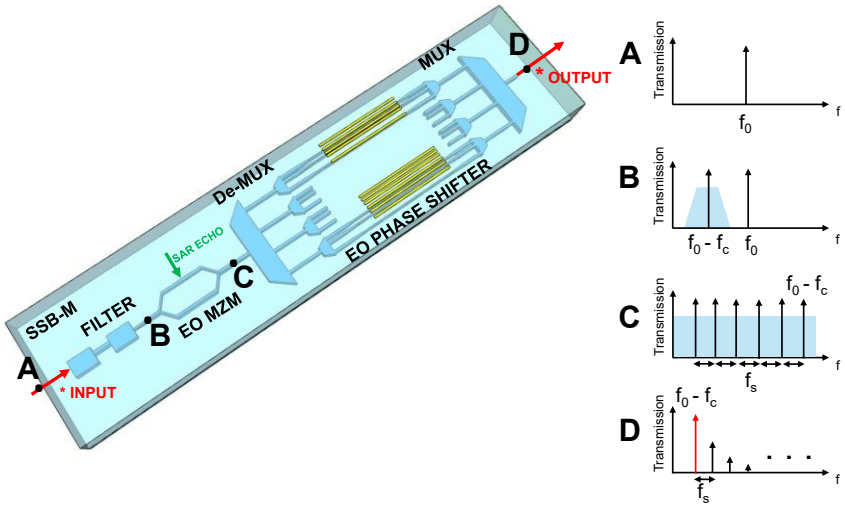

Figure 5.4.1 FFT photonic processor architecture and signal manipulations through it.

The proposed scheme provides 256 frequency channels, each spaced 300 MHz apart within the Ka-band. By leveraging thin-film $LiNbO_3$ with inherently low propagation losses, the processor achieves a maximum insertion loss of ~12 dB, a drive voltage of 7 V, a maximum tunable delay of 0.98 ns, and a phase shifter length of 4.1 mm. These performance metrics effectively overcome the limitations of the Cooley-Tukey butterfly optical FFT in terms of scalability, footprint, and calibration, as well as those of traditional electronic FFT processors regarding energy consumption and latency, all while remaining consistent with SAR processing demands [34–35]. Additional details on the proposed implementation are provided in [36-37].

5.5 Technological challenges

All the devices constituting the SAR architecture illustrated in Fig. 5.1.1 have corresponding and experimentally validated implementations in the photonic domain. In particular, linearly chirped microwave waveguides (LCMWGs) [38], high-performance electro-optic modulators [39], frequency converters [40], optical amplifiers capable of watt-class output powers [41], beamforming networks based on silicon photonics phase shifters [42], and phased-array antennas implemented on silicon-on-insulator platforms [43] have all been successfully demonstrated and fabricated on photonic platforms. These results collectively indicate that the individual functional blocks required for a fully photonic SAR payload are no longer limited by device-level feasibility, but rather by system-level integration and co-packaging challenges.

The proposed linearly chirped microwave waveguide (LCMWG) occupies a footprint of approximately 4 × 4 cm^2, which represents the largest area contribution within the overall photonic SAR architecture. This footprint is primarily dictated by the required dispersion and delay length needed to generate and process wideband chirped microwave signals with adequate resolution. In contrast, the beamforming network exhibits a significantly more compact layout, with an estimated footprint of approximately 2 cm × 1 mm, owing to its implementation based on phase shifters and compact optical delay lines that do not require long optical path lengths. Similarly, the fast Fourier transform (FFT) block is expected to occupy an intermediate footprint, on the order of 3 cm × 1 mm. In this case, the overall dimensions are largely determined by the cumulative length of cascaded arrayed waveguide gratings (AWGs) and electro-optic phase shifters, which dominate the layout due to their wavelength-dependent routing and phase control requirements. These estimates highlight how the physical footprint of the proposed photonic system is strongly influenced by the functional role of each block, with dispersive and spectral-processing components setting the dominant area constraints, while beamforming and phase-control elements remain comparatively compact.

The primary remaining limitations arise from the need to integrate heterogeneous technological platforms, each optimized for specific functions—for instance, thin-

film lithium niobate (TFLN) for high-speed modulation and signal processing, indium phosphide (InP) for efficient laser sources, and silicon nitride (SiN) for low-loss waveguiding and passive routing. Heterogeneous bonding provides a powerful and scalable solution to this challenge by enabling efficient electrically pumped light generation on silicon, thereby overcoming a fundamental barrier to CMOS-compatible photonic integration. This approach allows high-performance III–V active devices to be seamlessly combined with silicon's superior passive components, in some cases achieving performance levels that surpass those of monolithically integrated III–V platforms. In addition, multiple die bonding supports the realization of complex, multi-wavelength photonic integrated circuits incorporating efficient modulators, high-speed photodetectors, and advanced signal processing functionalities without the need for regrowth, while simultaneously reducing fabrication cost and improving yield.

As the density and complexity of photonic integration increase, the mitigation of parasitic reflections and backscattering becomes a critical design consideration, particularly for laser stability and system robustness. Heterogeneous integration further enables the incorporation of on-chip non-reciprocal components, such as isolators and circulators, through the bonding of magnetic materials including Ce:YIG, thereby addressing these challenges at the chip level. Overall, heterogeneous silicon photonics is approaching technological maturity, with commercial deployment already established in data center applications and strong prospects for expansion into emerging domains such as LIDAR, optical gyroscopes, sensing, and microwave and optical clocks [44].

5.6 Conclusions

This section provides a comprehensive assessment of the advantages of photonic solutions over conventional electronics for SAR payload building blocks. It discusses which technologies have already been experimentally demonstrated and introduces innovative approaches to overcome emerging limitations, paving the way for next-generation photonic SAR systems.

More specifically, the chirped waveform generator achieves a phase noise lower than –110 dBc/Hz at a 10 kHz offset from the carrier and delivers an output power exceeding 10 dBm, owing to the use of an ultra-high-Q ring resonator. The beamforming network is implemented with phased array antennas providing a main lobe directivity of approximately 45 dB. This configuration enables a squint-free bandwidth of 0.5 GHz and supports beam steering over ±15°. In this case, steering is realized by tuning the laser source's central frequency, since the delay lines are not tunable. The total power consumption of the beamforming network is on the order of 1 kW. Regarding the photonic FFT processor, its fully reconfigurable architecture contributes to payload miniaturization while supporting 8-bit ADC operation with a 300 MHz sampling spacing of the up-converted RF signal. A key milestone is the demonstration of real-time on-board SAR echo processing, enabled

by a delay of 0.98 ns, which allows information discrimination prior to downlinking, thereby reducing the overall power consumption.

Looking ahead, the adoption of integrated photonic technologies in SAR payloads is expected to become a key enabler for the NewSpace paradigm, where cost-effective, scalable, and lightweight solutions are essential. The proposed photonic building blocks are inherently compatible with CubeSats and small-satellite platforms, enabling the deployment of distributed SAR constellations with sub-meter resolution, rapid revisit times, and on-board real-time data processing. This approach would support wider coverage and more frequent monitoring of dynamic Earth processes, ranging from disaster management to climate change observation.
From a technological perspective, the main challenges are associated with the integration of multiple photonic platforms, each optimized for specific functions such as modulation, light generation, and low-loss waveguiding. Recent advances in heterogeneous and multi-die bonding provide an effective solution to these challenges by allowing high-performance active and passive components to be co-integrated on a single silicon platform, while also enabling multi-wavelength operation and improved system-level performance. Moreover, heterogeneous integration facilitates the incorporation of non-reciprocal elements required to mitigate reflections and backscattering in dense photonic circuits, contributing to improved stability and robustness.
As photonic integration technologies continue to mature, supported by progress in heterogeneous integration, advanced packaging, and radiation-hardened design, fully photonic SAR payloads are expected to become not only technically feasible but also economically competitive. This evolution has the potential to transform the design and operation of future spaceborne radar missions, enabling modular, multi-mission payloads capable of supporting both Earth observation and telecommunications functionalities on a shared hardware platform.

References

[1]. Y. Aoki, M. Furuya, F. De Zan, M. P. Doin, M. Eineder, M. Ohki, T. J. Wright, "L-band Synthetic Aperture Radar: Current and future applications to Earth sciences," *Earth, Planets and Space*, vol. 73, no. 1, p. 56, 2021, doi: https://doi.org/10.1186/s40623-021-01363-x.

[2]. A. Renga, M. D. Graziano, M. Grasso, A. Moccia, "Evaluation of design parameters for formation flying SAR," in *EUSAR 2021; 13th European Conference on Synthetic Aperture Radar, online*, 2021, pp. 1-4.

[3]. A. Renga, M. D. Graziano, A. Moccia, "Formation Flying SAR: analysis of imaging performance by Array Theory," *IEEE Transactions on Aerospace and Electronic Systems,* vol. 57, no. 3, pp. 1480-1497, 2020, doi: 10.1109/TAES.2020.3043526.

[4]. C. Ciminelli, F. Dell'Olio, M. N. Armenise, *Photonics in Space: Advanced Photonic Devices and Systems*, Singapore, Singapore, World Scientific, 2016.

[5]. G. Brunetti, N. Sasanelli, N. Saha, G. Campiti, F. Hassan, A. di Toma, M. N. Armenise, C. Ciminelli, "Integrated photonics for NewSpace," in *Berta, R., De Gloria, A. (eds) Applications in Electronics Pervading Industry, Environment and Society. ApplePies 2022*. Lecture Notes in Electrical Engineering, vol 1036. Springer, Cham., 2023, https://doi.org/10.1007/978-3-031-30333-3_39

[6]. A. N. Bozovich, Photonic integrated circuits (PICs) for next generation space applications, in *Virtual 2020 NEPP Electronics Technology Workshop (ETW), Greenbelt, Massachusetts, 2020*.

[7]. W. A. Imbriale, L. Boccia, *Space Antenna Handbook*, Hoboken, New Jersey, USA, John Wiley & Sons, 2012.

[8]. D. Pilz, P. Feldle, "RF-payload of TerraSAR-X," in *Proceeding German Microwave Conference (GeMiC), Ulm, Germany, 2005*, pp. 140-143.
[9]. M. N. Armenise, F. Dell'Olio, C. Ciminelli, C. Galeone, G. Brunetti, "Microphotonics-based architectures of mini-SAR payloads," In *21st International Conference on Transparent Optical Networks (ICTON), Angers, France, 2019*, pp. 1-4, doi: 10.1109/ICTON.2019.8840245.
[10]. A. di Toma, G. Brunetti, M. N. Armenise, C. Ciminelli, "Synthetic aperture radar payloads: migration towards photonic approach," in *Small Satellites Systems and Services Symposium (4S 2024),* Palma de Mallorca, Spain, May 27-31, 2024, vol. 13546, pp. 1372-1383, doi: https://doi.org/10.1117/12.3062644.
[11]. H. Chi, C. Wang, J. Yao, "Photonic generation of wideband chirped microwave waveforms," *IEEE Journal of Microwaves*, vol. 1, no. 3, pp. 787-803, 2021, doi: 10.1109/JMW.2021.3085868.
[12]. M. Gagné, S. Loranger, J. Lapointe, R. Kashyap, "Fabrication of high quality, ultra-long fiber Bragg gratings: up to 2 million periods in phase," *Optics Express*, vol. 22, no. 1, pp. 387-398, 2014, doi: https://doi.org/10.1364/OE.22.000387.
[13]. F. Zhang, Q. Guo, Z. Wang, P. Zhou, G. Zhang, J. Sun, S. Pan, "Photonics-based broadband radar for high-resolution and real-time inverse synthetic aperture imaging," *Optics Express*, vol. 25, no. 14, pp. 16274-16281, 2017, doi: https://doi.org/10.1364/OE.25.016274.
[14]. T. Hao, J. Tang, W. Li, N. Zhu, M. Li, "Tunable Fourier domain mode-locked optoelectronic oscillator using stimulated Brillouin scattering," *IEEE Photonics Technology Letters*, vol. 30, no. 21, pp. 1842-1845, 2018, doi: 10.1109/LPT.2018.2866192.
[15]. G. Serafino, C. Porzi, B. Hussain, F. Scotti, F. Falconi, M. Chiesa, V. Toccafondo, A. Bogoni, P. Ghelfi, "High-performance beamforming network based on si-photonics phase shifters for wideband communications and radar applications," *IEEE Journal of Selected Topics in Quantum Electronics*, vol. 26, no. 5, pp. 1-11, 2020, doi: 10.1109/JSTQE.2020.2995292.
[16]. D. I. Lialios, N. Ntetsikas, K. D. Paschaloudis, C. L. Zekios, S. V. Georgakopoulos, G. A. Kyriacou, "Design of true time delay millimeter wave beamformers for 5G multibeam phased arrays," *Electronics*, vol. 9, no. 8 p. 1331, 2020, doi: https://doi.org/10.3390/electronics9081331.
[17]. M. Longbrake, "True time-delay beamsteering for radar," In *IEEE National Aerospace and Electronics Conference (NAECON), Dayton, OH, USA, 2012* pp. 246-249, doi: 10.1109/NAECON.2012.6531062.
[18]. S. Colburn, Y. Chu, E. Shilzerman, A. Majumdar, "Optical frontend for a convolutional neural network," *Applied Optics*, vol. 58, no. 12, pp. 3179-3186, 2019, doi: https://doi.org/10.1364/AO.58.003179.
[19]. M. Miscuglio, P. Gupta, A. Babakhani, C. W. Wong, H. Dalir, T. El-Ghazawi, V. J. Sorger, "Photonic convolutional processor for network edge computing," in *AI and Optical Data Sciences, San Francisco, California, USA, 2020*, vol. 11299, p. 112990K, doi: https://doi.org/10.1117/12.2545970.
[20]. W. Liu, M. Li, R. S. Guzzon, E. J. Norberg, J. S. Parker, M. Lu, L. A. Coldren, J. Yao, "A fully reconfigurable photonic integrated signal processor," *Nature Photonics*, vol. 10, pp. 190-195, 2016, doi: https://doi.org/10.1038/nphoton.2015.281.
[21]. J. K. George, H. Nejadriahi, V. J. Sorger, "Towards on-chip optical ffts for convolutional neural networks," in *IEEE International Conference on Rebooting Computing (ICRC*), *Washington, DC, USA,* 2017, pp. 1-4, doi: 10.1109/ICRC.2017.8123675.
[22]. K. Zhang, S. Zhao, Y. Yin, T. Lin, X. Li, W. Jiang, G. Wang, "Photonic generation and transmission of linearly chirped microwave waveform with increased time-bandwidth product," *IEEE Access*, vol. 7, pp. 47461-47471, 2019, doi: 10.1109/ACCESS.2019.2909738.
[23]. W. Li, J. Yao, "Generation of linearly chirped microwave waveform with an increased time-bandwidth product based on a tunable optoelectronic oscillator and a recirculating phase modulation loop," *Journal of Lightwave Technology*, vol. 32, no. 20, pp. 3573-3579, 2014, doi: 10.1109/JLT.2014.2309392.
[24]. G. Brunetti, F. Dell'Olio, D. Conteduca, M. N. Armenise, C. Ciminelli, "Comprehensive mathematical modelling of ultra-high Q grating-assisted ring resonators," *Journal of Optics*, vol. 22, no. 3, p. 035802, 2020, doi: 10.1088/2040-8986/ab71eb.
[25]. G. Brunetti, M. N. Armenise, C. Ciminelli, "Chip-scaled Ka-band photonic linearly chirped microwave waveform generator," *Frontiers in Physics*, vol. 10, p. 785650, 2022, doi: https://doi.org/10.3389/fphy.2022.785650.

[26]. T. Tatoli, D. Conteduca, F. Dell'Olio, C. Ciminelli, M. N. Armenise, "Graphene-based fine-tunable optical delay line for optical beamforming in phased-array antennas," *Applied Optics*, vol. 55, no. 16, pp. 4342-4349, 2016, doi: https://doi.org/10.1364/AO.55.004342.
[27]. H. Lee, T. Chen, J. Li, O. Painter, K. J. Vahala, "Ultra-low-loss optical delay line on a silicon chip," *Nature Communications*, vol. 3, no. 1, p. 867, 2012, doi: https://doi.org/10.1038/ncomms1876.
[28]. R. Pant, A. Byrnes, C. G. Poulton, E. Li, D.-Y. Choi, S. Madden, B. Luther-Davies, B. J. Eggleton, "Photonic-chip-based tunable slow and fast light via stimulated Brillouin scattering," *Optics Letters*, vol. 37, no. 5, pp. 969-971, 2012, doi: https://doi.org/10.1364/OL.37.000969
[29]. eoPortal, "COSMO-SkyMed," Accessed September 18, 2025 [Online]. Available: https://www.eoportal.org/satellite-missions/cosmo-skymed#space-segment
[30]. M. D'Errico, *Distributed space missions for earth system monitoring*, Berlin, Germany Springer, 2012.
[31]. M. D. Salvo, C. Germani, A. Torre, L. Borgarelli, "Ka-band applications for remote sensing from space," in *Proceedings of IEEE Gold Remote Sensing Conference, Livorno, Italy, 2010*.
[32]. Y. Huang, *Antennas: from theory to practice*, Hoboken, New Jersey, USA, John Wiley & Sons, 2021.
[33]. eoPortal, "Copernicus: Sentinel-1 — The SAR Imaging Constellation for Land and Ocean Services," Accessed September 18, 2025 [Online]. Available: https://www.eoportal.org/satellite-missions/copernicus-sentinel-1#copernicus-sentinel-1--the-sar-imaging-constellation-for-land-and-ocean-services.
[34]. M. Ahmed, Y. Al-Hadeethi, A. Bakry, H. Dalir, V. J. Sorger, "Integrated photonic FFT for photonic tensor operations towards efficient and high-speed neural networks," *Nanophotonics*, vol. 9, no. 13, pp. 4097-4108, 2020, doi: https://doi.org/10.1515/nanoph-2020-0055.
[35]. D. Hillerkuss, M. Winter, M. Teschke, A. Marculescu, J. Li, G. Sigurdsson, K. Worms, S. Ben Ezra, N. Narkiss, W. Freude, and J. Leuthold, "Simple all-optical FFT scheme enabling Tbit/s real-time signal processing," *Optics Express*, vol. 18, no. 9, pp. 9324-9340, 2010, doi: https://doi.org/10.1364/OE.18.009324.
[36]. M. N, Armenise, A. di Toma, G. Brunetti, N. Saha, C. Ciminelli, "Flexible photonic integrated circuits: a new paradigm to process data on-board satellites," in *2023 23rd International Conference on Transparent Optical Networks (ICTON)*, Bucharest, Romania, July 2-6, 2023, p. 1, doi: 10.1109/ICTON59386.2023.10207537.
[37]. A. di Toma, G. Brunetti, M. N. Armenise, C. Ciminelli, "LiNbO_3-Based Photonic FFT Processor: An Enabling Technology for SAR On-Board Processing," *Journal of Lightwave Technology*, vol. 43, no. 2, pp. 912-921, 2025, doi: 10.1109/JLT.2024.3453670.
[38]. L. Wang, Y. Liu, Y. Chen, W. Gou, S. Cui, Y. Yu, X. Xiao, Y. Yu, X. Zhang, "Generation of reconfigurable linearly chirped microwave waveforms based on Fourier domain mode-locked optoelectronic oscillator," Journal of Lightwave Technology, vol. 40, no. 1, pp. 85–92, 2022, doi: 10.1109/JLT.2021.3119438
[39]. Y. Li, T. Lan, D. Yang, J. Bao, M. Xiang, F. Yang, Z. Wang, "High-performance Mach–Zehnder modulator based on thin-film lithium niobate with low voltage-length product," ACS Omega, vol. 8, no. 10, pp. 9644–9651, 2023, doi: https://doi.org/10.1021/acsomega.3c00310
[40]. C. G. Bottenfield, S. E. Ralph, "High-performance fully integrated silicon photonic microwave mixer subsystems," Journal of Lightwave Technology, vol. 38, no. 19, pp. 5536–5545, 2020, doi: 10.1109/JLT.2020.2990693
[41]. N. Singh, J. Lorenzen, K. Wang, M. A. Gaafar, M. Sinobad, H. Francis, M. Edelmann, M. Geiselmann, T. Herr, S. M. Garcia-Blanco, F. X. Kärtner, "Watt-class silicon photonics-based optical high-power amplifier," Nature Photonics, vol. 19, no. 3, pp. 307–314, 2025, doi: https://doi.org/10.1038/s41566-024-01587-9
[42]. G. Serafino, C. Porzi, B. Hussain, F. Scotti, F. Falconi, M. Chiesa, V. Toccafondo, A. Bogoni, P. Ghelfi, "High-performance beamforming network based on Si-photonics phase shifters for wideband communications and radar applications," IEEE Journal of Selected Topics in Quantum Electronics, vol. 26, no. 5, pp. 1–11, 2020, doi: 10.1109/JSTQE.2020.2995292
[43]. K. Van Acoleyen, H. Rogier, R. Baets, "Two-dimensional optical phased array antenna on silicon-on-insulator," Optics Express, vol. 18, no. 13, pp. 13655–13660, 2010, doi: https://doi.org/10.1364/OE.18.013655

[44]. T. Komljenovic, D. Huang, P. Pintus, M. A. Tran, M. L. Davenport, J. E. Bowers, “Photonic integrated circuits using heterogeneous integration on silicon,” Proceedings of the IEEE, vol. 106, no. 12, pp. 2246–2257, 2018, doi: 10.1109/JPROC.2018.2864668

Chapter 6

Conclusions

The work presented in this thesis has explored the disruptive potential of reconfigurable photonic circuits for next-generation satellite payloads, addressing critical challenges posed by the NewSpace paradigm. Driven by the increasing demand for compact, lightweight, and energy-efficient systems, this research has demonstrated how photonic integration, and in particular reconfigurable architectures, can unlock new functionalities and performance levels that extend beyond the reach of conventional electronic solutions.

Beginning with the design and demonstration of reconfigurable microwave photonic band-pass filters, the thesis has shown how spectral selectivity and adaptability can be enhanced while respecting the strict SWaP requirements of CubeSat-scale missions. Two complementary solutions have been investigated, a silicon-based dual-ring resonator filter, offering 45 dB stopband rejection, 20 MHz bandwidth tuning, and central frequency reconfigurability of up to 180 MHz with low power consumption, and a TriPleX CROW-based filter with PCM phase shifters, achieving 20 GHz frequency tuning, 2 GHz bandwidth control, and a tuning efficiency of 37.4 GHz/mW. Together, these results mark a progression from thermo-optic tuners toward energy-efficient, non-volatile photonic filters capable of agile spectrum management in spaceborne telecom payloads.

The investigation then extended to optical beamforming networks (OBFNs), where the limitations of traditional thermo-optic technologies were addressed through the integration of phase-change materials and innovative device architectures. The proposed PCM-based OBFN achieved a tunable delay of 140 ps with two orders of magnitude lower power consumption than metallic heaters, stable operation over a bandwidth of 4.3–7 GHz, and continuous steering over ±60°. In parallel, SAR-tailored building blocks were demonstrated, including an innovative asymmetrical power splitter based on an MMI achieving various splitting ratios (ranging from 55% to 95%) without altering the device length, collectively supporting large-scale photonic SAR payloads with reduced power demands (~1 kW). Finally, a metasurface-based beamformer demonstrated ±30° field of view with complete

sidelobe suppression, offering an ultra-compact and scalable path for optical intersatellite links. These contributions highlight the transition from bulky and power-hungry beamformers toward lightweight, adaptive, and energy-efficient flexible photonic networks.

In the field of on-board photonic data processing, the thesis has introduced an integrated photonic Fast Fourier Transform (FFT) processor capable of computing spectral samples in real time, surpassing the intrinsic speed and latency limitations of electronic DSP-based approaches. The architecture supports 256 channels spaced 300 MHz apart in the Ka-band, with a maximum delay of 0.98 ns, 12 dB insertion loss, and phase shifters only 4.1 mm long. By enabling direct optical-domain processing of SAR echoes, this device reduces downlink data volume, optimizes bandwidth usage, and supports distributed SAR constellations with autonomous on-board intelligence.

The thesis culminated in the development of photonic building blocks for a fully integrated SAR system, combining an ultra-high-Q chirped waveform generator (phase noise < –110 dBc/Hz at 10 kHz offset, output power > 10 dBm), a phased array antenna with 45 dB directivity and squint-free 0.5 GHz bandwidth, and the proposed photonic FFT processor. The system demonstrated real-time SAR echo processing and a total beamforming power consumption of ~1 kW, marking a decisive step toward the feasibility of all-photonic SAR payloads compatible with small satellites and CubeSats.

Taken together, these contributions underscore the central objective of this research, demonstrating how reconfigurable photonic circuits can enable compact, adaptive, and energy-efficient payloads for the next generation of satellite missions. Numerical benchmarks such as 45 dB filter rejection, 20 GHz frequency reconfigurability, ±60° beam steering with <1 ps delay ripple, and real-time FFT computation illustrate the tangible progress achieved in meeting agencies', space companies', and NewSpace economy's requirements.

Looking forward, several directions emerge for future work. The full exploitation of phase-change materials, combined with hybrid integration of electro-optic tuning mechanisms, offers a pathway to simultaneously optimize speed, tunability, and energy efficiency. The integration of metasurfaces with PIC may further extend the field of view and resolution of beamforming systems while reducing footprint. Despite the progress achieved, several challenges remain before fully photonic payloads can transition from laboratory demonstrations to operational missions.
A central limitation lies in the lack of standardization of technological processes for integrated photonic devices. Unlike microelectronics, where CMOS foundries adhere to well-established process design kits (PDKs) and interoperability standards, photonic integration is still fragmented across platforms (silicon photonics, TriPleX, InP, $LiNbO_3$, and hybrid approaches). This diversity hampers large-scale adoption, complicates supply chains, and increases costs for space-qualified photonic devices. Establishing standardized processes, interoperable PDKs, and common design frameworks will be essential for achieving the maturity level required for widespread industrial deployment. Another critical bottleneck is the insufficient availability of radiation hardness testing and qualification for

integrated photonic devices. While individual optical components have shown resilience to certain space radiation environments, systematic testing of complete photonic integrated circuits under realistic space conditions remains limited and often not aligned with mission timelines. The absence of a consolidated roadmap for radiation-hard photonic device qualification represents a significant risk for mission adoption, particularly for long-duration deep-space or high-radiation environments. Ongoing efforts by space agencies and industrial stakeholders are moving toward scheduled testing campaigns, yet a coordinated, standardized framework is urgently needed to ensure reliability and accelerate the transition of photonic technologies into operational payloads. Advances in heterogeneous integration and radiation-hardened packaging will be essential to translate these theoretical demonstrations into space-qualified hardware. The convergence of photonic filters, beamformers, and processors into multifunctional, software-defined photonic payloads could give rise to a new generation of agile satellites—capable of adapting on orbit to evolving mission needs, spectrum allocations, and communication standards.

In conclusion, this thesis demonstrates that reconfigurable integrated photonics is not merely an incremental improvement but a paradigm-shifting technology for space systems. By offering unmatched SWaP efficiency, spectral and spatial agility, and real-time processing capabilities, photonic circuits pave the way for a new era of intelligent, resilient, and resource-efficient satellites that will play a central role in both Earth observation and next-generation telecommunications.

Appendix A

COMSOL Multiphysics and Finite Element Method (FEM)

The Finite Element Method (FEM) is a numerical technique for solving partial differential equations (PDEs) that arise in physics and engineering. It is based on the weak (or variational) formulation of PDEs and is particularly well-suited to problems defined on complex geometries and involving heterogeneous material properties. This method is the backbone of the COMSOL Multiphysics simulation platform, which provides a versatile environment for modeling coupled physical phenomena.

Consider a general partial differential equation defined on a bounded domain $\Omega \subset R^n$ with boundary $\partial\Omega$

$$\begin{aligned} L(u) &= f \quad in\ \Omega, \\ B(u) &= g \quad on\ \partial\Omega \end{aligned}$$

where L is a differential operator, u the unknown field, f a source term, and B a boundary operator encoding Dirichlet, Neumann, or Robin boundary conditions.

In the Galerkin formulation, one seeks an approximate solution u_h in a finite-dimensional subspace $V_h \subset V$, where V is a Sobolev space such as $H^1(\Omega)$. The weak form is obtained by multiplying the governing PDE by a test function $v \in V$, integrating over the domain, and applying integration by parts

$$\int_\Omega v\, L(u)\, d\Omega = \int_\Omega vf\, d\Omega + \partial \int_{\partial\Omega} vg\, d\Gamma$$

Replacing u with the finite-dimensional approximation u_h and restricting v to the same finite-dimensional space yields a system of algebraic equations $K\, u = f$, where K is the stiffness (or system) matrix, u is the vector of nodal unknowns, and f is the load vector. The accuracy of FEM depends on the choice of basis functions (often piecewise polynomials) and mesh resolution.

The domain Ω is partitioned into a finite set of non-overlapping elements $\{\Omega_e\}$, such that

$$\Omega \approx \cup \Omega_e$$

Within each element, the approximate solution is expressed as a linear combination of shape functions $N_i(x)$

$$u_h(x) = \sum_{i=1}^{N} u_i N_i(x)$$

where u_i are the nodal values. COMSOL typically employs Lagrange basis functions, which interpolate the solution at nodal points. Linear, quadratic, and higher-order polynomials can be used depending on the required accuracy.
The element matrices are computed locally and then assembled into the global system. For a prototypical diffusion-type PDE ($-\nabla \cdot (D\nabla u) = f$) the weak form reads

$$\int_{\Omega} \nabla v \cdot D\, \nabla u \, d\Omega = \int_{\Omega} vf \, d\Omega$$

The corresponding element stiffness matrix is $K_{ij}^{(e)} = \int_{\Omega_e} \nabla N_i \cdot D\, \nabla N_j \, d\Omega$, and the element load vector is $f_i^{(e)} = \int_{\Omega_e} N_i \, f \, d\Omega$. The global system is obtained by assembling all contributions

$$K = \sum_e K^{(e)}, f = \sum_e f^{(e)}$$

In COMSOL Multiphysics, this procedure is implemented in a general and automated fashion while remaining faithful to the fundamental FEM framework. The workflow begins with the definition of the computational domain, which can be constructed using built-in geometric primitives or imported from external CAD models. Once the geometry is specified, the governing physics is defined either through pre-configured modules such as electromagnetics, acoustics, or structural mechanics, or by explicitly specifying coefficients in a general form PDE interface. The latter is written as

$$ea\frac{\partial^2 u}{\partial t^2} + da\frac{\partial u}{\partial t} - \nabla \cdot (c\nabla u + \alpha u - \gamma) + \beta \cdot \nabla u + au = f$$

a highly flexible representation capable of capturing a wide variety of linear and nonlinear physical problems. After the governing equations are established, the geometry is discretized into a finite element mesh consisting of elements such as triangles, quadrilaterals, tetrahedra, or hexahedra, depending on the spatial dimension and problem requirements. COMSOL provides automated meshing algorithms, while also allowing manual control over element size, distribution, and refinement strategy. The discretization stage also involves the selection of basis functions, typically Lagrange polynomials of user-specified order, although for vectorial problems in electromagnetics the software employs curl-conforming

Nédélec edge elements to ensure that tangential field components remain continuous across element boundaries, thus maintaining the physical fidelity of Maxwell's equations.

Once the mesh and basis functions are established, the assembly of the global algebraic system proceeds internally, following the same principle of accumulating elemental matrices and load vectors into a global system. For time-dependent problems, COMSOL applies implicit time-stepping schemes such as backward differentiation formulas, while nonlinear problems are treated using Newton-type iterations that involve repeated assembly and factorization of the Jacobian matrix. Linear systems are solved with either direct solvers, such as sparse LU decomposition, or iterative Krylov subspace solvers, with preconditioning strategies adapted to the specific physics.

Because COMSOL is designed for multiphysics simulations, the weak forms corresponding to different physics modules are coupled naturally at the variational level. This implies that when, for instance, thermal expansion couples structural mechanics to heat transfer, or when electromagnetic heating couples wave propagation to conduction, the resulting algebraic system simultaneously accounts for all field interactions. The global system thus represents the monolithic interaction of all involved phenomena, guaranteeing consistent treatment of couplings.

Following the solution phase, post-processing tools allow for evaluation of the computed field distributions, derived quantities, and integral measures such as fluxes, scattering parameters, and effective indices. Since the finite element basis functions permit interpolation of the solution across the domain, COMSOL provides continuous field visualizations and quantitative data extraction at arbitrary points, lines, and surfaces. In essence, the software streamlines the rigorous mathematical framework of FEM into a versatile workflow where geometry, physics, discretization, solution, and analysis are seamlessly integrated.

Appendix B

Beam Propagation Method (BPM)

The beam propagation method (BPM) is a widely used numerical technique for modelling the evolution of optical fields in waveguides and other inhomogeneous dielectric media, especially in scenarios where light propagates predominantly along a preferred axis. Unlike full vectorial methods that solve Maxwell's equations directly, BPM relies on approximations that exploit the slowly varying nature of optical envelopes, which makes it computationally efficient for simulating guided modes, waveguide couplers, and integrated photonic structures. Its formulation begins with the Helmholtz equation derived from Maxwell's equations in the frequency domain.

Starting from Maxwell's equations under time-harmonic conditions with angular frequency ω, the electric field $E(r)$ satisfies the vector wave equation. For scalar fields, which provide a sufficiently accurate description in many guided-wave problems, one considers the scalar Helmholtz equation

$$\nabla^2 E(x,y,z) + k_0^2 n^2(x,y,z) E(x,y,z) = 0$$

where E is the field envelope, $k_0 = \omega/c = 2\pi/\lambda$ is the free-space wavenumber, and $n(x,y,z)$ is the refractive index distribution. The domain is typically structured such that light predominantly propagates along the longitudinal direction (z-axis), while the transverse coordinates (x,y) account for lateral confinement. To enable efficient computation, the field is factorized into a rapidly varying carrier and a slowly varying envelope

$$E(x,y,z) = \psi(x,y,z) e^{i\beta_0 z}$$

where β_0 is a reference propagation constant ($\beta_0 = k_0\, n$). Substituting into the Helmholtz equation and neglecting second-order derivatives of the slowly varying envelope with respect to z yields the paraxial wave equation

$$\frac{\partial \psi}{\partial z} = \frac{i}{2\beta_0} \nabla_T^2 \psi + i \frac{k_0^2 n^2(x,y,z) - \beta_0^2}{2\beta_0} \psi$$

where ∇_T^2 is the Laplacian operator in the transverse (x,y) plane. This equation resembles a Schrödinger-type evolution equation, with z playing the role of time, the transverse Laplacian representing diffraction, and the refractive index variation acting as a potential term.

The numerical implementation of BPM relies on discretizing the propagation axis into small steps Δz. Given the field distribution $\psi(x,y,z)$ at a plane z, one computes the distribution at $z + \Delta z$ by applying an approximate propagator. Various integration schemes exist.

The split-step Fourier method is one of the most common. It separates the diffraction operator (transverse Laplacian) and the refractive index operator, applying them sequentially within each step. The diffraction term is most efficiently evaluated in the Fourier domain, where ∇_T^2 corresponds to a multiplication by $-k_x^2 - k_y^2$. Thus, the algorithm alternates between spatial and Fourier domains. Free-space diffraction is treated by phase multiplication in Fourier space, while index variations are handled in the spatial domain by multiplying the field by a phase factor. This procedure provides both efficiency and accuracy for sufficiently small step sizes.

An alternative scheme is the finite-difference BPM, where the transverse Laplacian is discretized on a spatial grid and the resulting system of ordinary differential equations in z is integrated using implicit or explicit schemes. Finite-difference formulations allow direct incorporation of boundary conditions and complex refractive index profiles but can be computationally heavier for large domains compared to split-step methods.

The validity of BPM depends on the paraxial approximation. It assumes that the field envelope varies slowly with respect to z and that propagation angles relative to the z-axis remain small. As such, BPM is well suited for weakly guiding structures, single-mode and multimode waveguides, directional couplers, and photonic circuits where most of the energy flows forward along the main axis. However, it is less accurate for problems involving sharp discontinuities, strong reflections, high-index contrast, or wide-angle scattering. Extensions such as wide-angle BPM have been developed, in which higher-order terms in the expansion are retained to increase accuracy in strongly guiding configurations.

BPM can also be adapted to model nonlinear optical propagation. In this case, the refractive index becomes intensity-dependent, $n = n_0 + n^2|E|^2$, and the nonlinear contribution enters as an additional phase modulation term in the propagation equation. This allows simulations of self-focusing, soliton dynamics, and nonlinear switching devices within integrated optics. Moreover, BPM is readily extended to include anisotropic or absorbing media by allowing complex or tensor-valued refractive indices.

In practical implementation, absorbing boundary conditions or perfectly matched layers (PMLs) are introduced at the edges of the computational window to avoid spurious reflections. The size of the transverse computational grid and the choice of step size Δz must be carefully balanced since fine resolution ensures accuracy but increases memory and computational load, while large step sizes may compromise stability and convergence. Adaptive step-size control and beam windowing techniques are often employed to optimize simulations.

Appendix C

Scattering Matrix and Transfer Matrix Methods

The analysis of optical and electromagnetic structures often relies on formalisms that express the relationship between incident and transmitted fields across layered or segmented regions. Two of the most widely adopted approaches are the Scattering Matrix Method and the Transfer Matrix Method (TMM). Both are rooted in the linearity of Maxwell's equations in the frequency domain and the modal decomposition of fields into forward- and backward-propagating components, yet they emphasize different ways of structuring the input–output relations of a device.

The scattering matrix method directly relates incoming and outgoing wave amplitudes. At each port of a device, it is possible to define incoming fields a_j and outgoing fields b_j, which represent the modal amplitudes incident upon and emerging from the device ports. The incoming and outgoing fields are related as

$$b = S\,a$$

where $a = (a_1, a_2, \ldots, a_N)^T$, $b = (b_1, b_2, \ldots, b_N)^T$, and S is the scattering matrix of dimension $N \times N$, with N denoting the number of ports or modes. The matrix element S_{ij} represents the transmission from an incoming port j to an outgoing port i. In a two-port system, this reduces to

$$\begin{pmatrix} b_1 \\ b_2 \end{pmatrix} = \begin{pmatrix} S_{11} & S_{12} \\ S_{21} & S_{22} \end{pmatrix} \begin{pmatrix} a_1 \\ a_2 \end{pmatrix}$$

Parameters along the diagonal of the S-matrix are referred to as reflection coefficients because they only refer to what happens at a single port, while off-diagonal S-parameters are referred to as transmission coefficients, because they refer to what happens at one port when it is excited by a signal incident at another port. S-parameters are complex numbers, having a real and imaginary part (or magnitude and phase), because both the magnitude and phase of the incident signal are

changed by the network. The power in the scattered wave is represented by the square of the magnitude of an S-parameter. S-parameters are defined for a given frequency and vary as a function of frequency.
The scattering matrix of a complex system can be constructed by combining the scattering matrices of its subsystems. The combination is carried out through algebraic operations that eliminate the internal connections between subsystems, often expressed via the so-called Redheffer star product. This procedure preserves the correct mapping between external ports while internal degrees of freedom are removed. One of the most important properties of the scattering matrix is its boundedness. Indeed, for passive and lossless systems, *S* is unitary, ensuring energy conservation, while reciprocity conditions enforce symmetry. These properties make Scattering Matrix Method not only numerically stable but also directly comparable with experimental characterization, as scattering parameters (*S*-parameters) are the standard outputs of microwave network analysis and optical measurement setups.
The Scattering Matrix Method framework naturally extends to multimode waveguides and networks of interconnected devices. In such cases, each port may support multiple guided or radiation modes, and the scattering matrix generalizes to relate the full set of modal amplitudes. The unitarity property remains central, ensuring that the total power carried by all modes is conserved. This feature makes this theory particularly attractive for modeling large-scale integrated photonic circuits or microwave networks, where numerous interconnections and multiple reflections are present.

The transfer matrix method originates from the description of electromagnetic waves in stratified media. Within each homogeneous region, the Helmholtz equation admits solutions that can be expressed as the superposition of waves propagating along the longitudinal direction. In a one-dimensional geometry, the field in region j can be represented as

$$E_j(z) = A_j e^{ik_j z} + B_j e^{-ik_j z}$$

where A_j and B_j denote the forward- and backward-propagating amplitudes and k_j is the propagation constant in the medium. At the interface between two adjacent regions, boundary conditions impose the continuity of tangential components of the fields. These boundary conditions lead to a linear relation between the amplitude vectors of region j and region $j+1$, which can be compactly expressed through a transfer matrix. For example, for a given layer of thickness d_j, the propagation of fields across the layer is described by a propagation matrix, while the discontinuity in refractive index at each interface is described by an interface matrix. The transfer matrix of the entire layer is obtained as the product of interface and propagation contributions. In compact notation

$$\begin{pmatrix} A_{j+1} \\ B_{j+1} \end{pmatrix} = T_j \begin{pmatrix} A_j \\ B_j \end{pmatrix}$$

where Tj is a 2×2 matrix containing exponential terms $e^{\pm ik_j d_j}$ as well as the Fresnel coefficients at the interfaces. The global transfer matrix of a multilayer structure is then obtained by multiplying the transfer matrices of each individual layer,

$$\begin{pmatrix} A_N \\ B_N \end{pmatrix} = \left(\prod_{j=1}^{N-1} T_j \right) \begin{pmatrix} A_1 \\ B_1 \end{pmatrix}$$

This formulation represents closed-form solutions for simple stratified stacks and efficient algorithms for multilayer systems. However, a notable drawback of the TMM is its numerical instability when applied to long or highly resonant structures since the matrices involve exponential terms and successive multiplication. This can lead to extremely large or small entries, causing loss of precision due to finite machine accuracy.

Comparing the two approaches becomes evident that they are alternative representations of the same underlying linear relations. The transfer matrix method directly propagates amplitudes across layers, making it straightforward and analytically transparent, particularly in stratified geometries and thin-film optics. However, successive multiplication of transfer matrices introduces exponential terms that can lead to numerical instabilities, especially in long structures or near resonances, where very large or very small numbers are encountered. The scattering matrix formulation, by contrast, expresses input–output relations in terms of reflection and transmission coefficients, quantities that remain bounded by physical principles. As a result, Scattering matrix method is numerically more stable and better suited for the analysis of extended or highly resonant systems, as well as for direct comparison with experimental data. Ultimately, both methods are grounded in the same physics, and the choice between them depends on the geometry under study and the numerical stability requirements.

Appendix D

Coupling mode Theory

Coupled Mode Theory (CMT) provides a powerful analytical framework for describing the interaction of modes in optical and electromagnetic systems. It is particularly useful in integrated optics, waveguide couplers, resonators, and photonic crystal devices, where energy can transfer between different spatial or temporal modes due to perturbations or proximity of guiding structures. The essence of CMT lies in reducing the full set of Maxwell's equations, which are often intractable in complex geometries, into a set of ordinary differential equations that govern the slowly varying amplitudes of interacting modes. These equations capture how power oscillates between coupled channels under the influence of perturbations in refractive index, material absorption, or boundary conditions.

The starting point of the theory is the frequency-domain Maxwell's equations, which can be written as an eigenvalue problem for the unperturbed system. In the absence of coupling, the electromagnetic field distributions $E_m(r)$ and $H_m(r)$ form a complete set of orthogonal modes, each associated with a propagation constant β_m in the case of waveguides, or a resonant frequency ω_m in the case of cavities. These modes satisfy orthogonality relations derived from Lorentz reciprocity, which provide the mathematical foundation for projecting the full fields onto a modal basis. In a perturbed system, the total field is expressed as a superposition of these unperturbed modes with slowly varying amplitudes,

$$E(r,z) = \sum_m a_m(z) E_m(r) e^{i\beta_m z}$$

where $a_m(z)$ are the modal amplitudes that evolve with the propagation coordinate z. The assumption of slow variation allows neglecting second-order derivatives of the amplitudes with respect to z, an approximation that reduces the governing equations to a first-order system.

By substituting the modal expansion into Maxwell's equations for the perturbed structure and applying the orthogonality relations, one derives the coupled mode equations. For two interacting modes, labeled 1 and 2, the equations take the canonical form

$$\frac{da_1}{dz} = -i\, k_{12} e^{i(\beta_1-\beta_2)z} a_2$$
$$\frac{da_2}{dz} = -i\, k_{21} e^{i(\beta_2-\beta_1)z} a_1$$

where κ_{mn} are the coupling coefficients determined by the overlap integrals of the modal fields with the perturbation. Explicitly, the coupling coefficient between modes m and n is proportional to

$$\kappa_{mn} \propto \iint \Delta\epsilon(r) E_m^*(r) \cdot E_n(r)\, dA$$

with $\Delta\epsilon(r)$ representing the dielectric perturbation that mediates the coupling. These integrals quantify the strength of interaction based on spatial overlap of field distributions and the refractive index variation.

In the special case of phase matching, where $\beta_1 \approx \beta_2$, efficient power transfer occurs between the modes. The coupled mode equations then reduce to sinusoidal solutions, where power oscillates periodically from one mode to the other with a characteristic coupling length $L_c = \frac{\pi}{2|k|}$. This phenomenon underlies the operation of directional couplers, where two parallel waveguides placed in close proximity exchange power back and forth along their length. Conversely, when the propagation constants differ significantly, the exponential phase factors prevent efficient coupling, and the interaction remains weak.

CMT also extends naturally to resonant systems. In a cavity or ring resonator, the temporal coupled mode theory formulation describes the time evolution of modal amplitudes. Here, the fields are expanded as

$$E(r,t) = \sum_m a_m(t) E_m(r) e^{i\omega_m t}$$

where the modal amplitudes $a_m(t)$ satisfy ordinary differential equations of the form

$$\frac{da_m}{dt} = (i\omega_m - \gamma_m) a_m + \sum_m k_{mn} a_n + s_{in}$$

with γ_m representing loss or decay rates, κ_{mn} the coupling between modes, and s_{in} the external source term representing excitation from input channels. This formalism is central to the modelling of resonator–waveguide coupling, filters, and sensors, where resonance linewidths, quality factors, and transmission spectra are directly extracted from the coupled mode equations.

A key advantage of CMT lies in its ability to capture essential device physics with relatively simple equations, bypassing the need for full numerical solutions of Maxwell's equations in each geometry. The coupling coefficients contain the geometrical and material details, while the equations themselves describe the

evolution of modal amplitudes. This abstraction not only enables analytical insight but also provides a computationally efficient framework for simulating complex photonic circuits, where multiple couplings and interactions occur simultaneously. Nevertheless, the accuracy of CMT relies on certain assumptions. The perturbation must be weak enough that the unperturbed modal basis remains valid, and the envelopes of the modal amplitudes must vary slowly compared to the oscillatory carrier terms. Furthermore, radiation modes and higher-order corrections are often neglected, which may limit accuracy in structures with strong discontinuities or large perturbations. Extensions of CMT have been developed to relax these assumptions, including formulations for strong coupling, multimode systems, and nonlinear interactions, where the coupling coefficients depend on the field amplitudes themselves.

Appendix E

Synthetic Aperture Radar System

Synthetic Aperture Radar (SAR) is a coherent imaging system that provides high-resolution two-dimensional reconstructions of a scene by exploiting the relative motion of the radar platform with respect to the illuminated area. Unlike radar, in which azimuth resolution is constrained by the physical size of the antenna, SAR synthesizes a much larger effective aperture by coherently integrating the echoes collected along the flight trajectory. This principle makes it possible to achieve fine resolution independent of range, enabling detailed imaging for Earth observation, planetary science, surveillance, and geophysical monitoring under virtually all weather and illumination conditions.

The operation of SAR begins with the transmission of a modulated radar pulse, most commonly a linearly frequency-modulated chirp, described as

$$s(t) = e^{i\,(\omega_0 t + 1/2\alpha t^2)}$$

where ω_0 is the carrier frequency and α is the chirp rate. After propagating to the target and back, the received signal for a point scatterer at distance R is

$$r(t) = \sigma s(t - 2R/c)$$

with σ the radar cross-section and c the speed of light. Range resolution is obtained through pulse compression, performed by matched filtering, which yields

$$\Delta R = \frac{c}{2B}$$

where B is the bandwidth of the transmitted signal. Thus, fine range resolution is directly tied to large bandwidths.

In the azimuth direction, SAR capitalizes on the Doppler modulation introduced by platform motion. As the radar moves along its trajectory, a stationary target is observed from multiple aspect angles, producing a varying Doppler frequency given approximately by

$$f_D(t) = \frac{2v}{\lambda} sin\theta(t)$$

where v is the platform velocity, λ the radar wavelength, and $\theta(t)$ the instantaneous look angle to the target. The collection of Doppler-shifted echoes forms the Doppler history of the scatterer, and coherent integration of these signals synthesizes a large aperture of length comparable to the platform displacement during the observation interval. The resulting azimuth resolution is

$$\Delta x \approx \frac{L}{2}$$

where L is the physical antenna length. This resolution is independent of range, in contrast with radar where it degrades linearly with distance.

Beyond the signal processing principles, a SAR system consists of several fundamental building blocks. At the core is the antenna subsystem, which transmits and receives the radar signals. Although typically of modest physical aperture, the antenna must be designed to provide adequate beamwidth and sidelobe control in both range and azimuth directions. Modern SAR platforms may employ phased array antennas, enabling electronic beam steering and multiple operating modes such as stripmap, spotlight, or scanSAR.

The transmitter subsystem generates the modulated radar waveform. This requires a stable frequency source, waveform generator, and a high-power amplifier capable of transmitting sufficient energy to illuminate the scene while maintaining spectral purity. In many systems, chirped pulses are generated digitally and then upconverted to the desired carrier frequency.

The receiver subsystem performs low-noise amplification, downconversion, and digitization of the returned echoes. Coherence between transmitted and received signals is critical, and thus the transmitter and receiver share a common local oscillator reference to preserve phase stability.

Positioning and navigation systems, such as GPS combined with inertial measurement units, are employed to provide the necessary accuracy. Residual errors in trajectory reconstruction introduce phase distortions that must be corrected in post-processing through motion compensation algorithms. The data acquisition and storage subsystem is crucial, as SAR imaging involves sampling wideband signals at high rates over long integration times, generating large volumes of raw data. These data streams are stored on-board or downlinked to ground stations, where they are processed into images.

Image formation is typically carried out by algorithms such as range-Doppler processing, chirp scaling, or back-projection. In each case, the processing entails matched filtering in both range and azimuth to reconstruct the reflectivity function $\sigma(x,y)$ of the scene.

Furthermore, SAR systems often integrate processing subsystems that implement compression, focusing, and multi-look averaging in real time, particularly in airborne and tactical applications where rapid image availability is required.

Appendix F

Finite Difference Time Domain (FDTD) Method

The Finite-Difference Time-Domain (FDTD) method is a numerical technique for solving Maxwell's equations in the time domain, and it has become one of the most widely employed methods for modelling electromagnetic wave propagation, scattering, and interaction with complex materials and structures. It directly discretizes Maxwell's equations on a grid in both space and time, enabling a full-wave description of electromagnetic fields without resorting to frequency-domain approximations. This approach is particularly powerful in photonics, microwave engineering, antenna analysis, and nanophotonics, where arbitrary geometries and dispersive materials must be modelled with high accuracy.

The method begins with Maxwell's equations in differential form for non-magnetic, source-free media, which in SI units can be expressed as

$$\nabla \times E = -\mu \frac{\partial H}{\partial t},$$
$$\nabla \times H = \epsilon \frac{\partial E}{\partial t}$$

where E and H denote the electric and magnetic fields, and ϵ and μ represent the permittivity and permeability of the medium. In FDTD, the spatial and temporal derivatives appearing in these equations are replaced with finite differences defined on a staggered computational grid, known as the Yee grid. This grid arrangement, introduced by Kane Yee in 1966, interleaves the electric and magnetic field components in space and staggers their updates in time by half a time step, ensuring that Faraday's and Ampère's laws are enforced in a naturally consistent manner.

For illustration, consider the one-dimensional case of a wave propagating along the z-axis with electric field polarized in the x-direction and magnetic field in the y-direction. Maxwell's equations reduce to

$$\frac{\partial E_x}{\partial z} = -\mu \frac{\partial H_y}{\partial t}$$

$$\frac{\partial H_y}{\partial z} = -\epsilon \frac{\partial E_x}{\partial t}$$

Discretizing the spatial coordinate into steps of Δz and the temporal coordinate into steps of Δt, the FDTD scheme updates the field values iteratively according to difference equations of the form

$$H_y^{n+1/2}(i+1/2) = H_y^{n-1/2}(i+1/2) - \frac{\Delta t}{\mu\, \Delta z}[E_x^n(i+1) - E_x^n(i)]$$
$$E_x^{n+1}(i) = E_x^n(i) - \frac{\Delta t}{\epsilon\, \Delta z}\left[H_y^{n+1/2}(i+1/2) - H_y^{n+1/2}(i-1/2)\right],$$

where n denotes the discrete time step and i the discrete spatial index. The staggering of indices in both space and time is the essence of the Yee scheme, which guarantees second-order accuracy in both domains while preserving the divergence conditions of Maxwell's equations.

The three-dimensional extension follows the same principle, with each component of the electric and magnetic fields defined on a lattice such that the operations involve neighbouring components in a straightforward finite-difference stencil. By iteratively updating all six field components in time, the electromagnetic field evolution is obtained over the entire computational domain. This explicit marching scheme makes FDTD conceptually simple yet highly general, able to capture broadband responses with a single simulation since the full temporal field is available and can later be transformed into the frequency domain via Fourier analysis.

A key condition for stability in FDTD is the Courant–Friedrichs–Lewy (CFL) criterion, which imposes a limit on the maximum allowable time step. In three dimensions, the condition reads

$$\Delta t \leq \frac{1}{c} \frac{1}{\sqrt{\left(\frac{1}{\Delta x^2} + \frac{1}{\Delta y^2} + \frac{1}{\Delta z^2}\right)}}$$

where c is the speed of light in the medium and Δx, Δy, Δz are the grid spacings. This criterion ensures that the numerical wavefront does not propagate faster than the physical speed of light, thereby preventing instability.

Practical FDTD implementations require careful handling of boundaries. Since the computational domain is finite while electromagnetic problems are often open, artificial boundary conditions must be introduced to mimic free-space propagation. The most common approach is the Perfectly Matched Layer (PML), an artificial absorbing medium that minimizes reflections at the boundaries for waves of arbitrary incidence and frequency. The PML is indispensable in photonics and scattering problems where spurious reflections would otherwise contaminate the results. In addition to absorbing boundaries such as the Perfectly Matched Layer, another essential class of boundary conditions in FDTD simulations arises when modeling conductors. The most widely used is the Perfect Electric Conductor (PEC) boundary condition, which idealizes a surface as having infinite conductivity. PEC

boundaries are widely used to model metallic waveguides, cavity resonators, and antennas, where the finite conductivity of real metals can often be approximated as infinite when the skin depth is negligible compared to geometric dimensions.

Material modeling in FDTD extends beyond simple linear dielectrics. Dispersive media, such as metals at optical frequencies, can be incorporated by introducing auxiliary differential equations or convolutional updates that reproduce the frequency-dependent permittivity, for example via Drude or Lorentz models. Nonlinearities can also be included by updating the permittivity as a function of the instantaneous field intensity, enabling simulations of Kerr effects or harmonic generation. This flexibility highlights the method's versatility in addressing a wide range of physical phenomena.

Despite its strengths, FDTD faces challenges in terms of computational efficiency. The explicit nature of the algorithm implies that fine spatial discretization, necessary to resolve subwavelength structures, leads to very small time steps due to the CFL condition, resulting in long simulation times. Memory requirements also scale with the number of grid points, which can become prohibitive for large three-dimensional domains. Parallel computing and domain decomposition methods have been developed to mitigate these limitations, making FDTD feasible for increasingly complex systems.

In practice, an FDTD simulation involves defining the computational domain and grid, specifying the material properties of each cell, placing sources such as plane waves, dipoles, or Gaussian pulses, and recording field quantities at monitors or detectors. The time-domain output can be transformed to the frequency domain to obtain spectra, scattering parameters, or modal properties. Because FDTD inherently captures broadband responses in a single run, it is especially efficient when wide spectral information is required.